VILNIUS UNIVERSITY

CENTER FOR PHYSICAL SCIENCES AND TECHNOLOGY

Dainius Prakapavičius

OXYGEN IN STELLAR ATMOSPHERES: SPECTRAL LINE FORMATION AND ABUNDANCES

Doctoral Dissertation

Physical sciences, Physics (02 P)

Vilnius, 2017

Doctoral dissertation was completed during doctorate studies at Vilnius University, Institute of Theoretical Physics and Astronomy in 2010–2014 and is defended in extern.

Scientific supervisor – dr. Arūnas Kučinskas (Vilnius University, Physical sciences, Physics – 02 P). From 2010 10 01 until 2014 09 30.

Scientific adviser – dr. Arūnas Kučinskas (Vilnius University, Physical sciences, Physics – 02 P). From 2014 10 01 until 2017 04 18.

VILNIAUS UNIVERSITETAS

FIZINIŲ IR TECHNOLOGIJOS MOKSLŲ CENTRAS

Dainius Prakapavičius

DEGUONIS ŽVAIGŽDŽIŲ ATMOSFEROSE: SPEKTRO LINIJŲ FORMAVIMASIS IR GAUSA

Daktaro disertacija

Fiziniai mokslai, fizika (02 P)

Vilnius, 2017

Disertacija rengta 2010–2014 metais Vilniaus universitete, Teorinės fizikos ir astronomijos institute studijuojant doktorantūroje ir ginama eksternu.

Mokslinis vadovas – dr. Arūnas Kučinskas (Vilniaus universitetas, fiziniai mokslai, fizika – 02 P). Nuo 2010 10 01 iki 2014 09 30.

Mokslinis konsultantas – dr. Arūnas Kučinskas (Vilniaus universitetas, fiziniai mokslai, fizika – 02 P). Nuo 2014 10 01 iki 2017 04 18.

Abstract

The realism of spectroscopic abundance determination depends directly on the realism of physical assumptions used in the model atmospheres and spectral synthesis tools. The vast majority of stellar abundances in late-type stars are determined using classical 1D (plane-parallel or spherically symmetric) hydrostatic model atmospheres. It is well known however that low-mass stars exhibit granulation patterns that arise due to convective motions in their atmospheres. Although these dynamical fluid flows directly influence conditions under which stellar radiation forms, they are not properly accounted for in the 1D hydrostatic model atmospheres. This can be done in a much more realistic way by using more advanced 3D hydrodynamical model atmospheres. In a similar way, while the assumption of non-local thermodynamic equilibrium (NLTE) is becoming more and more widely used in 1D abundance analysis, it is rarely applied with the 3D hydrodynamical model atmospheres.

In this Thesis we developed a methodology that could be used to model non-local radiative transfer and, subsequently, for computing NLTE oxygen spectral line profiles using 3D hydrodynamical model atmospheres. This was done by generalizing and expanding spectral synthesis code `NLTE3D` and constructing a realistic model atom of oxygen. This methodology was applied for the analysis of solar intensity spectrum of O I IR triplet located near 777 nm. We also investigated the role of convection in the formation of molecular lines both theoretically (using weak fictitious lines) and by analysing high-quality spectra of the metal-poor halo giant HD 122563. The impact of convection was quantified with the aid of 3D–1D abundance corrections, i.e., the difference in the abundance of particular chemical element determined using the same spectral line of a given equivalent width, W, with the 3D hydrodynamical and 1D hydrostatic model atmospheres.

The main results of this Thesis are: (1) the `NLTE3D` package has undergone significant upgrade and generalization allowing to use oxygen model atom for the spectral synthesis with the `CO`^{5}`BOLD` model atmospheres. Implementation of accelerated Λ-iteration (ALI) scheme allows for faster solution of the non-local radiative transfer problem; (2) a new model atom of oxygen has been constructed and implemented in `NLTE3D` package. The new model atom was used to determine 3D NLTE solar oxygen abundance; (3) solar oxygen abundance was determined using the updated `NLTE3D` package, realistic solar `CO`^{5}`BOLD` model

atmosphere and two sets of solar intensity spectra taken at different limb angles. The obtained value is A(O) = 8.76 ± 0.02. The solar oxygen abundance determined using 3D hydrodynamical `CO5BOLD` model atmosphere is higher than that determined using `STAGGER` model atmospheres (A(O) < 8.70); (4) 3D–1D abundance corrections of weak molecular (CH, CO, C_2, NH, CN, and OH) lines were determined using model atmospheres of stars located in the lower part of the red giant branch (RGB) at four different metallicities, [Fe/H] $= 0, -1, -2, -3$. It was found that the 3D–1D abundance corrections become larger and increasingly more negative at lowest metallicities and line excitation potentials. The largest (and most negative) 3D–1D abundance correction was determined for the resonance lines of CO at [Fe/H] $= -3$ and reach -1.8 dex. (5) it was found that the cool layers of the 3D hydrodynamical model atmosphere play an important role in the formation of molecular lines. Since the low temperatures that are encountered in the 3D hydrodynamical model atmospheres are not present in the classical 1D models, we found that realistic modelling of molecular line formation could not be achieved using classical model atmospheres; (6) mean oxygen abundance in the atmosphere of the metal-poor halo star HD 122563 determined using OH lines located in the UV part of the spectrum (310–330 nm) and the 1D hydrostatic `ATLAS9` model atmospheres is A(O) $= 6.41 \pm 0.16$. The mean 3D LTE oxygen abundance determined using classical `LHD` and 3D hydrodynamical `CO5BOLD` model atmospheres is A(O) $= 6.23 \pm 0.13$. 1D LTE oxygen abundances showed significant trends with line excitation potential and strength. However, oxygen abundances corrected for the 3D-effects using 3D–1D LTE abundance corrections did not exhibit such trends; (7) the 3D–1D oxygen abundance corrections in the atmosphere of HD 122563 were different for different OH UV lines and their size was found to be correlated with the line excitation potential and/or line strength and covered a range between 0.45 dex at 0 eV to 0.0 dex at 1.5 eV; (8) oxygen-to-iron ratio in the atmosphere of HD 122563 is [O/Fe] $= 0.07 \pm 0.13$ dex and falls at the lower boundary of oxygen abundance spread observed at this metallicity and does not support the high over-abundance ([O/Fe] ≈ 1.0) of oxygen in the metal-poor stars.

Acknowledgments

Firstly, I am very thankful for my supervisor Arūnas Kučinskas for his patience, guidance and help during my study years.

I would also like to express my gratitude for Matthias Steffen for the work we did together.

I appreciate useful communication with H.-G. Ludwig, P. Bonifacio, B. Freytag, E. Caffau, L. Mashonkina and S. Korotin that helped to deepen and widen my knowledge on many occasions.

I also acknowledge numerous discussions with V. Dobrovolskas, J. Klevas, A. Černiauskas, V. Vansevičius, G. Tautvaišienė, J. Sperauskas, D. Narbutis, K. Zubovas, G. Valiauga, E. Stonkutė, K. Milašius, R. Ženovienė, M. Macijauskas, A. Drazdauskas and many others.

I would like to acknowledge Vilnius University, Germany Academic Exchange Service, Lithuanian Research Council and Potsdam Astrophysics Institute for financial support allowing me to visit conferences, summer schools and Leibniz Institute for Astrophysics in Potsdam.

I also thank Adomas, Agneška, Aistė, Algirdas, Domantas, Jonas, Ieva, Kamilis, Laimis, Marius, Silvija, Simonas and Vytis for the special friendship.

Above all, I am indebted for my parents Arvydas and Kornelija for the continuous support.

Abbreviations

$\langle 3D \rangle$ – averaged 3D;

ALI – accelerated Λ-iteration; an iterative method that is applied in cases where radiative source function depends on the intensity of radiation field;

$\log g$ – logarithm of stellar surface gravity, cgs;

LTE – local thermodynamic equilibrium;

MLT – mixing length theory;

NLTE – non-local thermodynamic equilibrium;

O I IR triplet – oxygen IR triplet, individual spectral lines located at $\lambda_1 = 777.2, \lambda_2 = 777.4, \lambda_3 = 777.5$ nm;

RGB – red giant branch;

$T_{\rm eff}$ – stellar effective temperature, K;

W – spectral line equivalent width;

$\xi_{\rm mac}$ – macroturbulence velocity, km/s;

$\xi_{\rm mic}$ – microturbulence velocity, km/s;

$\tau_{\rm Ross}$ – Rosseland optical depth in stellar atmosphere;

χ – spectral line excitation potential, eV.

Contents

Introduction **11**
Motivation . . . 11
Novelty . . . 15
Aims of the study . . . 16
Main tasks . . . 16
Results and statements to defend . . . 16
Personal contribution . . . 16
Publications on the Thesis topic in the refereed journals . . . 18
Other publications in the refereed journals . . . 18
Presentations at the conferences . . . 18
Thesis outline . . . 19

1 Model atmospheres and spectral line synthesis **21**
1.1 Model atmospheres . . . 21
1.1.1 3D hydrodynamical `CO`^{5}`BOLD` model atmospheres . . . 24
1.1.2 1D hydrostatic model atmospheres . . . 28
1.2 Spectral line synthesis . . . 28
1.2.1 3D NLTE spectral synthesis . . . 28
1.2.2 Spectral line synthesis with the `Linfor3D` package . . . 32

2 `NLTE3D` code: physics, implementation, and tests **35**
2.1 Introduction . . . 35
2.2 Formulation of the NLTE problem . . . 36
2.3 Accelerated Λ-iteration scheme . . . 38
2.4 Solution of statistical equilibrium equations . . . 42
2.5 An outline of the `NLTE3D` code . . . 43
2.6 Performance of ALI scheme . . . 44

3 Spectral lines of atomic oxygen in stellar atmospheres: O I IR triplet lines and solar oxygen abundance **47**
3.1 Introduction . . . 47
3.2 Observational data . . . 49
3.3 Model atmospheres . . . 51
3.4 3D/1D NLTE spectral synthesis computations . . . 53
3.4.1 Model atom of oxygen . . . 53
3.4.2 Estimation of NLTE effects . . . 56
3.4.3 Spectral synthesis calculations . . . 56
3.5 Line profile fitting and results . . . 57
3.5.1 Fitting procedure . . . 57
3.5.2 Fitting results for the WCLC and Pereira spectra . . . 59
3.5.3 Fitting of disk-center intensity and flux line profiles . . . 63

3.6 Equivalent width fitting and results 64
  3.6.1 Equivalent width measurements 64
  3.6.2 *W* fitting of disk-center and full-disk spectra 66
  3.6.3 *W* fitting of the μ-dependent WCLC and Pereira spectra 67
3.7 Discussion 71
  3.7.1 Comparison with previous work 71
  3.7.2 Interpretation of the obtained 1D NLTE results 73
  3.7.3 Treatment of inelastic collisions with neutral hydrogen 76

4 Influence of convection on the formation of molecular spectral lines in the atmospheres of RGB stars 79
4.1 Introduction 79
4.2 Model atmospheres 80
4.3 Spectral line synthesis 80
4.4 Influence of convection on the formation of molecular lines 83

5 Oxygen abundance in the metal-poor giant HD 122563 determined using OH UV lines 91
5.1 Introduction 91
5.2 Target star and observations 93
5.3 Model atmospheres 95
5.4 Oxygen abundance in HD 122563 from OH UV lines 98
  5.4.1 Determination of 1D LTE oxygen abundances 98
  5.4.2 Determination of 3D LTE oxygen abundances 102
  5.4.3 Error budget 107
5.5 Results and discussion 109
  5.5.1 1D LTE and 3D LTE oxygen abundance in HD 122563 109
  5.5.2 OH UV line formation 112
  5.5.3 Early Galactic evolution of oxygen 117

Summary and conclusions 119

References 121

Appendix A. The 3D–1D abundance corrections for the spectral lines of molecules in the atmospheres of red giant branch (RGB) stars located at the lower part of RGB 128

Appendix B. OH line list and oxygen abundances determined from individual lines in HD 122563 132

Introduction

Motivation

Stars are composed of various chemical species and their abundance varies from star to star. In stellar spectra, these chemical elements leave their 'fingerprints' in the form of absorption lines. Interpretation of stellar spectra is therefore one of the means to study chemical composition of stellar photospheres. Knowledge about abundances of chemical elements in stars, combined with the kinematical information about these objects, is of key importance for understanding formation and chemical-dynamical evolution of various stellar populations, such as star clusters, different components of the Galaxy (disks, halo), and galaxies at large.

In this sense, oxygen is very useful since it is the third most abundant chemical element (after hydrogen and helium). The bulk of oxygen is produced via helium-burning in evolved stars of high mass ($M/M_{\odot} \gtrsim 10$). Oxygen abundances determined in stellar atmospheres could be used for analysis of time-scales of evolution of stellar populations via oxygen-to-iron abundance ratio, [O/Fe][1]. Upon the formation of a stellar system, type II supernovae (SNe) contribute oxygen-rich ejecta to the local interstellar medium (ISM) which produces high and positive [O/Fe]. Only about 1 Gyr later type Ia SNe start providing iron to the ISM and this lowers [O/Fe] ratio what is reflected in the chemical composition of stars. By comparing [O/Fe] vs. [Fe/H] plots with the predictions of theoretical models, one can gain information about the type Ia-to-II ratio of SNe in the stellar system and the nature of the system itself. Given the observed oxygen abundance gradient within any disk galaxy and a galactic chemical evolution model, it is possible to reconstruct the nature and formation of galactic disks (Chiappini et al. 1997; Chiappini et al. 2001; Stasińska et al. 2012).

Since the determined oxygen abundances could be applied in a variety of ways, one should be careful in choosing the most reliable abundance indicators. In this Thesis we therefore focus on different oxygen abundance indicators in evolved stars. Photospheric oxygen abundance in cool stars can be determined from a number of atomic and molecular spectral lines. Main atomic oxygen

---

[1] $[X/Y] = \log[N(X)/N(Y)]_{\star} - \log[N(X)/N(Y)]_{\odot}$, where X and Y are chemical species

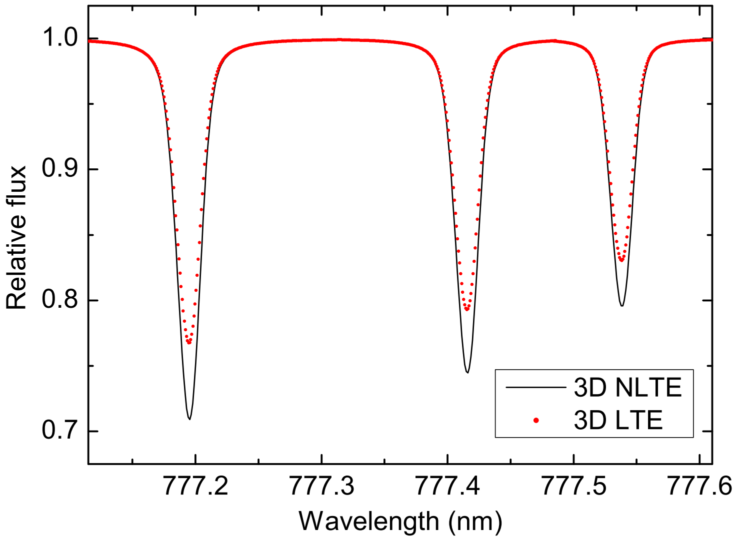

Fig. 1. Theoretical flux profiles of O I IR triplet line computed with Solar 3D hydrodynamical model atmosphere under the assumption of LTE (red dots) and NLTE (continuous black line; from Prakapavičius et al. 2013).

abundance indicators are the forbidden lines (further, [O I]) located at $\lambda = 630$ and 636 nm, and high-excitation IR triplet near $\lambda = 777$ nm. In addition, one may also use molecular OH lines in the UV (310–330 nm) and IR (1500–1650 nm).

The forbidden lines are reliable oxygen abundance indicators since they are thought to form in LTE: ground level of this transition is thermalized via efficient oxygen-proton charge transfer reaction and the upper levels are not involved in radiative transitions that could drive their population numbers away from LTE. However, oscillator strengths of these transitions are very small, and [O I] lines are mainly weak. Their strength diminishes with increasing $T_{\rm eff}$ and they are virtually unobservable in the metal-poor main-sequence stars, but, in giants, they could be measured down to metallicities of [Fe/H] = –3.

Permitted O I IR triplet lines, due to their high excitation potential (χ = 9.146 eV), are not visible in cool giants because temperature in these stars is not sufficiently high. Hence, O I IR triplet lines can only be studied in main-sequence, turn-off dwarfs and sub-giants with $T_{\rm eff} > 5000 - 5500$ K (depending on metallicity). However, unlike forbidden lines, O I IR triplet lines are known to be prone to NLTE effects: non-local radiation field at the wavelengths of the O I IR triplet is lower than expected in LTE and this causes photoexcitation rates to be lower than LTE. While this does not influence the line opacity, the upper level of the triplet gets underpopulated with respect to LTE. This results in diminished line source function and stronger spectral lines in NLTE (e.g., Kiselman 1993, see also Fig. 1).

It is known that, when the abundances are derived using classical one-dimensional (1D) hydrostatic model atmospheres, all described oxygen abundance indicators give quite different A(O) (see, e.g., Grevesse & Sauval 1998; Barbuy et al. 2003; Asplund et al. 2004, and references therein). One may expect that this problem may be alleviated by using three-dimensional (3D) hydrodynamical model atmospheres. Compared to 1D hydrostatic model atmospheres, 3D hydrodynamical models allow to reach qualitatively different level of realism in modelling convection – the process that has significant influence on shaping internal structure of stellar atmospheres as well as their observable properties. Also, they allow for consistent modelling of a variety of hydrodynamic phenomena, such as shock waves, acoustic waves, velocity field etc. Hence, in comparison to 1D models, 3D hydrodynamical model atmospheres are much more realistic.

Asplund et al. (2004) applied Solar model atmosphere computed with the `STAGGER` code (Magic et al. 2013) in order to analyze the observed solar spectrum and to determine A(O) from a variety of photospheric oxygen lines. Surprisingly, a very good match between the abundances determined using different spectral lines was found. The oxygen abundance obtained in this study was $A(O) = 8.66 \pm 0.05$, which was updated slightly upwards by subsequent investigation of Pereira et al. (2009b). Such oxygen abundance is significantly lower than the previous estimate, $A(O) = 8.83$ (Grevesse & Sauval 1998). Although this 'low' A(O) replicates the observed spectral lines much better, it results in worse agreement between precise helioseismic measurements and predictions of theoretical solar interior models. With lowered oxygen content, observational and theoretical quantities, such as location of the base of convective envelope, He abundance, and speed of sound in the convective zone, disagree significantly while the theoretical models computed with the previous solar chemical composition of Grevesse & Sauval (1998) yielded much better agreement.

Similar investigation based on 3D hydrodynamical `CO`^{5}`BOLD` model atmospheres (Freytag et al. 2012) was performed by Caffau et al. (2008). The authors determined oxygen abundance of $A(O) = 8.76 \pm 0.07$ dex, which produces significantly better agreement with the helioseismologically inferred oxygen abundance (Villante et al. 2014). However, although Caffau et al. (2008) used 3D-hydrodynamical model atmospheres, spectrum synthesis of O I IR triplet was performed in 3D LTE and 1D NLTE, while the size of 3D and NLTE effects were estimated separately. Such approaches were criticised in a number of studies (e.g., Kiselman 1993; Pereira et al. 2009b) whose authors argued that the observed center-to-limb variation of OI IR triplet lines can not be reproduced with 1D NLTE and/or 3D LTE approaches. A good match between the observed and theoretical line profiles can only be achieved with full 3D NLTE analysis. Clearly, independent determination of solar oxygen abundance using 3D hydrodynamical `CO`^{5}`BOLD` model atmosphere and NLTE methodology was desirable.

Currently, there are only two software packages that can be used to solve non-equilibrium radiative transfer using 3D model atmospheres – `MULTI3D` and `NLTE3D`. The former package was applied in the studies of Asplund et al. (2004), Allende Prieto et al. (2004), and Pereira et al. (2009b) who performed NLTE analysis of solar O I IR triplet. It was discussed above that it would be very important to perform solar oxygen determination independently from the previous investigations. This task could be done using `NLTE3D` package. However, originally `NLTE3D` package was suited only for spectral synthesis of Li I, and only after performing a number of changes in the `NLTE3D` code, an estimation of 3D NLTE effects on O I IR triplet line formation was possible. In this Thesis we therefore generalized and expanded the `NLTE3D` code with the aim to enable 3D NLTE synthesis of oxygen IR triplet.

Besides the atomic lines, OH UV and IR lines are also used for oxygen abundance determination. OH UV lines are especially useful because they are strong and measurable at very low metallicities, i.e., in situations when atomic oxygen lines become undetectable. Such lines are present in the spectra of all late-type stars and hence are very useful for homogeneous analysis of oxygen abundance in stellar atmospheres across the H-R diagram. However, when analysed with classical 1D model atmospheres, abundances of OH UV lines show trends with the line parameters, such as excitation potential or line strength (Aoki 2015). This hints to problems with either temperature or velocity structure of the model atmosphere. It is also known that formation of molecular lines is very sensitive to the thermal structure of the model atmosphere and abundances determined with the 3D model atmospheres provide significantly different results from those obtained using 1D models (Collet et al. 2007). However, both theoretical and observational investigations of molecular line formation performed using 3D model atmospheres are still scarce. Since oxygen-bearing molecular lines may be very useful in the abundance analysis of metal-poor stars, detailed investigation of molecular line formation in stellar atmospheres with the aid of 3D hydrodynamical model atmospheres would be both timely and important.

Novelty

The work presented in this Thesis is novel in a several aspects:

1. `NLTE3D` package was expanded and adopted for the oxygen spectral line synthesis using 3D hydrodynamical `CO`^{5}`BOLD` model atmospheres. The expansion of `NLTE3D` package includes the implementation of the accelerated Λ-iteration (ALI) scheme, ability to treat various collisional processes, ability to perform calculations using various model atoms (and ions), computation of background continuum opacity, and treat the departure from the ionization equilibrium.
2. Photospheric solar oxygen abundance was determined from O I IR triplet lines using 3D NLTE spectral synthesis using 3D hydrodynamical `CO`^{5}`BOLD` model atmospheres. Our analysis has revealed that profiles and strengths of individual O I IR triplet lines observed at different limb angles in the Sun can only be reproduced using full 3D NLTE approach (reduced $\chi^2 \approx 1$), whereas 1D NLTE/LTE methodology yields unsatisfactory results (reduced χ^2 values range between 5–15).
3. Detailed analysis of interplay between convection and molecular (CO, OH, C_2, CH, NH, CN) line formation in the atmospheres of red giant branch stars was carried out. It was found that the number densities of molecules are very sensitive to the horizontal fluctuations of thermodynamic and hydrodynamical parameters. Because of this, spectral lines computed with the 3D hydrodynamical model atmospheres are stronger than their 1D hydrostatic counterparts. The abundances determined using 3D hydrodynamical model atmospheres can be up to 1.8 dex lower than those determined using classical 1D model atmospheres.
4. 3D hydrodynamical model atmosphere was applied to analyse OH UV spectral lines in the spectrum of the metal-poor red giant HD 122563. For this purpose we have used a newly developed methodology where the microturbulence velocity is derived from the 3D hydrodynamical model atmosphere to ensure consistency in differential abundance analysis. The results of our investigation have shown that such method allows to minimize the systematic errors that arise due to the possible shortcomings of the 3D hydrodynamical model atmospheres (for instance, limited spatial resolution). We have also found that, the oxygen abundances determined using OH UV lines and 3D hydrodynamical model atmosphere do not depend on the excitation potential and spectral line strength, while this is not the case in the classical 1D LTE analysis.

Aims of the study

The goal of this work was to study the influence of convection and non-local radiation field on the atomic oxygen spectral line formation in the solar atmosphere; and to investigate the formation of molecular (CO, OH, C_2, CH, NH, CN) spectral lines in the atmospheres of red giant stars.

Main tasks

1. Develop and implement new modules in the `NLTE3D` code dedicated for the 3D NLTE analysis of atomic oxygen lines.
2. Investigate the impact of convection and non-local radiative field on the formation of O I IR triplet lines in the solar spectra, determine atmospheric solar oxygen abundance using the updated `NLTE3D` code.
3. Investigate the impact of convection on molecular (CO, OH, C_2, CH, NH, CN) spectral line formation in the atmospheres of RGB stars.
4. Determine oxygen abundance in the atmosphere of a metal-poor red giant HD 122563 using 3D hydrodynamical model atmosphere and OH lines located in the UV part of the spectrum (310–330 nm).

Results and statements to defend

1. New modules required for the 3D NLTE synthesis of atomic oxygen spectral lines were created and implemented in the `NLTE3D` package: oxygen model atom, ALI scheme, modules required for computation of the influence of collisional processes on the statistical equilibrium and continuum opacities;
2. Solar oxygen abundance determined using high spectral resolution solar spectra observed at different disk positions, 3D hydrodynamical $\mathtt{CO^5BOLD}$ model atmospheres, and NLTE spectrum synthesis is $A(O) = 8.76 \pm 0.02$.
3. Abundance corrections of molecular (CO, OH, C_2, CH, NH, CN) spectral lines in the atmospheres of red giant stars depend on stellar metallicity and excitation potential: the corrections are largest for low excitation (< 0.5 eV) spectral lines observed in the atmospheres of red giant stars of lowest metallicity ($[M/H] = -3.0$).
4. Oxygen abundance in the atmosphere of the metal-poor red giant HD 122563 determined using OH UV lines and applying 3D–1D abundance corrections is $A(O) = 6.23 \pm 0.13$ dex.

Personal contribution

The author contributed to the modification to the `NLTE3D` software package that was aimed to enable calculations using oxygen model atom, inclusion the processes of collisional excitation and ionization, ability to compute continuum opacities and population number densities using IONDIS/IONOPA packages and to treat the departure from the ionization equilibrium. The author performed a number of reliability tests of the updated `NLTE3D` package, compiled a new oxygen the oxygen model atom using data from the literature, performed 3D NLTE and 1D NLTE spectral synthesis of solar O I IR triplet ($\lambda = 777\,\mathrm{nm}$), and determined solar oxygen abundance using the equivalent width fitting technique. These results are described in Chapter 3 and were published in Steffen et al. (2015, co-authors of the paper formulated goals and tasks of the research, performed spectroscopic observations and their reduction, developed methodology used for the oxygen abundance analysis, performed computations of the 3D hydrodynamical and 1D hydrostatic model atmospheres, determined oxygen abundance by using spectral line fitting method, and performed analysis of the results). The author performed 3D LTE and 1D LTE spectral synthesis computations of molecular (CO, OH, C_2, CH, NH, CN) lines, determined 3D–1D abundance corrections of the molecular lines, and contributed towards the analysis of spectral line formation processes of molecular lines in the atmospheres of RGB stars. These results are described in Chapter 4 and were published in Dobrovolskas et al. (2013, co-authors of the paper formulated goals and tasks of the research, performed software development, computation of model atmospheres, various tests, spectral synthesis calculations of atoms and ions, determined 3D–1D abundance corrections for these lines, investigated the influence of convection and scattering on spectral line formation, performed analysis of 3D–1D abundance corrections in different RGB stars, and analysis of results). The author performed spectral synthesis computations using 1D `ATLAS9`, and `LHD`, and 3D hydrodynamical `CO`^{5}`BOLD` model atmospheres of the metal-poor giant HD 122563, did part of 1D LTE and 3D LTE oxygen abundance analysis, and contributed to the analysis of the influence of convection on the formation of OH UV lines. These results are described in Chapter 5 and were published in Prakapavičius et al. (2017, co-authors contributed to the formulation of goals and tasks of the research, calculated the model atmospheres, contributed to the 1D LTE analysis of spectral lines, analysis of the impact of convection on the formation of OH UV spectral lines and analysis of the obtained results).

Publications on the Thesis topic in the ISI WoS journals

1. **Prakapavičius, D.**, Kučinskas, A., Dobrovolskas, V., Klevas, J., Steffen, M., Bonifacio, P., Ludwig, H.-G., and Spite, M., 2017 *Three-dimensional hydrodynamical* `CO5BOLD` *model atmospheres of red giant stars V. Oxygen abundance in the metal-poor giant HD 122563 from OH UV lines* // Astronomy and Astrophysics, 599, A128.
2. Steffen, M., **Prakapavičius, D.**, Caffau, E., Ludwig, H.-G., Bonifacio, P., Cayrel, R., Kučinskas, A., Livingston, W.C., 2015, *The photospheric solar oxygen project. IV. 3D-NLTE investigation of the 777 nm triplet lines* // Astronomy and Astrophysics, 583, A57.
3. Dobrovolskas, V., Kučinskas, A., Steffen, M., Ludwig, H.-G., **Prakapavičius**, D., Klevas, J., Caffau, E., Bonifacio, P., 2013, *Three-dimensional hydrodynamical* `CO5BOLD` *model atmospheres of red giant stars. III. Line formation in the atmospheres of giants located close to the base of the red giant branch* // Astronomy and Astrophysics, 559, A102.

Other publications in the ISI WoS journals

1. Dobrovolskas, V., Kučinskas, A., Bonifacio, P., Korotin, S. A., Steffen, M., Sbordone, L., Caffau, E., Ludwig, H.-G., Royer, F. **Prakapavičius, D.**, 2014, *Abundances of lithium, oxygen, and sodium in the turn-off stars of Galactic globular cluster 47 Tucanae* // Astronomy and Astrophysics, 565, A121.
2. Kučinskas, A., Steffen, M., Ludwig, H.-G., Dobrovolskas, V., Ivanauskas, A., Klevas, J., **Prakapavičius, D.**, Caffau, E., Bonifacio, P., 2013, *Three-dimensional hydrodynamical CO5BOLD model atmospheres of red giant stars. II. Spectral line formation in the atmosphere of a giant located near the RGB tip* // Astronomy and Astrophysics, 549, A14.

Presentations at the conferences

1. **Prakapavičius D.**, Kučinskas A., Dobrovolskas V., Klevas J., Steffen M., Bonifacio P., Ludwig H.-G., ir Spite M., 2016, *The influence of convection on OH UV line formation in the atmosphere of metal-poor red giant HD 122563* // "`CO5BOLD` Workshop 2016". Naples (Italy), 11–13 April, 2016 (oral presentation by **D. Prakapavičius**);
2. Dobrovolskas, V., **Prakapavičius, D.**, Kučinskas, A., Bonifacio, P., Caffau, E., Ludwig, H.-G., Steffen, M., Spite, M., 2015, *Oxygen in the early Galaxy: abundance studies with 3D hydrodynamical model atmospheres* // ESO workshop "Rainbows on the Southern Sky". Garching (Germany), 5–9 October, 2015 (poster presentation by V. Dobrovolskas);
3. Dobrovolskas, V., Kučinskas, A., Bonifacio, P., Korotin, S. A., Sbordone, L., Caffau, E., **Prakapavičius, D.**, 2013 , *Abundances of lithium, oxygen and sodium in*

the turn-off stars of Galactic globular cluster 47 Tuc // "40th Lithuanian National Physics Conference", Vilnius (Lithuania), 10–12 June, 2013, Programa ir pranešimų tezės, Vilniaus universitetas, 244 p. (poster presentation by V. Dobrovolskas);

4. **Prakapavičius, D.**, Steffen, M., Kučinskas, A., Ludwig, H.-G., Freytag, B., Caffau, E., Cayrel, R., 2012, *Oxygen spectral line synthesis: 3D non-LTE with* `CO`^{5}`BOLD` *hydrodynamical model atmospheres* // "`CO`^{5}`BOLD` Workshop 2012", Heidelberg (Germany), 1–3 October, 2012, Memorie della Societa Astronomica Italiana Supplementi, 24, 111 (oral presentation by **D. Prakapavičius**);
5. Kučinskas, A., Ludwig, H.-G., Steffen, M., Dobrovolskas, V., Klevas, J., **Prakapavičius, D.**, Caffau, E., Bonifacio, P., 2012, *The influence of convection on the atmospheric structures and observable properties of red giant stars* // "`CO`^{5}`BOLD` Workshop 2012", Heidelberg (Germany), 1–3 October, 2012, Memorie della Societa Astronomica Italiana Supplementi, 24, 68 (oral presentation by A. Kučinskas);
6. Klevas, J., Kučinskas, A., Ludwig, H.-G., Bonifacio, P., Steffen, M., **Prakapavičius, D.**, 2012, *Spectral line asymmetries in the metal-poor red giant HD 122563:* `CO`^{5}`BOLD` *predictions versus observations* // "`CO`^{5}`BOLD` Workshop 2012", Heidelberg (Germany), 1–3 October, 2012, Memorie della Societa Astronomica Italiana Supplementi, 24, 78. (oral presentation by J. Klevas).
7. Dobrovolskas, V., Kučinskas, A., Ludwig, H.-G., Caffau, E., Klevas, J., **Prakapavičius, D.**, 2010, *Chemical abundances in metal-poor giants: limitations imposed by the use of classical 1D stellar atmosphere models* // "11th Symposium on Nuclei in the Cosmos", Heidelberg (Germany), 19–23 July, 2010, Proc. of the 11th Symposium on Nuclei in the Cosmos, id.288. (poster presentation by V. Dobrovolskas).

Thesis outline

This Thesis consists of **Introduction**, four **Chapters**, **Conclusions**, **References** and two **Appendices**.

In **Chapter 1** we describe stellar model atmospheres and LTE/NLTE spectral line synthesis codes used in this Thesis.

In **Chapter 2** we present a description of the `NLTE3D` package and its performance tests.

In **Chapter 3** we describe the results obtained during the investigation of atmospheric solar oxygen abundance using 3D hydrodynamical model atmospheres and 3D NLTE spectral synthesis. Results of this investigation were published in Steffen et al. (2015, the second paper in the Section “Publications on the Thesis topic in the refereed journals”).

In **Chapter 4** we summarize the results of investigation of the impact of convection on molecular (CO, OH, C_2, CH, NH, CN) line formation in the atmospheres of red giant stars. Results presented in this Chapter were published in Dobrovolskas et al. (2013, the third paper in the list of refereed papers).

In **Chapter 5** we describe results of the investigation of oxygen abundance in the atmosphere of a metal-poor red giant HD 122563 which was carried out using OH UV lines and 3D hydrodynamical model atmosphere. We also present here the results of our investigation of the influence of convection on the formation of OH UV lines. Results presented in this Chapter are summarized in Prakapavičius et al. (2017, the first paper in the list of referred papers).

In **Conclusions** we briefly summarize the results obtained in this Thesis and outline possible future applications and extension of the work done so far.

In the **Appendices** we list: (a) 3D–1D abundance corrections of molecular (CO, OH, C_2, CH, NH, CN) lines observed in the spectra of the red giant stars (**Appendix A**); (b) parameters of OH UV spectral lines used in the analysis of oxygen abundances in the atmosphere of HD 122563, and individual oxygen abundances determined using different spectral lines (**Appendix B**).

Chapter 1

Model atmospheres and spectral line synthesis

In this Thesis we focus on spectroscopic chemical abundance analysis, which is done by comparing spectral lines observed in the spectra of real stars and those predicted by theoretical models. Theoretical spectral lines have to be computed using physical assumptions regarding the interaction of light and matter (i.e., emission and absorption). One of the main tools used in this analysis is a model atmosphere, which is a theoretical counterpart of the stellar layers that produce and absorb stellar radiation. The realism and reliability of chemical abundance analysis directly relies on realism and assumptions of the model atmosphere.

Another important component of stellar abundance analysis is spectral synthesis. This procedure produces theoretical spectrum, which can be directly compared with the observed spectrum and, by finding a best-match between the two, one can determine chemical composition of the star. Spectral synthesis involves many steps, such as finding number densities of the relevant absorbing chemical species (i.e., atoms, ions, molecules), proper treatment of Doppler shifts and broadening processes, and so on. Again, spectral synthesis that is more realistic from physical point of view should result in more reliable chemical abundances.

In this Chapter we discuss the theoretical tools of spectral abundance analysis – model atmospheres and spectrum synthesis tools – used in this Thesis.

1.1 Model atmospheres

In this Thesis we utilized two types of model atmospheres: classical hydrostatic one-dimensional (1D) model atmospheres; and state-of-the-art hydrodynamical three-dimensional (3D) model atmospheres. Classical 1D model atmospheres are computed using the assumption of the hydrostatic and radiative-convective equilibrium. These simulations are done assuming plane-parallel or spherically-symmetric geometry and thermodynamic quantities are taken to be horizontally homogeneous. Examples of such model atmosphere codes are `PHOENIX` (Hauschildt et al. 1992), `MARCS` (Gustafsson et al. 2008), and `ATLAS9` (Castelli & Kurucz 2004). Radiative transport of energy is treated realistically in the majority 1D model atmosphere codes as there exists extensive databases with accurate radiative opacities. Some of the 1D model atmospheres are sufficiently sophisticated in the sense that they include time-dependent hydrogen ionisation and detailed NLTE radiative transfer. However, they lack physically realistic prescriptions for treating dynamical phenomena, such as convection, shock waves and others.

It is well known that dynamical phenomena, especially convection, play important role in shaping the photospheric structure and determining the physical conditions at which spectral lines are forming (Asplund et al. 1999; Wedemeyer et al. 2004). Classical model atmospheres, by their definition, are not able to account for the horizontal atmospheric inhomogeneities. This means that under such conditions thermodynamic parameters at a single geometrical depth are described by a single value. However, it has been confirmed, both observationally and theoretically, that stellar atmospheres are inhomogeneous as they consist of material moving upwards, downwards and sideways, which may produce shock waves propagating in different directions.

In classical model atmospheres the convective energy transport is usually treated under the framework of the mixing length theory (MLT, Böhm-Vitense 1958) or one of its derivatives (e.g., Canuto et al. 1996). MLT is used to describe convective flux $F_{\rm conv}$ as a function of geometric depth and depends on local quantities, such as pressure scale height and temperature gradient. Obviously, such prescription is not very realistic as MLT attempts at modelling a non-local, hydrodynamic, and multi-dimensional phenomenon by using local parameters and assuming hydrostatic equilibrium.

Treatment of convection under MLT might be questioned in a few ways. First, MLT treatment does not account for overshooting through the classical convective boundary. At the classical Schwarzchild boundary, convective eddies still possess momentum and penetrate into the radiative region, until they're stopped by buoyancy (Nordlund & Dravins 1990). This overshooting influences convective photospheres and spectral line formation in a complicated fashion, as some positive convection-related flux should is always present above the Schwarzchild boundary. The influence of overshooting was investigated by numerous authors and found that inclusion of overshooting, generally, influences temperature structure of the atmosphere as well as its radiative output (see, e.g., Castelli et al. 1997) .

Second, MLT is dependent on a number of free parameters, which have to be calibrated empirically. One of them, the mixing length, $\alpha_{\rm MLT}$, determines the effective scale length for convection. It is a dimensionless quantity that expresses the scale-length of convection in terms of pressure scale height and is usually set by adjusting it in the model of the Sun to reproduce its observed properties. The obtained $\alpha_{\rm MLT}$ is then used to model stars that may be very different from the Sun. However, this approach is not supported by any theory and there are no compelling physical reasons why $\alpha_{\rm MLT}$ should be identical in all types of stars (Freytag & Salaris 1999). Hence, in addition to the lack physical realism of the 1D model atmospheres, the choice of the mixing length parameter frequently lacks adequate justification based on physical reasons.

Moreover, when using 1D model atmospheres, besides $\alpha_{\rm MLT}$, two additional free parameters are required for spectral synthesis: microturbulence ($\xi_{\rm mic}$) and macroturbulence ($\xi_{\rm mac}$) velocities. They are needed because MLT assumes that material is static and carries no information about gas dynamics. These parameters are used to describe photospheric velocity field and related Doppler broadening that would be present in the real atmosphere. One problem with such approach is that identical turbulent velocity is applied for the entire photosphere, even though it may be depth-dependent (see, e.g., Steffen et al. 2013). Secondly, $\xi_{\rm mic}$ and $\xi_{\rm mac}$ are applied as isotropic velocities, while it is well known from the observations (of, e.g., line bisectors; see Nordlund & Dravins 1990) that the photospheric material moves asymmetrically. These assumptions inevitably lead to additional uncertainties and systematics.

Inability to account for the dynamical phenomena and horizontal inhomogeneities (or, in general, 3D hydrodynamical effects) in realistic manner, as well as for inconsistencies of MLT, may lead towards large systematic effects in the derived chemical abundances. Pioneering work of Collet et al. (2007), who investigated 3D effects on spectral line formation by using 3D model atmospheres of the red giant branch (RGB) stars, have found that lines of many chemical elements are prone to the 3D hydrodynamical effects. It was found that these effects, in the presence of horizontal inhomogeneities, tend to strengthen spectral lines which, in turn, leads to higher abundances determined using 1D hydrostatic model atmospheres. These results were subsequently confirmed by Kučinskas et al. (2013) and Dobrovolskas et al. (2013) who studied objects in a wider range of atmospheric parameters typical to RGB stars. It was found that the abundances obtained using 3D and 1D model atmospheres may reach –0.6 dex (meaning that 3D hydrodynamical model atmospheres predict lower abundances). Resonance spectral lines of the chemical species that are in the minority ionization stage are especially influenced by the 3D hydrodynamical effects since they form in the a strong influence on the layers where the horizontal fluctuations are most pronounced.

1.1.1 3D hydrodynamical `CO⁵BOLD` model atmospheres

As discussed above, convection has a strong influence on the properties of the photosphere where the spectrum emitted by the star is forming. Since convection is a dynamical and multi-dimensional phenomenon, it needs to be treated adequately. In this Thesis we used three-dimensional hydrodynamic model atmospheres that were computed with the $\mathtt{CO^5BOLD}$ code (Freytag et al. 2012). Since all $\mathtt{CO^5BOLD}$ model atmospheres used in this work share similar qualities, in this Section we describe them in general terms and, in the upcoming applications of these model atmospheres, we simply point to the particular details of the models used in those Sections.

$\mathtt{CO^5BOLD}$ model atmosphere code solves the coupled non-linear equations of compressible hydrodynamics in an external gravity field, together with radiative transfer equation. Hydrodynamic equations solved by $\mathtt{CO^5BOLD}$ are (Freytag et al. 2012) :

$$\frac{\partial \rho}{\partial t} + \frac{\partial \rho v_x}{\partial x} + \frac{\partial \rho v_y}{\partial y} + \frac{\partial \rho v_z}{\partial z} = 0 \tag{1.1}$$

$$\frac{\partial}{\partial t}\begin{pmatrix} \rho v_x \\ \rho v_y \\ \rho v_z \end{pmatrix} + \frac{\partial}{\partial x}\begin{pmatrix} \rho v_x v_x + P \\ \rho v_y v_x \\ \rho v_z v_x \end{pmatrix} + \frac{\partial}{\partial y}\begin{pmatrix} \rho v_x v_y \\ \rho v_y v_y + P \\ \rho v_z v_y \end{pmatrix} + \frac{\partial}{\partial z}\begin{pmatrix} \rho v_x v_z \\ \rho v_y v_z \\ \rho v_z v_z + P \end{pmatrix} = \rho g \tag{1.2}$$

$$\frac{\partial \rho E}{\partial t} + \frac{\partial (\rho E + P) v_x}{\partial x} + \frac{\partial (\rho E + P) v_y}{\partial y} + \frac{\partial (\rho E + P) v_z}{\partial z} - Q_{\mathrm{rad}} = 0 \tag{1.3}$$

ρ is density, v_{i} is velocity component in the direction i, P stands for pressure, g is gravitational acceleration, E is the total energy density per unit mass (i.e., including internal, kinetic and gravitational energy terms), and Q_{rad} is a radiative energy exchange term. Internal energy, E_{int}, ρ and P are coupled via precomputed equation of state. These equations account for conservation of mass, momentum, and energy, respectively.

Equations of hydrodynamics are coupled to the radiation transfer via $Q_{\rm rad}$ that is defined as

$$Q_{\rm rad} = -\nabla \cdot F_{\rm rad} \tag{1.4}$$

where F_{rad} is radiative flux, a frequency and angle-integrated monochromatic radiative intensity $I_{\mu\lambda}$. The latter is defined for a single inclination angle $\mu \equiv cos(\theta)$, where θ is an angle between the ray and z-axis (directed outwards), and wavelength λ. It is computed by utilizing long characteristics scheme[1] to solve the radiation transport equation

$$\mu \frac{dI_\lambda(\mu,\tau_\lambda)}{d\tau_\lambda} = I_\lambda(\mu,\tau_\lambda) - S_\lambda(\tau_\lambda) \tag{1.5}$$

where $\tau_\lambda \equiv \int_0^z \kappa_\lambda dz$ is monochromatic optical depth and S_λ is the source function. In the model atmospheres used in this Thesis the source function was computed under the assumption of LTE, scattering was treated as true absorption, so S_λ was set to the local Planck's function $B_\lambda(T)$.

To obtain a realistic representation of the $F_{\rm rad}$, this equation should be solved for a number of inclination angles and wavelength points. Usually, $I_{\mu\lambda}$ is computed for four azimuthal angles ϕ and two + vertical inclination angles θ. Angle-averaging is done with Lobatto-type integration where the intensity computed for each inclination angle is assigned a pre-computed weight and contributions at all angles are summed up.

Wavelength-dependency of $F_{\rm rad}$ is taken into the account by using monochromatic opacities from the `MARCS` stellar atmosphere package (Gustafsson et al. 2008). Radiative opacities are computed by adopting solar-scaled chemical composition published in Asplund et al. (2005). In cases of $[\mathrm{M/H}] \leq -1.0$, we apply a constant enhancement in alpha-element abundances $[\alpha/\mathrm{Fe}] = +0.4$. However, since there are millions of lines in the spectra of cool stars, wavelength dependency of κ_λ is very complex to account for and solution in a multi-dimensional environment is beyond the current computational capabilities. However, $Q_{\rm rad}$ can be evaluated with reasonable accuracy without accounting for a detailed dependency of κ_λ on λ. Because of this, one can simplify the problem by making use

---

[1] Solution of radiation transport by using long characteristics scheme is based on a concept of long rays that extend from the top to bottom of the computational domain. Since the inclined radiation rays pass between computational grid points, relevant physical quantities (opacity and source function) are interpolated between radiation ray and 3D grid (see Freytag et al. 2012).

of the opacity-binning scheme (Nordlund 1982; Ludwig et al. 1994; Vögler et al. 2004) and significantly reduce the required computational time. Result of this simplification is that the radiative transport needs to be solved once per opacity bin and not for the many wavelength points spanning over the entire spectrum.

All 3D hydrodynamical model atmospheres used in this Thesis were computed in a “box-in-a-star” set-up which means that only a fraction of the stellar surface is simulated. Such set-up utilises the following boundary conditions:

- open boundary conditions are set vertically. Matter and radiation is allowed to flow in and out of the box and the total is conserved. Free parameters control the temperature of inflowing matter pressure and optical depth scale heights at the top boundary of the model atmosphere. Entropy of the inflowing material ($S_{\rm bot}$) is set at the lower boundary and, in effect, controls the outgoing radiative flux and the effective temperature of the model atmosphere.
- periodic boundary conditions are applied laterally. Matter and radiation rays that exit the model box non-vertically enter the box on the other side.

In order to gather statistically representative sample, all model calculations are continued until the sequence of hydrodynamic simulations reaches time-span of ≈10–20 convective turnover times. Since the 3D spectral synthesis computations (especially in NLTE) are computationally expensive, it would be time-consuming to utilize all ($\approx$ 400) 3D snapshots[2]. In order to lower the computational costs, a smaller sub-sample of model snapshots is selected and used in the spectral line synthesis computations. In all cases, these sub-samples consist of 20 snapshots. When selecting a sub-sample of snapshots, one tries to preserve certain properties the original (full) snapshot ensemble: average effective temperature and its standard deviation, mean velocity at optical depth unity, mean velocity profile and mean mass velocity profile. Fig. 1.1 shows radiative flux of a sample model run and depicts the snapshots chosen according to the mean properties of the entire simulation. It was argued previously (Caffau 2009; Ludwig et al. 2009) that such subsample of model atmospheres represents the entire sample in terms of spectral line properties reasonably well.

An additional comment on the lower boundary condition should be made at this point. Since the outgoing radiative flux is controlled via free parameter $S_{\rm bot}$,

---

[2] a snapshot of a 3D hydordynamical model atmosphere is thermodynamic and hydrodynamic configuration of the model atmosphere at a single instance of time

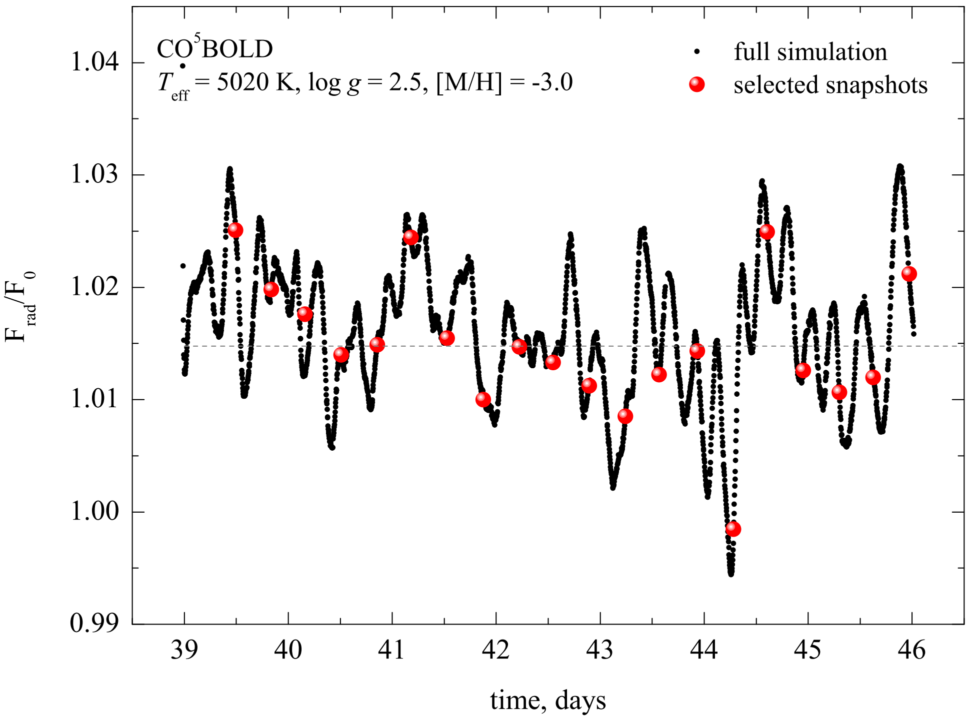

Fig. 1.1. Temporal evolution of the outgoing flux normalized to the nominal flux (corresponding to $T_{\rm eff} = 5020\,{\rm K}$) for the model atmosphere with $T_{\rm eff} = 5020\,{\rm K}$, $\log g = 2.5\,[{\rm cgs}]$ and $[{\rm M/H}] = -3$. Red dots mark the selected sub-sample consisting of 20 3D snapshots (see text for details). This figure was kindly provided by V. Dobrovolskas.

one has to fine-tune the latter in order to achieve the required flux at the top of the atmosphere that corresponds to the nominal $T_{\rm eff}$. After changing $S_{\rm bot}$, the simulation has to relax to the quasi-stable state and new $T_{\rm eff}$. Because of this reason, model atmospheres used in this Thesis may have mean $T_{\rm eff}$ that are slightly off the target value. It should also be mentioned that the radiative flux of the model atmospheres experiences temporal fluctuations due to stochastic nature of convection (Fig. 1.1), resulting in the fluctuating $T_{\rm eff}$. Note, however, that differences between the average $T_{\rm eff}$ of individual 3D snapshots are always small ($\lesssim 40\,{\rm K}$), and the average effective temperatures of all model atmospheres are very close to their target values.

Finally, by horizontally and temporally averaging the temperature (T^4) and gas pressure (P) on surfaces of constant optical depth ($\tau_{\rm Ross}$) the average $\langle 3{\rm D}\rangle$ model is obtained. The $\langle 3{\rm D}\rangle$ model is a 1D atmosphere representing the mean properties of the 3D model (cf. Fig. 3.1). Comparison of the line formation properties of the full 3D and the $\langle 3{\rm D}\rangle$ model gives an indication of the importance of horizontal inhomogeneities in the process of line formation (see, e.g., Sect. 5.5.2 for details).

1.1.2 1D hydrostatic model atmospheres

In this Thesis we also use 1D model atmospheres computed with the `LHD` code (Caffau & Ludwig 2007). This code solves equations of radiation hydrodynamics on one-dimensional plane-parallel grid. Equations describing stellar structure are formulated in Lagrangian form, while radiation transfer is solved using the same scheme as used in the $\mathtt{CO}^5\mathtt{BOLD}$ package (see previous Section). `LHD` model atmospheres utilize MLT in the formalism of Mihalas (1978) and an additional free parameter – mixing length, α_{MLT} – to control the efficiency of convection in the given model atmosphere. Also, model atmospheres computed with the `LHD` code use the same equation of state, radiative transfer and opacity binning schemes as those implemented in the $\mathtt{CO}^5\mathtt{BOLD}$ package. Such approach is useful for the comparison of internal structures and observable properties of $\mathtt{CO}^5\mathtt{BOLD}$ and `LHD` model atmospheres (see, e.g., Chapter 4).

We have also used 1D hydrostatic model atmospheres computed with the `ATLAS9` code (Kurucz 1970), one of the most popular classical one-dimensional hydrostatic stellar model atmosphere codes. `ATLAS9` model atmospheres are computed using the assumption of hydrostatic equilibrium. Also, these model atmospheres are computed by utilizing a more detailed radiative transfer than that utilized in the computations of 3D hydrodynamical models, which in `ATLAS9` is solved by using opacity distribution functions (ODFs). Such approach is more precise because, instead of using a small number of opacity bins (see Sect. 1.1.1), it samples line opacity at a much higher number of wavelength points (337 wavelength points, see Castelli & Kurucz 2003). Hence, `ATLAS9` model atmospheres are more suitable to be used in the abundance analysis (see Chapter 5) while `LHD` model atmospheres were used only to perform a differential analysis, in order to estimate the role of hydrodynamical effects in the spectral line formation (see Chapter 5).

1.2 Spectral line synthesis

1.2.1 3D NLTE spectral synthesis

In order to perform spectral line synthesis computations that are needed for stellar abundance analysis, one needs to determine the the line opacity and source function. This is usually done under the assumption of local thermodynamic equilibrium (LTE). Such approach is relatively straightforward since the population numbers of the lower and upper atomic levels (that control line opacity and source function) of particular radiative transition are then a sole function of the local temperature and can be computed using the Saha-Boltzmann equation. Such approach assumes that the radiation experienced by the matter is of local origin and is described by the Planck's function. This, however, is not nescessarilly true in reality since spectral lines are forming in the optically thin stellar regions and the temperature may change significantly along the mean free path of a photon.

Under such conditions, the matter will experience different radiation field from the one expected under LTE. Such radiation field may induce additional excitation or de-excitation, modify the population numbers of the lower and upper atomic levels of a given atom or molecule, and influence the synthetic spectral line profile. Moreover, non-local radiation field may drive the ionization balance of chemical species away from the LTE expectation.

In order to account for non-local nature of radiation field, the assumption of non-local thermodynamic equilibrium (NLTE) is used. Under this assumption, one simultaneously accounts for a number of radiative and collisional processes (both bound-bound and bound-free) in a system called model atom. By modelling radiative and collisional transitions in the model atom and solving a system of equations called statistical equilibrium, it is possible to derive population numbers of all modelled atomic levels, including those participating in a transition of interest.

It has been found repeatedly that if departures from LTE (further, NLTE effects) are taken into account during the line synthesis computations, this may have a significant impact on the resulting abundance estimates. Recent estimates of the differences between NLTE and LTE oxygen abundance estimates obtained in different types of stars/stellar atmospheres range between –0.8 and –0.1 dex (Fabbian et al. 2009, 1D NLTE) or –0.5 and 0.0 dex (Amarsi et al. 2015, 3D NLTE), depending on the stellar parameters (especially metallicity) and the oxygen abundance.

However, it is of utmost importance to stress that the reliability of the NLTE abundance analysis strongly depends on the realism of the model atmospheres that are used in the computation of NLTE spectral line profiles. The classical 1D hydrostatic model atmospheres that are used in stellar abundance work suffer from several major drawbacks (see Sect. 1.1). Hence, NLTE spectral line synthesis should be combined with the most physically realistic 3D hydrodynamical model atmospheres. This is especially important in the low-metallicity regime where the lack of line blanketing may cause severe overionization while horizontal fluctuations of thermodynamic and hydrodynamical quantities are largest and thus may have a direct influence on the number densities of chemical species at in the atmosphere (see, e.g., Chapter 4).

As a first step towards computing 3D/1D NLTE spectral line profiles, we compute level departure coefficients b_i[3], using `NLTE3D` code, 3D/1D model atmospheres described in the previous Sections, and a model atom of a given chemical element whose abundance needs to be determined (see Sect. 3.4.1).

First, `NLTE3D` computes the line-blanketed radiation field that is required for the calculation of the photoionization transition probabilities. For this task, we utilized the `ATLAS9` line opacity distribution functions from Castelli & Kurucz (2004) and the continuum opacities from the `IONOPA` routines, a part of the Kiel and `CO`^{5}`BOLD` atmosphere packages. The properties of the radiation field are computed using the method of long characteristics where the radiative transfer equation is solved using a modified Feautrier scheme.

Based on this 3D line-blanketed radiation field, we then compute the photoionization and photorecombination transition probabilities. They are assumed to be independent of possible departures from LTE in the level population of a chemical element in question. Then, `NLTE3D` computes the angle-averaged continuum intensities, $J_{\rm cont}$, at the central wavelength of all of the line transitions. If a particular spectral line is weak, the profile averaged mean line intensity, $\bar{J}$, is set to $J_{\rm cont}$, and the radiative bound-bound transition probabilities of these lines are only computed once. Finally, we compute the collisional transition probabilities, which depend only on the local temperature. All of those transition probabilities are fixed, as they do not depend on the departure coefficients. In this situation, if all considered spectral lines are weak, the solution for statistical equilibrium equations is straightforward, and the departure coefficients of all levels can be obtained immediately, i.e., without any iterative procedure.

However, as soon as the line transitions are no longer optically thin, the mean radiative line intensities, $\bar{J}$, and the departure coefficients, b_i, become strongly coupled in a non-linear way. In this case, one must compute $\bar{J}$ as the weighted average of J_ν over the local line profile, taking into account that line opacity and source function depend on the departure coefficients of the energy levels

---

[3] Level departure coefficient, b_i, is defined as an NLTE-to-LTE ratio of populations (n_i and n_i^* respectively), for the atomic level i; $b_i = n_i/n_i^*$.

of the transition. In the present version of `NLTE3D`, the local line profile is assumed to be Gaussian, representing the thermal line broadening plus the effect of microturbulence. In the present version of the `NLTE3D` code, the 3D hydrodynamical velocity field is not used, so Doppler shifts along the line of sight are ignored. Instead, the velocity field is represented by a depth-independent microturbulence. Radiative damping, as well as van der Waals and Stark broadening, are also ignored. We verified that this simplification has a negligible influence on the resulting departure coefficients. In the spectral line synthesis computations, however, the line broadening is treated in full detail and includes the effects of the 3D hydrodynamical velocity field (see below).

Since it would be very computationally expensive to use complete linearization methods (Auer 1973; Kubát 2010, Sect. 8) with 3D hydrodynamical model atmospheres, we choose to iterate between the mean radiative line intensities and departure coefficients. However, as discussed by Prakapavičius et al. (2013), ordinary Λ-iteration scheme converges poorly when departure coefficients for oxygen are computed with the `NLTE3D` code and this may lead to erroneous results. Hence, we implemented the ALI scheme of Rybicki & Hummer (1991, Sect. 2.2) to achieve the solution of required precision faster.

Iterations are started using LTE line opacities and source functions from which the mean line intensities, $\bar{J}$, radiative transition probabilities, and equivalent widths of the emergent flux line profiles are calculated. Then, all previously computed transition probabilities are fed into the equations of statistical equilibrium which are solved for the unknown departure coefficients. Using the computed departure coefficients, the NLTE line opacities and source functions are computed and the radiation transfer is solved for all strong lines using these quantities. Then the $\bar{J}$, flux Ws, and approximate Λ-operators (Λ^*) are recomputed with NLTE line opacities and source functions. The updated mean radiative intensities enter the equations of statistical equilibrium and the cycle begins again.

The ALIs are continued until the relative changes (from one iteration to the next) in the flux Ws of all sufficiently strong lines have converged to a prescribed value (usually, 10^{-3}–10^{-5}). After convergence, departure coefficients of all levels that were included in the model atom are saved to the output file for the subsequent analysis and/or spectral line synthesis with `Linfor3D` (see next Section).

1.2.2 Spectral line synthesis with the `Linfor3D` package

Second step in the computation of synthetic spectral lines, is the spectrum synthesis itself. All spectral synthesis calculations with `CO`^{5}`BOLD` and `LHD` model atmospheres were performed using the `Linfor3D`[4] package. It should be noted that `Linfor3D` , at first, was designed and made for the computation of LTE line profiles and most of what follows below applies to LTE case as well.

In the first place, `Linfor3D` computes LTE populations of the upper and lower levels involved in a particular transition using Saha-Boltzmann equation and IONDIS package[5]. Further, `Linfor3D` estimates LTE line opacity, $\kappa_{\rm LTE}(\nu)$, and source function, $S_{\rm LTE}(\nu)$. If NLTE spectral synthesis is requested, then previously computed departure coefficients are used in order to compute NLTE line opacity, $\kappa_{\rm NLTE}(\nu)$, and line source function, $S_{\rm NLTE}(\nu)$, according to

$$\frac{\kappa_{\rm NLTE}(\nu)}{\kappa_{\rm LTE}(\nu)} = b_{\rm l}\,\frac{\exp(\frac{h\nu}{kT}) - (b_{\rm u}/b_{\rm l})}{\exp(\frac{h\nu}{kT}) - 1} \tag{1.6}$$

and

$$\frac{S_{\rm NLTE}(\nu)}{S_{\rm LTE}(\nu)} = \frac{\exp(\frac{h\nu}{kT}) - 1}{(b_{\rm l}/b_{\rm u})\,\exp(\frac{h\nu}{kT}) - 1} \tag{1.7}$$

respectively. In these equations, $b_{\rm l}$ and $b_{\rm u}$ are the departure coefficients of the lower and upper level of a particular transition, respectively.

Using these quantities, and continuum opacity from the IONOPA package, radiative intensities are computed using long characteristics method. Radiative transfer is usually computed for 150−200 wavelength points per line profile. Radiative intensities are averaged over all azimuthal directions. If flux spectrum is requested, spectral intensity lines are added up using Gauss-Lobatto integration scheme in order to obtain disk-integrated flux profile.

Since 3D hydrodynamical model atmospheres consist of a number of snapshots that represent photospheric structure at different instances of time (see Sect. 1.1.1), spectral synthesis is performed using each individual 3D snapshot. The spectral line profiles obtained using all individual snapshots are then co-added to obtain the final 3D line profile.

---

[4] http://www.aip.de/~mst/linfor3D_main.html

[5] Since this package is also utilized in the `NLTE3D` code, LTE populations are identical and consistent in both calculations of departure coefficients and spectrum synthesis.

In addition to the 3D model atmospheres, `Linfor3D` computes spectral line profiles using averaged ⟨3D⟩ model atmospheres. These model atmospheres are computed by horizontally averaging each 3D snapshot on surfaces of equal optical depth. Similarly to the 3D case, ⟨3D⟩ synthetic spectrum is calculated for every horizontally averaged 3D snapshot and the final ⟨3D⟩ line profile is then obtained by co-adding all individual line profiles. It should be mentioned that every ⟨3D⟩ model atmosphere is one-dimensional structure, hence the average ⟨3D⟩ models do not contain information about the horizontal or temporal fluctuations of thermodynamic quantities and velocity fields. Therefore, by comparing the predictions of average ⟨3D⟩ models with those of 3D model atmospheres, one is able to assess the role of horizontal fluctuations in the spectral line formation.

Finally, it is also possible to use `Linfor3D` with 1D reference model atmospheres in order to compute 1D spectra for the comparison with the 3D and ⟨3D⟩ results. For this, we used model atmospheres computed with the `LHD` code (Sect. 1.1.2). We stress again that `LHD` model atmospheres do not contain any information about hydrodynamics and velocity fields. Also, macroturbulence velocity is used in order to account for additional broadening due to large scale motions in the atmosphere.

Chapter 2

`NLTE3D` code: physics, implementation, and tests

2.1 Introduction

As discussed in Sect. 1.2.1, if NLTE effects are taken into account during the line synthesis computations, abundance estimates might be significantly different from the LTE expectation. Since radiation that illuminates line-forming atmospheric layers may form deeper in the atmosphere and at higher temperatures, it is expected to influence local ionization and excitation balance of chemical species in question. Such influence, in turn, will modify local quantities that govern interaction between matter and radiation – line opacity and source function – and will finally influence the resulting line profile. Non-local nature of radiation relevant for the formation of a given spectral line may be accounted for via simultaneous modelling of radiative and collisional processes within a system called model atom.

However, the reliability of NLTE spectrum synthesis depends on the realism of the model atmosphere that is utilized for the spectrum synthesis. It was already discussed in Sect. 1.1, classical 1D model atmospheres are limited in various ways and thus certain observable properties of stars can only be replicated with the help of state-of-the-art 3D hydrodynamical model atmospheres. The latter are much more realistic than their 1D counterparts. In this sense, it is perhaps the most important that convection in the 3D hydrodynamical atmospheres is modelled from the first principles, without resorting to various simplified schemes such as MLT. Amongst other things, this naturally leads to the appearance of the granulation pattern and horizontal inhomogeneities of hydrodynamical and thermodynamic quantities. It is well known from observations that granulation pattern appears on the stellar surface as a consequence of convection and may thus have a direct influence on spectral line formation. Finally, dynamical phenomena, such as acoustic and shock waves, emerge naturally in the 3D model atmospheres, whereas classical 1D hydrostatic model atmospheres are unsuitable for this task.

Hence, realistic NLTE spectral synthesis should be performed by using 3D model atmospheres. The `NLTE3D` package is well suited for this task. In this Chapter we describe the physical foundations of the `NLTE3D` package, outline the flow of the code, and provide test results of the ALI scheme.

2.2 Formulation of the NLTE problem

In order to solve the problem of non-local radiative transfer, assumption of the statistical equilibrium is used. Statistical equilibrium is defined as a state of the model atom in which the level populations are such that the net rate of all transitions (collisional, radiative, upward, downward, bound-bound, bound-free) from each level is zero. This means that processes that populate each level must be counter-balanced by the depopulating processes. This condition for level i can be written as

$$n_i[\sum_{j\neq i}(R_{ij} + C_{ij}) + R_{ik} + C_{ik}] = \sum_{i\neq j} n_j(R_{ji} + C_{ji}) + R_{ki} + C_{ki} \tag{2.1}$$

where n_i is the NLTE population of the level i and R_{ij} and C_{ij} are radiative and collisional transition probabilities for transition between levels i and j, respectively. If $i < j$, then such transition deals with excitation and vice versa. Level k denotes continuum and all such transitions deal with ionization or recombination. The terms on left-hand side of the latter equation account for the depopulation of the level i, while processes described on the right-hand side populate the level i in terms of the transitions from the level j. Such condition must be simultaneously met for the each level of the model atom and form a system of equations linear in unknown n_i.

When $i < j$, radiative transition probability that enters the equation is defined as

$$\begin{aligned} R_{ij} &= B_{ij}\bar{J}_{ij} \\ R_{ji} &= A_{ji} + B_{ji}\bar{J}_{ji}. \end{aligned} \tag{2.2}$$

First equation describes the radiative excitation, the second equation – de-excitation and include terms for spontaneous and induced emission, B_{ij}, A_{ji} and B_{ji} denote Einstein coefficients for absorption, spontaneous emission and stimulated emission, respectively, and $\bar{J}_{ij}$ is the mean radiation intensity. $\bar{J}_{ij}$ is defined as an angular- and frequency- integral of the intensity $I_{\mu\nu}$

$$\bar{J}_{ij} = \int_0^{\infty} \frac{1}{4\pi} \int_0^{4\pi} I_{\mu\nu}\phi_{ij}(\mu, \nu) d\Omega d\nu = \int_0^{\infty} J_\nu \phi_{ij}(\nu) d\nu \tag{2.3}$$

where ϕ_{ij} is normalized absorption (or emission) line profile. If one assumes equality of absorption and emission profiles (complete frequency redistribution), $\bar{J}_{ij} = \bar{J}_{ji}$ and the same quantity enters both equations in expression (2.2).

Upward transition probability for inelastic collisions with particle X, C_{ij} ($i < j$), is defined as

$$C_{ij} = N_X \int_{E_0}^{\infty} f(E) E \sigma_{ij}(E) dE = N_X < \sigma E >_{ij} \tag{2.4}$$

where N_X is the concentration of particle X (usually, only hydrogen and electrons are considered), $f(E)$ – Maxwell-Boltzmann function and $\sigma_{ij}(E)$ – collisional cross section for the upward transition between levels i and j at impact energy E. The integral in this equation, integrated from the threshold energy E_0 up to infinity, is also known as the collision rate coefficient $< \sigma E >_{ij}$.

Definition of the downward collisional transition probability, C_{ji}, stems from the argument of detailed balance, which states that $n_i^* C_{ij} = n_j^* C_{ji}$, where n_i^* is LTE population of the level i. It may be shown that

$$C_{ji} = \frac{n_i^*}{n_j^*} C_{ij} = \frac{g_i}{g_j} e^{\frac{E_{ij}}{kT}} C_{ij} \tag{2.5}$$

where g_i is the statistical weight of the level i, E_{ij} is the energy difference between levels i and j, k is Boltzmann constant and T is local temperature. If such approach is utilized, one only needs to evaluate of the upward collisional transition probability, while the downward transition probability can be obtained by utilizing the assumption of detailed balance.

In order to simplify the expressions for radiative transition probabilities, Eq. (2.2), and the equation of statistical equilibrium itself, we use the well known relations between the Einstein coefficients. We express all Einstein coefficients in terms of Einstein coefficient for absorption B_{ij} ($i < j$) and noting that NLTE population numbers can be defined as $n_i = n_i^* b_i$, we arrive at the following expression

$$\begin{aligned} & n_i^* b_i \Big[\sum_{i>j} \frac{g_j B_{ji}}{g_i}(k_{ij} + \bar{J}_{ij}) + \sum_{i<j} B_{ij}\bar{J}_{ij} + \sum_{i\neq j} C_{ij} + R_{ik} + C_{ik}\Big] = \\ & \sum_{j>i} n_j^* b_j \frac{g_i B_{ji}}{g_j}(k_{ij} + \bar{J}_{ij}) + \sum_{j<i} n_j^* b_j \bar{J}_{ij} + \sum_{j\neq i} n_j^* b_j C_{ji} + R_{ki} + C_{ki}. \end{aligned} \tag{2.6}$$

In this equation the original sums of equation (2.1) were split into two components, $j < i$ and $j > i$, in order to account for excitation and de-excitation processes that are defined in a different way (Eq. (2.2)).

Dividing Eq. (2.6) by n_i^* and expressing n_j^*/n_i^* as Boltzmann ratio, we arrive at the final form of the statistical equilibrium equation

$$\begin{aligned} & b_i \Big[\sum_{i>j} \frac{g_j B_{ji}}{g_i}(k_{ij} + \bar{J}_{ij}) + \sum_{i<j} B_{ij}\bar{J}_{ij} + \sum_{j\neq i} C_{ij} + R_{ik} + C_{ik}\Big] - \\ & \qquad \sum_{j>i} b_j B_{ij}(k_{ij} + \bar{J}_{ij}) e^{-\frac{h\nu_{ij}}{kT}} - \sum_{j<i} b_j \frac{g_j B_{ji}}{g_i} \bar{J}_{ij} e^{\frac{h\nu_{ij}}{kT}} - \\ & \qquad \qquad \sum_{j\neq i} b_j C_{ji} = R_{ki} + C_{ki}. \end{aligned} \tag{2.7}$$

Solution of this equation for the unknown b_i requires knowledge of mean radiation intensity across the spectral line profiles, photoionizing radiation field, and photoionization cross sections, collisional cross sections for the computation of the collisional rates of interest and precise atomic data (e.g., level energies and Einstein coefficients). Once all these quantities are known, this equation can be solved for multi-level model atom for the unknown departure coefficients (see Sect. 2.4).

2.3 Accelerated Λ-iteration scheme

Previously described terms are sufficient in order to solve equations of statistical equilibrium by using ordinary Λ-iteration scheme. This scheme is iterated as follows: initially, one estimates the formal solution of the radiation field at line wavelengths ($\bar{J}_{ij}$) where the line opacity and source function are calculated by using level populations derived in the previous iteration. Newly computed radiative transition probabilities R_{ij} (Eq. 2.2) for bound-bound transitions enter the equations of statistical equilibrium, a new iterate of level populations is computed and the cycle begins again using updated level populations.

This scheme, for a single unidirectional monochromatic radiation intensity (that enters the expression for $\bar{J}_{ij}$ in equation 2.3) $I_{\mu\nu}$, can be written as a following operator equation:

$$I_{\mu\nu} = \Lambda_{\mu\nu}[S^{\dagger}_{\mu\nu}] \tag{2.8}$$

where $\Lambda_{\mu\nu}$ is the exact Λ-operator and $S^{\dagger}_{\mu\nu}$ is the estimate of the line source function obtained 'old' level populations from the previous iteration. Eq. (2.8) can then be averaged over all angles and frequencies (Eq. 2.3) and resulting $\bar{J}_{ij}$ can enter the equations of statistical equilibrium (Eq. 2.7).

Although this scheme is conceptually simple, it is known that it converges slowly in the line-forming regions at the optically thick wavelengths, such as in the cores of strong lines. To quote Rybicki & Hummer (1991): "Each cycle of [Λ-]iteration corresponds to photons moving about one mean free path in the medium. In the cores of strong lines photons have very short mean free paths, and this implies that many iterations are required to move them any substantial distance". Also, "it exhibits a pathological behaviour in that the solution stabilizes (i.e. relative changes of the source function become extremely small) long before the correct solution is reached" (Hubeny 2003). Hence, a high number of iterations is needed in order to cover the whole model atmosphere and converge to a final solution. This obstacle can be overcome by utilizing a more sophisticated class of iteration methods, ALI.

The ALI method, besides the computation of the formal solution $\bar{J}^{\dagger}_{ij}$ by using the exact Λ-operator Λ_{ij}, involves evaluation of the approximate Λ-operator. With this approach, the operator equation for a single radiation ray is written as

$$I_{\mu\nu} = \Lambda^{*}_{\mu\nu}[S_{\mu\nu}] + (\Lambda_{\mu\nu} - \Lambda^{*}_{\mu\nu})[S^{\dagger}_{\mu\nu}] \tag{2.9}$$

where $\Lambda^{*}_{\mu\nu}$ is the approximate Λ-operator and $S_{\mu\nu}$ is the 'new' iterate of the source function that involves unknown departure coefficients (Cannon 1973). Here $\Lambda^{*}_{\mu\nu}$ *implicitly* relates intensity and source function. If $\Lambda^{*}_{\mu\nu}$ is realistic, then $I_{\mu\nu}$ is expected to converge on the exact solution much faster.

Also, it can be seen that, upon convergence, when $S_{\mu\nu} = S^{\dagger}_{\mu\nu}$, the approximate terms in the Eq. (2.9) cancel and this equation reduces to Eq. (2.8). This shows that both equations should yield identical results as long as convergence is reached.

Besides application of $\Lambda^{*}_{\mu\nu}$, ALI method is iterated by using a modified (so-called preconditioned) version of the equations of statistical equilibrium. We base our ALI scheme on the work of Rybicki & Hummer (1991), who, in their Section 2.2, presented an elegant ALI scheme for the case of multi-level model atom with the inclusion of background continuum opacity.

The equation that was described in the Sect. 2.2 treats departure coefficients as unknowns, while in the prescription of Rybicki & Hummer (1991) NLTE level populations are unknown. In the light of the formalism used in the `NLTE3D` code, the preconditioned equation of statistical equilibrium described in Rybicki & Hummer (1991) needs to be modified and the unknowns need to be changed. We derive the preconditioned equation of statistical equilibrium that is based on departure coefficients below.

We rearrange equation (2.7) to arrive at

$$\begin{aligned} &\sum_{j<i} \frac{g_j B_{ji}}{g_i} \left[b_i k_{ij} - \left(b_j e^{\frac{h\nu_{ij}}{kT}} - b_i \right) \bar{J}_{ij} \right] \\ &- \sum_{j>i} B_{ij} e^{-\frac{h\nu_{ij}}{kT}} \left[b_j k_{ij} - \left(b_i e^{\frac{h\nu_{ij}}{kT}} - b_j \right) \bar{J}_{ij} \right] \\ &+ \sum_{j\neq i} (b_i C_{ij} - b_j C_{ij}) - R_{ki} + b_i R_{ik} - C_{ki} + b_i C_{ik} = 0 \end{aligned} \tag{2.10}$$

According to the prescription of Rybicki & Hummer (1991), we now write $\bar{J}_{ij}$ as

$$\bar{J}_{ij} = \bar{J}^{\dagger}_{ij} + \Lambda^{*}_{ij} S_{ij} - \Lambda^{*}_{ij} S^{\dagger}_{ij} \equiv \Lambda^{*}_{ij} S_{ij} + J^{\mathrm{eff}}_{ij} \tag{2.11}$$

where we have defined J^{eff}_{ij} as

$$J^{\mathrm{eff}}_{ij} = \bar{J}^{\dagger}_{ij} - \Lambda^{*}_{ij} S^{\dagger}_{ij} \tag{2.12}$$

Note that $J_{ij}^{\rm eff}$ contains only 'old' (known) quantities. The line source function S_{ij} for the transition between the lower level i and upper level j is defined as

$$S_{ij} = \frac{n_j A_{ji}}{n_i B_{ij} - n_j B_{ji}} \tag{2.13}$$

Note that this line source function contains the 'new' (unknown) level populations and preservation of linearity in Eq. (2.7) must be given extra attention.

We insert definition of the departure coefficient in to the Eq. (2.13), so the latter is expressed in terms of LTE populations and departure coefficients, while all Einstein coefficients are expressed in terms of B_{ij}

$$S_{ij} = \frac{b_j k_{ij} \frac{g_i}{g_j} B_{ij}}{b_i \frac{g_i}{g_j} B_{ij} e^{\frac{h\nu_{ij}}{kT}} - b_j \frac{g_i}{g_j} B_{ij}} = \frac{b_j k_{ij}}{b_i e^{\frac{h\nu_{ij}}{kT}} - b_j}. \tag{2.14}$$

Note again that S_{ij} and $J_{ij}^{\rm eff}$ in this form are defined only for $i < j$.

By inserting $\bar{J}_{ij}$, defined in Eq. (2.11), and S_{ij}, defined in Eq. (2.14), into Eq. (2.10) and rearranging the resulting equation, we arrive at the final form of preconditioned equations of statistical equilibrium that is based on departure coefficients:

$$\begin{aligned} b_i \left[R_{ik} + \sum_{j<i} \frac{g_j B_{ji}}{g_i} \left(k_{ij}(1 - \Lambda_{ji}^*) + J_{ji}^{\rm eff} \right) + \sum_{j>i} B_{ij} J_{ij}^{\rm eff} + \sum_{j \neq i} C_{ij} + C_{ik} \right] \\ - \sum_{j>i} b_j B_{ij} \left(k_{ij}(1 - \Lambda_{ij}^*) + J_{ij}^{\rm eff} \right) e^{-\frac{h\nu_{ij}}{kT}} - \sum_{j<i} b_j \frac{g_j B_{ji}}{g_i} J_{ji}^{\rm eff} e^{\frac{h\nu_{ij}}{kT}} \\ - \sum_{j \neq i} b_j C_{ij} - R_{ki} - C_{ki} = 0 \end{aligned} \tag{2.15}$$

Upon convergence, $S_{ij} = S_{ij}^{\dagger}$ and $\bar{J}_{ij} = \Lambda_{ij}^* S_{ij}^{\dagger} + \bar{J}_{ij}^{\dagger} - \Lambda_{ij}^* S_{ij}^{\dagger} = \bar{J}_{ij}^{\dagger}$, so

$$J_{ij}^{\rm eff} = \bar{J}_{ij} - \Lambda_{ij}^* S_{ij} \tag{2.16}$$

It could be shown that, by replacing $J_{ij}^{\rm eff}$ by $\bar{J}_{ij} - \Lambda_{ij}^* S_{ij}$ in the Eq. (2.15), all terms with a factor Λ^* cancel. This shows that, upon convergence, Equations (2.15) and (2.7) are equivalent.

2.4 Solution of statistical equilibrium equations

Now, after presenting full details of the terms that enter preconditioned equations of statistical equilibrium in Eq. (2.15), we are in a position to solve these equations.

The system of linear equations that describe the state of the model atom has the form:

$$M_{ij} \times b_i = V_i \tag{2.17}$$

The diagonal terms of the matrix, M_{ii}, are multiplied by b_i, the departure coefficient of the level i, for which the equation is solved. From Eq. (2.15), it can be seen that b_i multiplies the terms that account for depopulation of the level i. Diagonal terms of M_{ij}, become:

$$\begin{aligned} M_{ii} = R_{ik} + \sum_{j<i} \frac{g_j B_{ji}}{g_i} [\frac{2h\nu_{ij}^3}{c^2}(1 - \Lambda^*) + \bar{J}_{ij}] + \\ \sum_{j>i} B_{ij}\bar{J}_{ij} + \sum_{j \neq i} C_{ij} + C_{ik} \end{aligned} \tag{2.18}$$

Eq. (2.15) also tells us that off-diagonal elements of M_{ij}, that are multiplied by b_j, account for the population of the level i. When j < i upward processes populate level i, so these terms become

$$M_{ij} = -\sum_{j<i} b_j \frac{g_j B_{ji}}{g_i} \bar{J}_{ij} e^{\frac{h\nu_{ij}}{kT}} - \sum_{j<i} b_j C_{ij} \tag{2.19}$$

When j > i, off-diagonal terms are defined by the downward transitions:

$$M_{ij} = -\sum_{j>i} b_j B_{ij} [\frac{2h\nu_{ij}^3}{c^2}(1 - \Lambda^*) + \bar{J}_{ij}] e^{-\frac{h\nu_{ij}}{kT}} - \sum_{j<i} b_j C_{ij} \tag{2.20}$$

Finally, the right hand side of the Eq. (2.17) is defined by the continuum recombination processes:

$$V_i = R_{ki} + C_{ki} \tag{2.21}$$

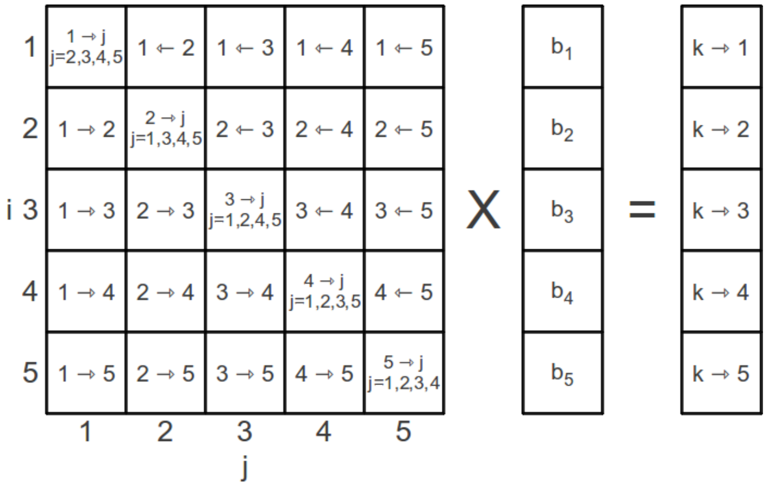

Fig. 2.1. Scheme showing the system of statistical equilibrium equation for a model atom that has 5 levels. Diagonal elements of the matrix (M_{ii}) account for depopulation, while off-diagonal terms account for the population of the level i. Right hand side of this system account for the continuum recombination ($k \rightarrow i$) processes.

Fig. 2.1 shows the system of statistical equilibrium equations for a model atom that has n = 5 levels. Such system of equations can be solved by adopting standard techniques of linear algebra.

2.5 An outline of the `NLTE3D` code

Computations with the `NLTE3D` code proceed along the following route:

- Model atmosphere is loaded. Various thermodynamical quantities (temperature, pressure, electron density etc.) are computed from the tabulated equation of state of the chosen chemical composition.

- $\bar{J}_{ij}$ values are computed for the continuum photo-ionization processes by utilizing Kurucz ODF (Castelli & Kurucz 2004) for line opacities and IONOPA continuum opacities.

- Wavelength-averaged photoionization cross sections are loaded and photoionization and photorecombination transition probabilities (R_{ik}, R_{ki} respectively) are computed for each level of the model atom. These transition probabilities are not changing with iterations hence they do not have to be recomputed at each cycle.

- Atomic data (level energies, collisional rate coefficients, Einstein coefficients, etc) is loaded. Tables of monochromatic IONOPA continuum opacities are computed at the line wavelengths in the $\log P - \log T$ plane. These tables are later interpolated to the values of the thermodynamic variables attained on the grid points of model atmosphere.

- Continuum intensities at all line wavelengths are computed. In case when the spectral line is weak and is not expected to strengthen with iterations, these intensities enter the rate equations. Otherwise, mean intensities and level populations are coupled and solution has to be reached by iteration.
- LTE line opacities, synthetic spectra and equivalent widths are computed.
- Collisional transition probabilities are computed. As with bound-free radiative transition probabilities, they are not changing with iteration, so they need to be computed only once.
- First set of departure coefficients is computed on a 3D model grid with either line opacity in LTE or with continuum opacity only. It is also possible to use previously computed set of departure coefficients for the first iteration. In this iteration, Λ^* is set to 0.0.
- The solution is iterated using ALI until all equivalent widths converge:
  – mean intensity and Λ^* are evaluated for the strong lines that require iterative solution. Line opacity and source function are computed by using NLTE atomic populations from the previous iteration.
  – new iterate of departure coefficients and ionization departure (b_{ion}) is computed using updated mean line intensities and Λ^*.
- After convergence, departure coefficients and, if requested, rates of all processes are saved to the output file.

2.6 Performance of ALI scheme

In this Section we provide tests regarding the performance of ALI scheme. For this experiment, we have performed 1D NLTE calculations with the `NLTE3D` code and oxygen model atom described in Sect. 3.4. For the solar metallicity models, oxygen abundance was set to A(O) = 8.76 and for [M/H] = −2.0 model atmospheres A(O) was set to 7.06 ([O/Fe] = 0.4), a typical value for the Galactic halo stars (Stasińska et al. 2012).

Table 2.1. Atmospheric parameters of a grid of 1D hydrostatic `LHD` model atmospheres and the number of iterations required for the convergence of NLTE solution using oxygen model atom and different iteration schemes.

Model atmosphere		Number of iterations		
$T_{\rm eff}$, K	$\log g$	OLI	ALI$_{\rm vert}$	ALI
[M/H] = 0.0, A(O) = 8.76				
6490	4.0	1609	291	114
5480	4.0	836	39	17
5970	2.5	8224	67	114
4480	2.5	5531	53	118
[M/H] = −2.0, A(O) = 7.06				
6530	4.0	16622	790	427
5470	4.0	14429	623	324
5020	2.5	6703	1190	624
4480	2.5	22364	309	196

We performed the `NLTE3D` calculations for three iteration schemes: ordinary Λ-iteration (OLI), ALI, where the Λ^* is computed for the vertical radiation ray only (denoted, ALI$_{\rm vert}$) and ALI where the angle-averaged Λ^* is utilized (denoted, ALI). The set-up for each particular case was iterated until the relative changes in the flux equivalent width, W, of all spectral lines considered fell below 10^{-5}.

Table 2.1 shows the number of iterations required by each iteration scheme for each model atmosphere in order to converge below 10^{-5} level. It could be seen that both ALI$_{\rm vert}$ and ALI schemes significantly outperform OLI and the differences in the number of iterations can reach two orders of magnitude.

Fig. 2.2 shows the largest relative changes in W as a function of iteration number for model atmospheres with [M/H] = 0 and [M/H] = −2.0. The figure clearly show the well-known behaviour of OLI that the changes in W stay nearly constant during a large number of iterations. On the other hand, the figures show that, depending on the utilized model atmosphere, ALI-based schemes sometimes become relatively noisy when the convergence limit is reached below $\Delta W/W \approx 10^{-4}$. It is also seen that in case of model atmospheres at [M/H] = −2.0 the convergence is slower. This may be caused by the fact that continuum opacity is much lower in these models, which, in turn, lowers the unity monochromatic optical depth at the wavelengths of strong UV lines. Since in the atmospheres of low-metallicity stars the formation of strong UV lines extends over wide interval of optical depths, more iterations are needed to transport them through the line formation region than in models of higher metallicity.

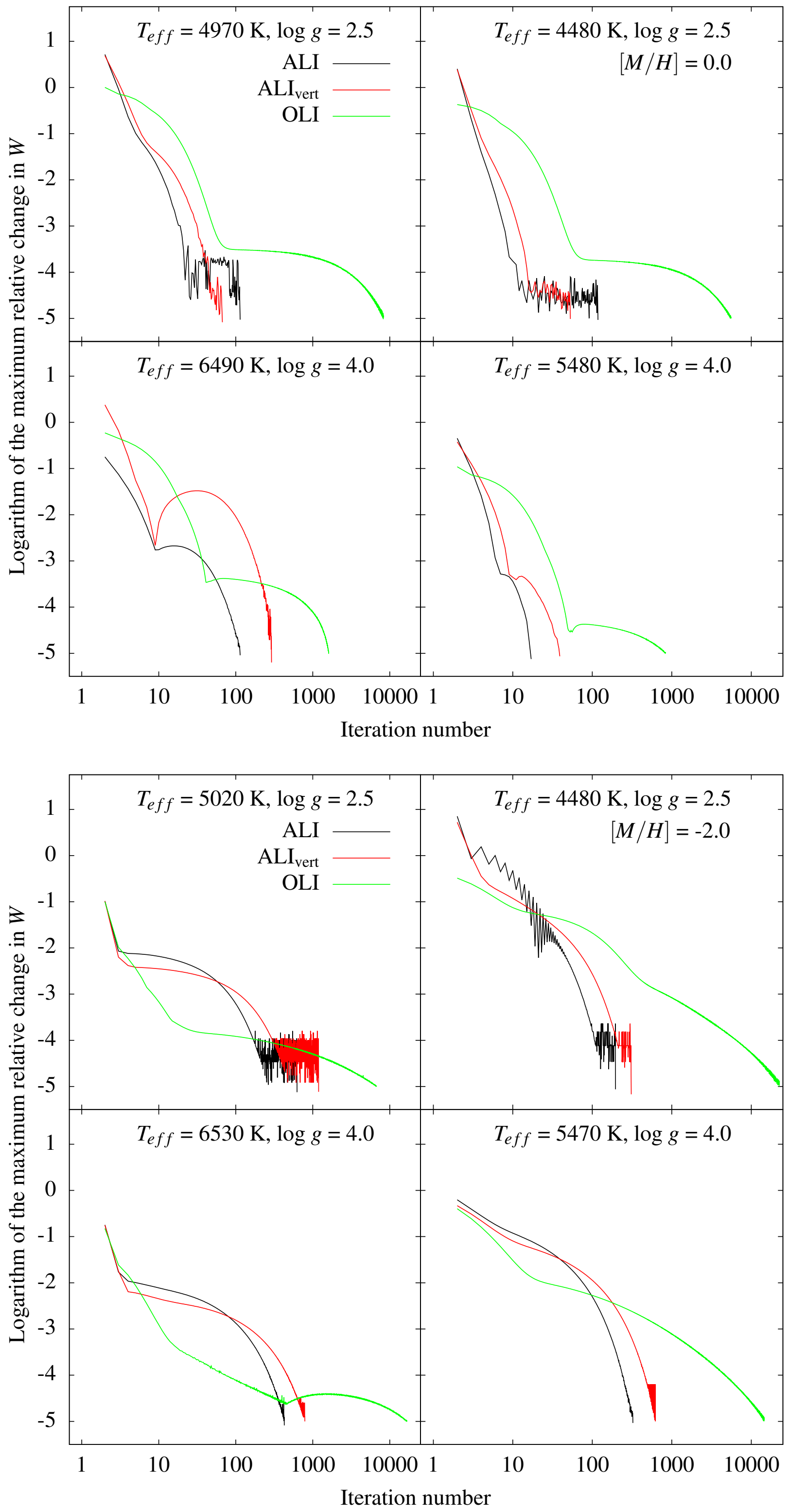

Fig. 2.2. Convergence of NLTE solution obtained using 1D hydrostatic `LHD` model atmospheres and three different iteration schemes. Top figure shows results for solar metallicity model atmospheres and the bottom plot shows results for model the atmospheres with [M/H] = −2.0. Results obtained using model atmospheres with log g = 2.5 and 4.0 are shown in top and bottom panels, respectively, while left and right panels show results obtained using models characterized with correspondingly higher and lower effective temperatures.

Chapter 3

Spectral lines of atomic oxygen in stellar atmospheres: O I IR triplet lines and solar oxygen abundance

3.1 Introduction

As it was discussed before, oxygen is a widely used tracer of the evolution of various stellar populations. It is mainly produced in massive stars that end their evolution as Type II supernovae. Knowledge about the oxygen abundance in different stellar populations was used to study Galactic star formation rates and constrain the models of Galactic chemical evolution (e.g., Matteucci & Francois 1992; Gratton et al. 2000). In all such studies, solar oxygen abundance[1], A(O), is used as a natural reference zero point.

Since oxygen is a volatile element, its compounds condense only partly in meteoritic matter, so that the relative amount of oxygen present in meteorites (i.e., with respect to some reference element, for example, silicon) is not representative of the oxygen abundance that was actually present in the original solar nebula. It is nevertheless thought that the original oxygen abundance is preserved in the solar photosphere this abundance can be determined by spectroscopic analysis. Recent state-of-the-art study of solar oxygen abundance performed using 3D NLTE abundance analysis techniques has yielded A(O) = 8.66 − 8.68 dex (Pereira et al. 2009b). Similar value of solar oxygen abundance, A(O) = 8.66 ± 0.05 dex, was obtained earlier by Asplund et al. (2004), who analyzed atomic and molecular oxygen lines in disk-integrated spectra. The work of Allende Prieto et al. (2001), who analyzed the forbidden oxygen line at 630 nm, resulted in A(O) = 8.69 ± 0.05 dex, while the investigation of Allende Prieto et al. (2004), who performed 3D NLTE analysis of center-to-limb variation of the O I IR triplet lines , suggested a slightly higher value of A(O) = 8.72 dex. Nevertheless, all these "new" values are significantly lower than the "canonical" solar oxygen abundance A(O) = 8.83 ± 0.06 dex determined

---

[1] $A(O) = \log[N(O)/N(H)] + 12$

by Grevesse & Sauval (1998) using classical 1D hydrostatic model atmospheres.

The rather low value of the solar oxygen abundance, A(O) $<$ 8.70 dex, as found in the investigations mentioned above, poses significant problem for theoretical solar structure models to meet the helioseismic constraints. These models depend on the solar chemical composition via radiative opacities, equation of state, and energy production rates. Changes in CNO abundances influence, for example, the structure of the radiative interior, location of the base of convective envelope, helium abundance in the convection zone, and the sound speed profile. It was shown by Basu & Antia (2008) that the "old" solar chemical composition of Grevesse & Sauval (1998) yields a much better agreement between theoretical predictions of helioseismology and helioseismic observations, while the use of "new" solar oxygen abundance leads to significant discrepancies.

According to the previous studies of the `CO`^{5}`BOLD` group (Caffau et al. 2008), solar oxygen abundance obtained using 3D LTE/1D NLTE techniques is somewhat higher, A(O) = 8.76 ± 0.07 dex. This rather high oxygen abundance was supported by the work of Ayres et al. (2013), who used a `CO`^{5}`BOLD` model atmosphere to analyze molecular CO lines (assuming n(C)/n(O)=0.5) and derived A(O) = 8.78 ± 0.02 dex. Villante et al. (2014) has shown that the solar chemical composition presented by Caffau et al. (2011), which includes a ‘high’ A(O), is in much better agreement with the overall metal composition inferred from helioseismology and solar neutrino data.

Spectroscopic abundance analysis relies on stellar atmosphere models and spectral synthesis computations. On the observational side, availability of high signal-to-noise spectra and high dispersion spectra is essential, as is the availability of clean (i.e., not blended) spectral lines. The number of suitable oxygen lines in the optical solar spectrum is very limited. The O I IR triplet lines at 777 nm are essentially free from any contamination and hence could be expected to be a good abundance indicators. It is well known, however, that the triplet lines are prone to departures from local thermodynamic equilibrium (LTE) in solar-type stars (e.g., Kiselman 1991). The NLTE effects lead to stronger synthetic spectral lines than in LTE and hence a lower oxygen abundance is required to match the observed line strength if the abundance analysis is performed using NLTE techniques.

It has been repeatedly demonstrated that it is impossible to reproduce the center-to-limb variation of the triplet lines under the assumption of LTE (Kiselman 1993; Pereira et al. 2009b). Pereira et al. (2009b) have also shown that NLTE synthetic line profiles computed using standard 1D hydrostatic model atmospheres (e.g., `ATLAS9`, `MARCS`) can not satisfactorily reproduce those observed in the solar spectrum. Somewhat better agreement is obtained if theoretical line profiles are computed using semi-empirical Holweger-Müller model (Holweger 1967; Holweger & Mueller 1974) model. Application of 3D hydrodynamical model atmospheres, however, gives the best results (Pereira et al. 2009b).

In this Chapter, we expanded on the work done by Caffau et al. (2008), following up on the investigation of the solar O I IR triplet at 777 nm with an independent 3D NLTE analysis of several high-quality solar intensity spectra for observed at different limb angles μ[2] (hereafter μ-angle for short) and of a disk-integrated flux spectrum. In Section 3.2, we describe the spectra that were used in for our analysis and in Sections 3.3–3.4.3 describe the model atmospheres and spectral synthesis tools used in our work. The main results are presented in Sections 3.5 and 3.6, where we describe the adopted methodology, perform different comparisons between observed and theoretical spectra, and determine solar oxygen abundance. We discuss obtained results and their implications in Sect. 3.7.

3.2 Observational data

We utilize intensity spectra of the O I IR triplet recorded at different μ-angles across the solar disk. As mentioned above, the analysis of the triplet lines requires detailed modelling of departures from LTE. Since the relevant collisional cross sections are essentially unknown, we derive both the oxygen abundance, A(O), and the scaling factor with respect to the classical (Drawin) cross sections for collisional excitation and ionization of oxygen atoms by neutral hydrogen, $S_{\rm H}$, from a simultaneous fit of the line profiles or their equivalent widths at different μ-angles. An analysis of the disk-center or disk-integrated spectrum alone would be insufficient to yield unique results. Since the impact of $S_{\rm H}$ depends systematically on the depth of line formation and therefore on μ, the variation of the spectral lines with disk position adds another dimension to the analysis and helps to constrain the problem. Following a similar idea, Caffau et al. (2015) utilized the center-to-limb variation of the blend of oxygen and nickel lines at 630 nm to separate the contribution of the individual elements.

---

[2] $\mu = \cos\theta$, where θ is the angle between the line of sight and the direction perpendicular to the solar surface; $\mu = 1$ at disk center, while $\mu = 0$ at the limb.

We made use of the following three independent observational data sets:

1. The absolutely calibrated FTS spectra obtained at Kitt Peak in the 1980s, as described by Neckel & Labs (1984) and Neckel (1999), covering the wavelength range from 330 nm to 1250 nm for the disk center and full disk (Sun-as-a-star), respectively. In the following, we refer to this as "Neckel Intensity" and "Neckel Flux". The spectral resolution ($\Delta\lambda$) ranges from 0.4 pm at 330 nm to 2 pm at 1250 nm ($825\,000 > \lambda/\Delta\lambda > 625\,000$).

2. A set of spectra observed at Kitt Peak observatory with the McMath-Pierce Solar Telescope and rapid scan double-pass spectrometer (see Livingston et al. 2007, and references therein). Observations were taken in single-pass mode on 12 September, 2006; the local time was about 10h15m to 10h45m. The resolution was set by the slit width: 0.1 mm for the entrance and 0.2 mm for the exit slit. This yields a resolution of $\lambda/\Delta\lambda \approx 90\,000$. The slit has a length of 10 mm and was set parallel to the limb. Observations were made at six μ-angles: $\mu = 1.00, 0.87, 0.66, 0.48, 0.35,$ and 0.25, along the meridian N to S in telescope (geographic) coordinates. Two spectra for any μ value and four spectra at disk center were used. The exposure time for each individual spectrum was 100 s, thus essentially freezing the five-minute solar oscillations. No wavelength calibration source was observed, and we used the available telluric lines to perform the wavelength calibration. The positions of the telluric lines were measured on the Neckel Intensity spectrum and a linear dispersion relation was assumed.

   After the wavelength calibration, we summed the spectra at equal μ to improve the signal-to-noise ratio (S/N). The continuum of the summed spectra was defined by a cubic spline passing through a predefined set of line-free spectral windows. A comparison of the normalized disk-center spectrum with the Neckel Intensity atlas reveals a systematic difference in the equivalent widths, in the sense that the spectral lines are weaker in this spectrum by about 4%. We attribute this difference to instrumental stray light, and correct the normalized spectra for all μ-angles as $I_{\mathrm{corr}}(\lambda) = (1 + f)\, I(\lambda) - f$, where $f = 0.0405$ is the stray light fraction. We estimate the signal-to-noise ratio of the stray light corrected spectra to be S/N $\approx$ 1500 at disk center, and S/N $\approx$ 700 at $\mu = 0.25$. In the following, we refer to these spectra as WCLC.

3. The high-quality spatially and temporally averaged intensity spectra used by Pereira et al. (2009b)[3], recorded with the Swedish 1-m Solar Telescope (Scharmer et al. 2003) on Roque de Los Muchachos observatory at La Palma over two weeks in May 2007. For these observations, the TRIPPEL spectrograph was used with a slit width set to 25 μm, corresponding to $0.11''$ on the sky. The spectral resolution of this data set is $\lambda/\Delta\lambda \approx 200\,000$. The data set consists of spectra at five disk positions, $\mu = 1.00$, 0.816, 0.608, 0.424, and 0.197. Since a large number of spectra at different instances of time and space were summed up, a high signal-to-noise ratio of S/N $\approx 1\,200 - 1\,500$ was achieved at all μ-angles. The spectra are corrected for stray light. See Pereira et al. (2009a,b) for a detailed discussion regarding this observational data set.

3.3 Model atmospheres

In this work we utilize Solar model atmospheres computed with the CO^{5}BOLD and LHD codes (see Chapter 1.1). This model atmosphere was computed on a Cartesian grid consisting of 140 grid points horizontally and 150 grid points vertically and spanning 5.56 Mm horizontally and 2.25 Mm vertically. 12 opacity bins were used for the computation of radiation transport. This set-up was running for 1.2 hours of the stellar time that was adequate to cover 14 convective overturns and sufficiently sample the evolution of the Solar surface. The simulation resulted in mean $T_{\rm eff} \approx 5774 \pm 16$ K. For the additional information about the Solar model used in this Thesis and comparison with the other 3D-hydrodynamical Solar model atmospheres see Beeck et al. (2012).

In order to perform differential analysis, 1D LHD model that possesses identical microphysics, was also computed. Since oxygen triplet lines have high excitation potentials and, hence, form deeply in the atmosphere, it is likely that they are sensitive to the choice of mixing length parameter, $\alpha_{\rm MLT}$. In order to probe the possible influence of $\alpha_{\rm MLT}$, we have computed a grid of LHD model atmospheres that has $\alpha_{\rm MLT} = 0.5, 1.0, 1.5$. After performing some tests, however, we found negligible influence of $\alpha_{\rm MLT}$ on the triplet lines. Hence, all results shown in the following are based in the LHD model atmosphere with $\alpha_{\rm MLT} = 1.0$.

We have also used the semi-empirical model atmosphere derived by Holweger & Mueller (1974) (in the following HM model, see also Holweger

---

[3] `http://cdsarc.u-strasbg.fr/viz-bin/qcat?J/A+A/508/1403`

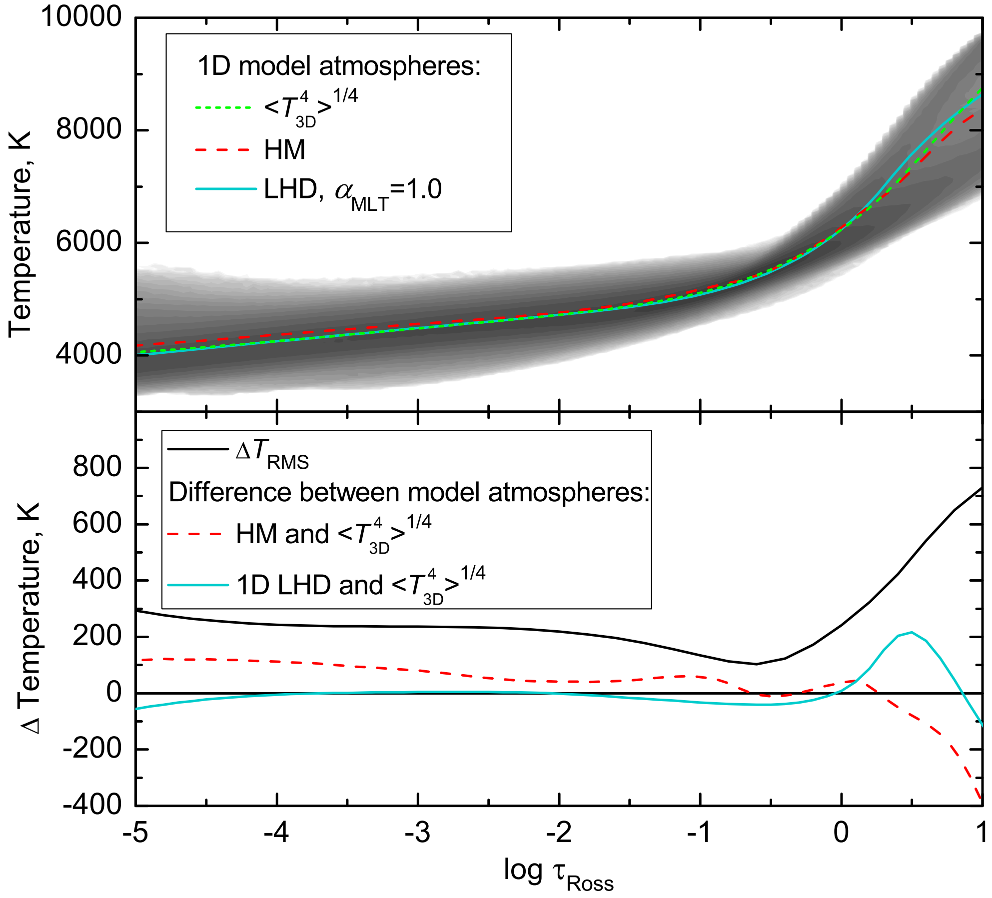

Fig. 3.1. Top: temperature structure of 3D hydrodynamical CO^{5}BOLD, average ⟨3D⟩, 1D hydrostatic LHD, and HM model atmosphere on the Rosseland optical depth scale. Bottom: horizontal temperature fluctuations, ΔT_{RMS}, of the 3D model at constant τ_{Ross} (black) and temperature difference HM – ⟨3D⟩ (dashed) and 1D LHD– ⟨3D⟩ (blue) as a function of $\log \tau_{\mathrm{Ross}}$.

1967). The $T(\tau)$ relation of this model was empirically fine-tuned to match observations of the solar continuum radiation and a variety of spectral lines.

The temperature structure of the HM model is significantly different from that of the 1D LHD model atmosphere, as illustrated in Fig. 3.1. In the optical depth range $-5.0 < \log \tau_{\mathrm{Ros}} < -0.5$, the HM model is slightly warmer than the ⟨3D⟩ model by 50 to 100 K, while the 1D LHD model almost perfectly matches the ⟨3D⟩ model. In the deep photosphere ($-0.5 < \log \tau_{\mathrm{Ros}} < +0.5$), where significant parts of the triplet lines originate, the HM model closely follows the temperature of the ⟨3D⟩ model, while the 1D LHD shows a somewhat steeper temperature gradient in these layers. This results in stronger O I triplet lines computed from the LHD model compared to those of the HM atmosphere.

Since the NLTE3D code can only work with model atmospheres defined on 3D geometrical grid, the 1D LHD and HM model atmospheres were converted to pseudo-3D models by replicating the particular 1D model atmosphere three times horizontally in each direction so that the resulting model would have 3x3 identical columns. Using the same equation of state and Rosseland opacity tables as in the 3D models, the vertical grid spacing of the pseudo-3D models is adjusted to ensure that the resulting model atmosphere is sampled at equidistant $\log \tau_{\rm Ross}$ levels, and preserves the $T(\tau)$ relation of the original 1D model.

3.4 3D/1D NLTE spectral synthesis computations

3D NLTE spectral synthesis was done in two separate steps. Firstly, the departure coefficients of the atomic levels involved in the O I triplet transition were computed with the `NLTE3D` code (see Sect. 2.1). Then the departure coefficients were passed to the spectral line synthesis package `Linfor3D` (see Sect. 1.2.2) that was used to compute NLTE line opacity and source function, solve the equation of radiation transport and compute line profiles at various disk positions. In this Section we describe the NLTE spectrum synthesis calculations.

3.4.1 Model atom of oxygen

We used a new model atom that was constructed specifically for this investigation. We chose to do this (instead, e.g., adopting a previously published model atom) because we wanted to have freedom to test and modify it according to our own needs. We have converged to an oxygen model atom that consists of 22 levels of O I (plus continuum), each having an associated bound-free transition. In addition, we take 64 bound-bound transitions into account, some of which are purely collisional. Fig. 3.2 shows the Grotrian diagram of our model atom.

Level energies and statistical weights of the model atom were taken from the NIST Atomic Spectra Database Version 5[4]. Cross sections for radiative, bound-free transitions were taken from the TOPBASE service[5] of the Opacity Project (Cunto et al. 1993). Lacking reliable collisional cross sections derived from laboratory measurements or quantum-mechanical calculations, we resort to the classical prescriptions of Allen (Allen 1973, p. 41) and Drawin (Drawin 1969; Steenbock & Holweger 1984; Lambert 1993) to obtain the rate coefficients for bound-free transitions due to ionizing collisions with electrons and neutral hydrogen, respectively. As the Drawin approximation is highly uncertain (see Sect. 3.7.3 below), we scale the rates obtained from the Drawin formula by the adjustable parameter $S_{\rm H}$, which is deduced simultaneously with

---

[4] `http://www.nist.gov/pml/data/asd.cfm/`

[5] `http://cdsweb.u-strasbg.fr/topbase/topbase.html`

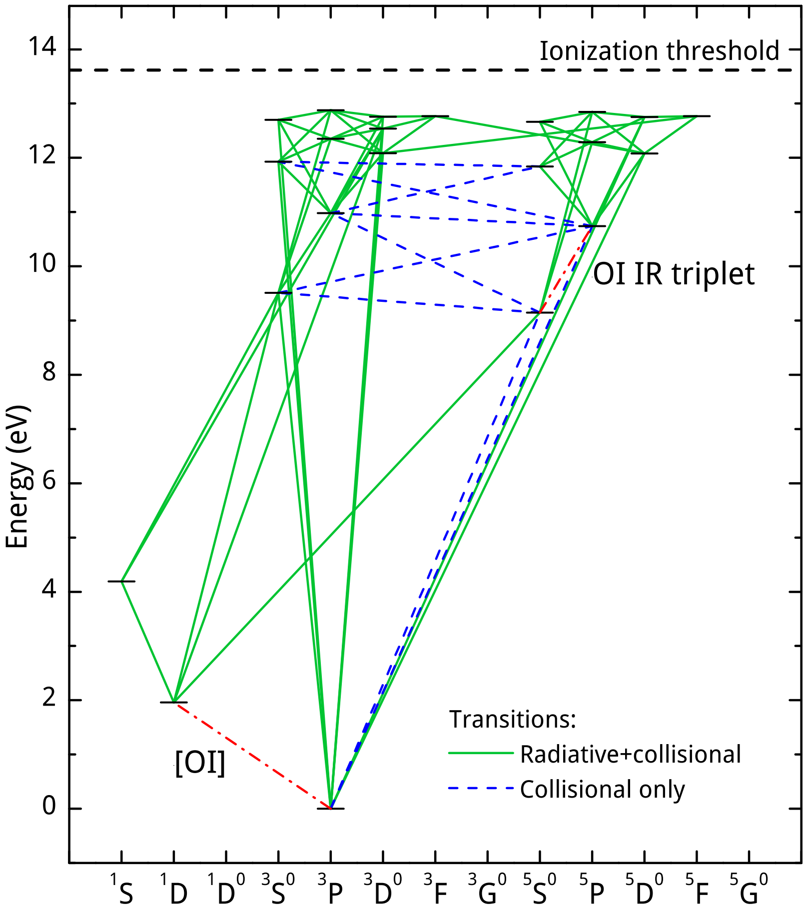

Fig. 3.2. Oxygen model atom used in this work. Radiatively allowed transitions are marked with green solid lines. Radiatively forbidden transitions, which were treated via electron-impact excitation only, are marked by blue dashed lines. The forbidden [O I] line and the O I IR triplet are marked by red dash-dotted lines. We took collisional and radiative bound-free transitions into account for each level.

the oxygen abundance (see Sect. 3.5). Finally, we include the charge transfer reaction $O^0 + H^+ \rightleftharpoons O^+ + H^0$ for the ground level of oxygen, as described by Arnaud & Rothenflug (1985). Because the ionization potentials of O I and H I are similar, this reaction is nearly resonant and very efficient. It ensures that the ground level of O I is in equilibrium with O I.

Out of the 64 bound-bound transitions, 54 are radiatively and collisionally permitted, while the remaining 10 are radiatively forbidden. For the latter transitions, we only take collisions with electrons into account (see below). Einstein coefficients and wavelengths for the permitted transitions were again taken from the NIST Atomic Spectra Database.

Rate coefficients for collisional excitation by neutral hydrogen were computed with classical Drawin formula and scaled by the same factor S_H as applied to the ionizing collisions by neutral hydrogen. Since the collisional cross section according to the Drawin formalism is proportional to the oscillator strength gf of the transition, the levels of the radiatively forbidden transitions are also not coupled by hydrogen collisional excitation in our model atom. Alternative assumptions and their impact on the derived oxygen abundance are briefly discussed in Sect. 3.7.3.

Rate coefficients for the collisional excitation by e^- were taken from the detailed R-matrix computations of Barklem (2007). For the radiatively allowed transitions that were not included in the latter work, we applied the classical van Regemorter's formula (van Regemorter 1962). The rate coefficients of Barklem (2007), unlike those computed by the oscillator strength-dependent classical van Regemorter's formula, are nonzero for radiatively forbidden transitions (blue dashed lines in Fig. 3.2), and hence we were able to account for the inter-system collisional transitions. The latter transitions are thought to play an important role in defining the statistical equilibrium of oxygen (especially at low metallicities, see Fabbian et al. 2009) and must be taken into account in realistic NLTE simulations. While the work of Barklem (2007) provides data for a total of 171 bound-bound transitions, we have only used 48 of them, based on the magnitude of their rate coefficient. We have performed tests that evaluate the influence of the remaining purely collisional transitions and found that it is negligible in the case of the Sun.

It should be noted that fine-structure splitting is ignored in our model atom, and all multiplets are treated as singlets. In particular, the upper level of the O I IR triplet, level $3p^5P$, is treated as a single superlevel with a single departure coefficient. However, since the three triplet components are well separated in wavelength, the line opacity computed from the combined gf-value of the superlevel transition would be too large, resulting in a wrong mean radiation field and, in turn, in wrong radiative excitation rates. To avoid this problem, we replace – for the radiative line transfer calculations only – the summed-up gf-value of the combined multiplet transition with the gf-value of the intermediate triplet component, thus diminishing the line opacity by a factor 3 (for tests and their results see Steffen et al. 2015). Similar opacity scaling is applied for all other lines that involve multiplet transitions. This approach significantly reduces the computational cost of solving the statistical equilibrium equations.

3.4.2 Estimation of NLTE effects

The first step in the computation of 3D/1D NLTE line profiles of O I IR triplet is the computation of departure coefficients, b_i[6]. This is done by using the `NLTE3D` code, 3D/1D Solar model atmospheres and oxygen model atom described previously.

Computation of the departure coefficients follows the scheme explained in Sect. 2.1. Important details in the computation of the departure coefficients is that, in order to save computation time, 3D model box was reduced and only each third point in both horizontal directions was used. This helped us to save nearly 90% of the computation time and our tests have shown that this does not influence the final results in any significant way (for tests and their results see Steffen et al. 2015). Also, it should be mentioned that ALIs were continued until relative changes in flux Ws of all sufficiently strong lines converged below 10^{-3}. We checked that increasing the accuracy of the convergence criterion does not alter the resulting departure coefficients significantly, which might be ascribed to the good convergence properties of the ALI scheme.

In preparation for the following investigation, we computed departure coefficients for a grid of $S_{\rm H}$ and A(O) values. The $S_{\rm H}$ values range from 0 to 8/3 in steps of 1/3, and A(O) varies from 8.65 to 8.83 dex in steps of 0.03 dex. The spectrum synthesis calculations described in Sect. 3.4.3 are based on this rather extensive and dense grid of departure coefficients. Using this rather extensive and dense grid of departure coefficients we performed spectrum synthesis calculations that are described in the next Section.

3.4.3 Spectral synthesis calculations

The second step in computing the synthetic line profiles of the oxygen IR triplet is the spectrum synthesis itself. Here we adopt the same atomic line parameters as specified in Table 1 of Caffau et al. (2008), and perform detailed 3D NLTE line formation calculations with the `Linfor3D`[7] package, which can handle both 3D and 1D model atmospheres. As in the case of the `NLTE3D` calculations of the departure coefficients, we reduced the horizontal resolution of the 3D model atmosphere by choosing only every third grid point in x and y-direction. Again, we conducted experiments confirming that this reduction does not influence the

---

[6] departure coefficient b_i is defined as a ratio of NLTE-to-LTE level populations for the level i

[7] `http://www.aip.de/Members/msteffen/linfor3d`

final results (for tests and their results see Steffen et al. 2015).

NLTE line opacity and source function were calculated by using LTE population numbers from IONOPA package and previously computed departure coefficients (see Sect. 1.2.2 and equations 1.6, 1.7). Using these quantities and the continuum opacity from the IONOPA package, the radiative transfer equation is integrated on long characteristics to obtain the emergent radiative intensities as a function of wavelength. The intensity spectra are calculated for two sets of inclination angles μ, which represent the WCLC and Pereira et al. (2009b) observations (see Sect. 3.2 or Table 3.2), in each case for four azimuthal directions (0, $\pi/2$, π, $3/2\,\pi$). The final intensity spectrum for each μ is obtained by averaging over all surface elements, and to improve the statistics, over all azimuthal directions. For comparison with the solar flux spectrum, we computed the integral over μ of the μ-weighted intensity spectra using cubic splines to derive the disk-integrated flux profile.

We finally compute a grid of synthetic line profiles using the corresponding grid of departure coefficients described in the previous Section. Each component of the oxygen triplet is synthesized for S_{H}-values in the range from 0 to 8/3 (with steps of 1/3), and A(O)-values in the range between 8.65 and 8.83 (with steps of 0.03 dex).

3.5 Line profile fitting and results

Computed synthetic intensity spectra are compared with observations across the solar disk to derive A(O) and S_{H} simultaneously. In this Section we compare observed and theoretical intensity line profiles and search for the best-fitting A(O)–S_{H} combination. This task utilizes the grid of theoretical NLTE line profiles described in Sect. 3.4.3) and searches for the A(O)–S_{H} combination that provides the best fit of the intensity profiles of a single triplet component simultaneously at all μ-angles.

3.5.1 Fitting procedure

We employ the Levenberg-Markwardt least-squares fitting algorithm (Markwardt 2009), as implemented in IDL procedure MPFIT, to find the minimum χ^2 in the four-dimensional parameter space defined by A(O), S_{H}, v_{b}, and $\Delta\lambda$. Here v_{b} is the FWHM (in velocity space) of a Gaussian kernel, which is used to apply some extra line broadening to the synthetic spectra to account for instrumental broadening and, in the case of 1D model atmospheres, macroturbulence; $\Delta\lambda$ is a global wavelength shift applied to the synthetic spectrum to compensate for potential imperfections of the wavelength calibration, uncertainties in the laboratory wavelengths, and systematic component- and μ-dependent line shifts. Test runs with an additional free fitting parameter for the continuum placement resulted in unsatisfactory fits. We therefore rely on the correct normalization of the observed spectra and consider the continuum level as fixed.

In a first sweep, we find the minimum χ^2 for each triplet component k and each μ-angle individually. Here χ^2 is defined as

$$\chi^2 = \sum_{i=1}^{n} \frac{\left(I_i^{\mathrm{obs}} - I_i^{\mathrm{calc}}\right)^2}{\sigma_i^2}, \tag{3.1}$$

where the sum is taken over all n considered wavelength points of the line profile, I_i^{obs} and I_i^{calc} is the intensity of observed and synthetic normalized spectrum, respectively, and σ_i is the pixel-dependent observational uncertainty of the spectrum to be fitted. For simplicity, we have adopted a fixed continuum signal-to-noise ratio of $S/N = 500$ for both the WCLC and the Pereira spectra, and computed σ_i simply as $\sigma = (S/N)^{-1}$, independent of wavelength point i and inclination angle μ.

An obvious blend in the blue wing of the strongest triplet component at $\lambda\,777.2$ nm is excluded from the relevant wavelength range by masking a window between -374 and -214 mÅ from the line center, setting $1/\sigma_i = 0$ for these pixels.

The result of this χ^2 minimization procedure is a set of best-fit parameters A(O), S_{H}, v_{b}, $\Delta\lambda$ for each (k, μ). These intermediate results are only used for two purposes: (i) for fixing the relative wavelength shift of the line profiles as a function of μ for each triplet component k; and (ii) to 'measure' the equivalent width of each individual observed line profile via numerical integration of the best-fitting synthetic line profile over a fixed wavelength interval of ±2 Å. The measured equivalent widths are used later for the equivalent width fitting method as described in Sect. 3.6.1.

We note that the oxygen abundance obtained from fitting the individual line profiles is relatively high, $8.78 < \mathrm{A(O)} < 8.87$, where the required oxygen abundance tends to increase towards the limb. At the same time, the corresponding S_{H}-values are large, too ($S_{\mathrm{H}} > 3.0$). However, we do not consider these results to be relevant because the line profile at a given single μ can be reproduced almost equally well with different combinations of the fitting parameters A(O), S_H, and v_b, which are tightly correlated. Small imperfections in the theoretical and / or observed line profiles can thus easily lead to ill-defined solutions. This degeneracy is only lifted when fitting the profiles at all μ-angles simultaneously.

In the second sweep, we fit the line profiles at all μ-angles (μ_j, $j = 1 \ldots m$) simultaneously, but separately for each of the three triplet components. In this case, χ^2 is defined as

$$\chi^2 = \sum_{j=1}^{m} \sum_{i=1}^{n} \frac{\left(I_{i,j}^{\mathrm{obs}} - I_{i,j}^{\mathrm{calc}}\right)^2}{\sigma_{i,j}^2}, \tag{3.2}$$

where m is the number of considered μ-angles. Again, $\sigma_{i,j}$ is taken to be constant, $\sigma_{i,j} = \sigma = (S/N)^{-1}$, as explained above, and the blend in the blue wing of the strongest triplet line at $\lambda\,777.2\,$nn is masked as before. Treating the triplet components separately has the advantage of allowing a consistency check and providing an independent error estimate of the derived oxygen abundance.

As in the first sweep, we consider A(O), S_H, and v_b as free fitting parameters, but instead of a single global $\Delta\lambda$, we introduce two global line shift parameters, $\Delta\lambda_1$ and $\Delta\lambda_2$, to allow for the most general case of a μ-dependent line shift correction, computed as $\Delta\lambda(\mu) = \Delta\lambda_0(\mu) + \Delta\lambda_1 + \Delta\lambda_2\,(1 - \mu)$, where $\Delta\lambda_0(\mu)$ is the individual wavelength shift determined in the first sweep for the respective μ-angle. It turns out, however, that the results of the global fitting are insensitive to the detailed treatment of the line shifts.

3.5.2 Fitting results for the WCLC and Pereira spectra

Fig. 3.3 shows the results of the simultaneous line profile fitting with the 3D NLTE synthetic line profiles of the WCLC and Pereira spectrum, respectively. In general, the agreement between observation and model prediction is very good; the differences never exceed 1% of the continuum intensity and usually remain at a much lower level. Both the line wings and line core are represented very well at all inclination angles. The very satisfactory match we obtain between theory and observation suggests that both the velocity field and the thermal structure of our model atmosphere are realistic in the range of optical depths sampled by the O I IR triplet lines for the considered inclination angles. In addition, the accurate reproduction of the observed line profiles suggests that our NLTE line formation technique is adequate, despite the possible shortcomings

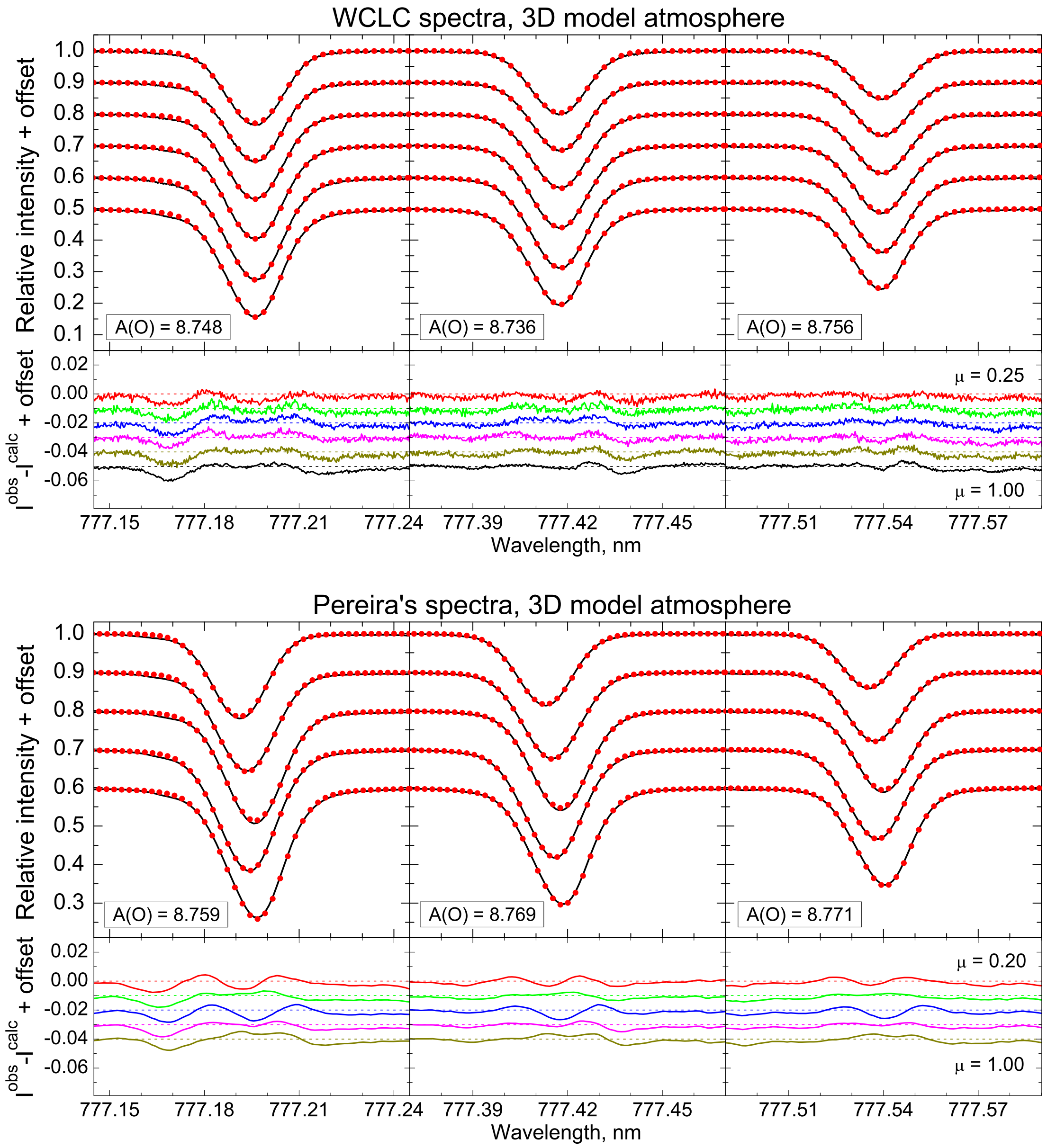

Fig. 3.3. Best-fitting NLTE line profiles computed with the 3D model atmosphere for the WCLC (top) and Pereira (bottom) spectra. The top panels show the observed spectrum (black lines) and their theoretical best-fitting counterparts (red dots) for the different μ-angles, μ increasing from top (limb) to bottom (disk center). For clarity, a vertical offset of 0.1 was applied between consecutive μ-angles. The legend shows the best-fitting A(O) value for each of the three triplet lines. The bottom panels show the difference of the normalized intensites $I^{\mathrm{obs}} - I^{\mathrm{calc}}$. An offset of 0.01 was applied between the different μ-angles (μ increasing downwards).

regarding the modeling of hydrogen collisions.

The line profiles computed with the 1D hydrostatic model atmospheres result in a less satisfactory agreement with the observations. For example, given a single A(O) and S_{H} value, the ⟨3D⟩ and 1D `LHD` models fail to simultaneously account for the line core and wings at $\mu = 1$, and predict a much too weak

Table 3.1. Results of NLTE line profile fitting with various model atmospheres: A(O) and $S_{\rm H}$-values for two different observed spectra (WCLC and Pereira). For the individual triplet components, we give the profile fitting errors of A(O) and $S_{\rm H}$ (only if $S_{\rm H} > 0$), while the errors of the mean values correspond to the standard deviation of the individual lines

	A(O)		$S_{\rm H}$	
Data set:	WCLC	Pereira	WCLC	Pereira
λ, nm	3D model atmosphere			
777.2	8.748 ± 0.002	8.759 ± 0.004	1.44 ± 0.03	1.64 ± 0.07
777.4	8.735 ± 0.002	8.769 ± 0.004	1.22 ± 0.03	1.67 ± 0.07
777.5	8.756 ± 0.002	8.771 ± 0.003	1.58 ± 0.04	1.85 ± 0.07
Mean	8.747 ± 0.010	8.766 ± 0.006	1.41 ± 0.19	1.72 ± 0.12
λ, nm	$\langle$3D$\rangle$ model atmosphere, $\xi_{\rm mic}$ = 1.0 km/s			
777.2	8.591	8.641 ± 0.011	0.00	0.22 ± 0.05
777.4	8.603	8.609	0.00	0.00
777.5	8.614	8.623 ± 0.010	0.00	0.03 ± 0.05
Mean	8.603 ± 0.011	8.624 ± 0.016	–	0.08 ± 0.12
λ, nm	HM model atmosphere, $\xi_{\rm mic}$ = 0.8 km/s			
777.2	8.671 ± 0.004	8.673 ± 0.008	0.44 ± 0.03	0.46 ± 0.06
777.4	8.680 ± 0.004	8.713 ± 0.007	0.43 ± 0.03	0.66 ± 0.06
777.5	8.747 ± 0.002	8.759 ± 0.005	1.02 ± 0.03	1.18 ± 0.07
Mean	8.699 ± 0.041	8.715 ± 0.043	0.63 ± 0.34	0.76 ± 0.37
λ, nm	HM model atmosphere, $\xi_{\rm mic}$ = 1.2 km/s			
777.2	8.635 ± 0.005	8.638 ± 0.010	0.38 ± 0.03	0.40 ± 0.06
777.4	8.644 ± 0.005	8.671 ± 0.007	0.34 ± 0.03	0.49 ± 0.06
777.5	8.715 ± 0.002	8.727 ± 0.005	0.86 ± 0.03	1.00 ± 0.07
Mean	8.664 ± 0.044	8.679 ± 0.045	0.53 ± 0.29	0.63 ± 0.32
λ, nm	LHD model atmosphere, $\alpha_{\rm MLT}$ = 1.0, $\xi_{\rm mic}$ = 0.8 km/s			
777.2	8.608	8.607	0.0	0.0
777.4	8.616	8.620	0.0	0.0
777.5	8.623	8.625	0.0	0.0
Mean	8.616 ± 0.008	8.617 ± 0.010	–	–
λ, nm	LHD model atmosphere, $\alpha_{\rm MLT}$ = 1.0, $\xi_{\rm mic}$ = 1.2 km/s			
777.2	8.581	8.580	0.0	0.0
777.4	8.593	8.597	0.0	0.0
777.5	8.604	8.606	0.0	0.0
Mean	8.593 ± 0.011	8.594 ± 0.013	–	–

line core close to the limb. The situation with the HM model is better, but the line profile fits are still clearly inferior to those computed with the 3D model atmosphere. It is worth mentioning that, for all 1D model atmospheres, changing the (μ-independent) microturbulence parameter only changes the value of the best-fitting A(O) and $S_{\rm H}$, but does not improve the quality of the fits.

In Table 3.1, we summarize the main results derived from fitting the line profiles simultaneously for all μ-angles, separately for each of the three triplet components, and for both the WCLC and the Pereira observed spectra. Columns (2) and (3) list the best-fitting oxygen abundance A(O) and their profile fitting errors for WCLC and Pereira, respectively, and Col. (4) shows the difference between A(O) derived from the two different sets of spectra. Columns (5) and (6) give the corresponding results for S_H, while the last two columns show the reduced χ^2 of the best fit for the two sets of spectra, respectively, defined as $\chi^2_\mathrm{red} = \chi^2/(n \times m - p)$, where $p = 5$ is the number of free fitting parameters. The fact that χ^2_red is of the order of unity means that the fit provided by the synthetic spectra is good (at least for the 3D model), given the assumed uncertainty of the observed spectral intensity of $\sigma_i = 1/500$. However, only relative χ^2-values are considered meaningful for judging the quality of a fit.

The profile fitting errors of A(O) and S_H given in Table 3.1 are computed as the square root of the corresponding diagonal elements of the covariance matrix of the fitting parameters, which is provided by the MPFIT procedure. The fact that these fitting errors are relatively small shows that the solution found by the fitting procedure is well defined. However, these fitting errors do not account for possible systematic errors (e.g., due to imperfect continuum placement, unknown weak blends, insufficient time averaging, etc.), and hence the true errors are likely to be larger. In the case of the ⟨3D⟩ and `LHD` models, the fitting errors are meaningless because the best fit would require $S_\mathrm{H}<0$ (see below), and the constraint $S_\mathrm{H} \geq 0$ essentially enforces $S_\mathrm{H}=0$.

As shown in Table 3.1, the oxygen abundances derived from the two sets of observed spectra generally agree within 0.03 dex or better, which is of the same order of magnitude as the line-to-line variation of A(O). The WCLC spectra produce systematically lower abundances. We attribute this to the systematically stronger lines at low μ compared to the Pereira et al. (2009b) data (cf. Fig. 3.4 below), which implies a reduced gradient $W(\mu)$, and, in turn, a lower S_H and A(O), as explained in more detail in Sect. 3.7.2. In the case of the 3D model atmosphere, we consider the agreement in the derived A(O) between the different triplet lines and between the two sets of spectra as satisfactory.

In case of 1D `LHD` model atmospheres, the agreement between the best-fit parameters of the two spectra is nearly perfect, but this is again related to the fact that S_H is forced to 0. The resulting fits are not good ($\chi^2_\mathrm{red} > 5$), particularly at the lowest μ-angle, as mentioned above. The derived A(O) are significantly lower (by about −0.15 dex) than for the 3D case. Similar conclusions can be drawn for the ⟨3D⟩ model. The NLTE oxygen abundance obtained with the 1D semi-empirical HM model atmosphere lies somewhere in between the 3D and the 1D `LHD` results. While S_H is positive, the line profiles are poorly fitted, both at disk center and near the limb, and the line-to-line variation of A(O) is rather high.

As will be discussed below in Sect. 3.7.2, all 1D results are systematically biased towards low S_H and low A(O) values. In the following, we shall therefore ignore the 1D results for the determination of the solar oxygen abundance.

To estimate the solar oxygen abundance from the profile fitting method, we compute, separately for each of the two data sets, the average abundance, ⟨A(O)⟩, as the unweighted mean over the best-fitting A(O) values of the three triplet lines. These mean oxygen abundances are listed in Table 3.1 in the rows marked 'Mean', together with their errors, which in this case are defined by the standard deviation of the individual data points from the three triplet components.

From the 3D NLTE synthetic spectra we find: $\langle A(O) \rangle = 8.747 \pm 0.010$ dex (WCLC spectra) and $\langle A(O) \rangle = 8.766 \pm 0.006$ dex (Pereira's spectra). We note that the $1\,\sigma$ error bars of the two results fail (by a narrow margin) to overlap, indicative of unaccounted systematic errors. We finally derive a two-spectra average of $\langle\langle A(O) \rangle\rangle = 8.757 \pm 0.01$ dex ($\langle\langle S_H \rangle\rangle = 1.6 \pm 0.2$).

3.5.3 Fitting of disk-center intensity and flux line profiles

As an independent consistency check, we also applied our line profile fitting procedure to the Neckel & Labs (1984) FTS spectra. In this case, we simultaneously fit the solar disk-center (Neckel Intensity) and disk-integrated (Neckel Flux) O I IR triplet line profiles. The blue wing of the 777.2 nm line is masked as before. The synthetic flux spectrum is computed by integration over μ of the μ-weighted intensity spectra available at the five inclinations defined by the Pereira spectra. Subsequently, the flux spectrum is broadened with the solar synodic projected rotational velocity $v \sin i = 1.8$ km/s. The fitting parameters are again A(O), S_H, instrumental broadening v_b, and the individual line shifts $\Delta\lambda_1$ and $\Delta\lambda_2$ for intensity and flux profile, respectively.

Using the 3D NLTE synthetic line profiles, we obtain an average oxygen abundance of $A(O) = 8.80 \pm 0.008$, where this error refers to the fitting error; the line-to-line scatter is much smaller, < 0.001 dex. The best-fitting mean S_H value is 2.7 ± 0.25. As before, the quality of the fits is very satisfactory, with

$\chi^2_{\mathrm{red}} = 0.81$, 0.84, and 1.13 for the three triplet components at $\lambda = 777.2$, 777.4, and 777.5 nm, respectively.

Both A(O) and S_{H} are significantly higher than inferred from the center-to-limb variation of the line profiles in the WCLC and Pereira spectra. We have to conclude that neither the fitting errors nor the line-to-line variation of A(O) represent a valid estimate of the true uncertainty of the derived oxygen abundance. Rather, systematic errors must be the dominating factor. We shall demonstrate in the next Section that the result of simultaneously fitting the intensity and flux profiles is very sensitive to small errors in measuring or modelling the relative line strengths in the disk-center and integrated disk spectra. We therefore consider the oxygen abundance derived from fitting the spectra at several μ-angles simultaneously as more reliable.

3.6 Equivalent width fitting and results

Another possible methodology for estimating the solar oxygen abundance is based on the comparison of the observed and theoretical center-to-limb variation of equivalent widths (Ws). Matching the W of the lines is admittedly less precise than line profile fitting: it is possible that synthetic and observed Ws match perfectly, while the line profiles exhibit significantly different shapes. However, W-fitting has the advantage of being simpler: there are only two free fitting parameters, A(O) and S_{H}. The additional fitting parameters that were necessary in the case of line profile fitting, related to extra line broadening and line shifts, have no influence on the equivalent width and thus are irrelevant for the W fitting procedure.

3.6.1 Equivalent width measurements

For a given model atmosphere, a grid of theoretical equivalent widths, $W_{\mathrm{calc}}(\mu)$, is computed as a function A(O) and S_{H} by integrating the NLTE synthetic line profile over a wavelength interval of ±2 Å, separately for each triplet component. Here the inclination angle μ covers the values for both observed spectra (WCLC and Pereira). In addition, the equivalent widths of the disk-integrated line profiles were obtained by appropriate μ-integration, denoted as $\overline{W}_{\mathrm{calc}}$ in the following.

The Ws of the observed line profiles, $W_{\mathrm{obs}}(\mu)$, $\overline{W}_{\mathrm{obs}}$, are obtained as a by-product of the 3D NLTE line profile fitting (see Sect. 3.5): $W_{\mathrm{obs}} = W_{\mathrm{calc}}(\mathrm{A(O)}^*, S^*_{\mathrm{H}})$, where $\mathrm{A(O)}^*$ and S^*_{H} are the best-fit parameters for the respec-

Table 3.2. *W*s of the O I IR triplet as a function of μ measured from the different spectra with our line profile fitting method (this work); for the Pereira spectra, we also give the original measurements taken from Pereira et al. (2009b).

	Equivalent width (pm)		
	O I 7772	O I 7774	O I 7775
μ	Spectrum: Neckel & Labs (1984), *W*: this work		
1.00	8.73 ± 0.050	7.60 ± 0.044	6.01 ± 0.035
flux	7.54 ± 0.043	6.52 ± 0.038	5.07 ± 0.029
μ	Spectrum: WCLC, *W*: this work		
1.00	8.73 ± 0.040	7.51 ± 0.035	5.95 ± 0.027
0.87	8.27 ± 0.038	7.13 ± 0.033	5.63 ± 0.026
0.66	7.33 ± 0.034	6.34 ± 0.029	5.02 ± 0.023
0.48	6.54 ± 0.030	5.62 ± 0.026	4.36 ± 0.020
0.35	5.94 ± 0.027	5.08 ± 0.023	3.79 ± 0.017
0.25	5.44 ± 0.025	4.63 ± 0.021	3.40 ± 0.016
μ	Spectrum: Pereira et al. (2009b), *W*: this work		
1.00	8.63 ± 0.060	7.55 ± 0.052	5.99 ± 0.041
0.816	8.08 ± 0.056	7.03 ± 0.049	5.54 ± 0.038
0.608	7.22 ± 0.050	6.25 ± 0.043	4.85 ± 0.034
0.424	6.33 ± 0.044	5.46 ± 0.038	4.16 ± 0.029
0.197	4.94 ± 0.034	4.16 ± 0.029	3.02 ± 0.021
μ	Spectrum and *W*: Pereira et al. (2009b)		
1.00	8.48 ± 0.09	7.44 ± 0.09	5.90 ± 0.09
0.816	8.00 ± 0.14	6.96 ± 0.15	5.47 ± 0.11
0.608	7.21 ± 0.09	6.21 ± 0.09	4.83 ± 0.09
0.424	6.38 ± 0.10	5.44 ± 0.10	4.17 ± 0.10
0.197	5.09 ± 0.10	4.22 ± 0.33	3.08 ± 0.28

tive line profile, obtained by fitting each μ-angle individually. This method of *W* measurement ensures an optimal consistency between observed and theoretical equivalent widths. The errors of the observed *W*s, σ_{o}, were estimated from the fitting errors of A(O) and S_{H} for the best-fitting theoretical line profile. The *W*s of the O I IR triplet measured in this way are listed in Tab. 3.2 for all spectra; for the Pereira spectra, we also give the original measurements by Pereira et al. (2009b) (bottom). The *W*s from both the WCLC and the Pereira spectra, as collected in Tab. 3.2, are plotted in Fig. 3.4.

The *W*s derived with our method from the Pereira spectra are generally slightly larger than those measured by the authors of the original work. This is because we integrate the synthetic single line profile over a very broad wavelength window. Since the O I lines have extended Lorentzian wings, our *W*s are systematically higher. For the weakest lines at $\mu = 0.197$, the impact of

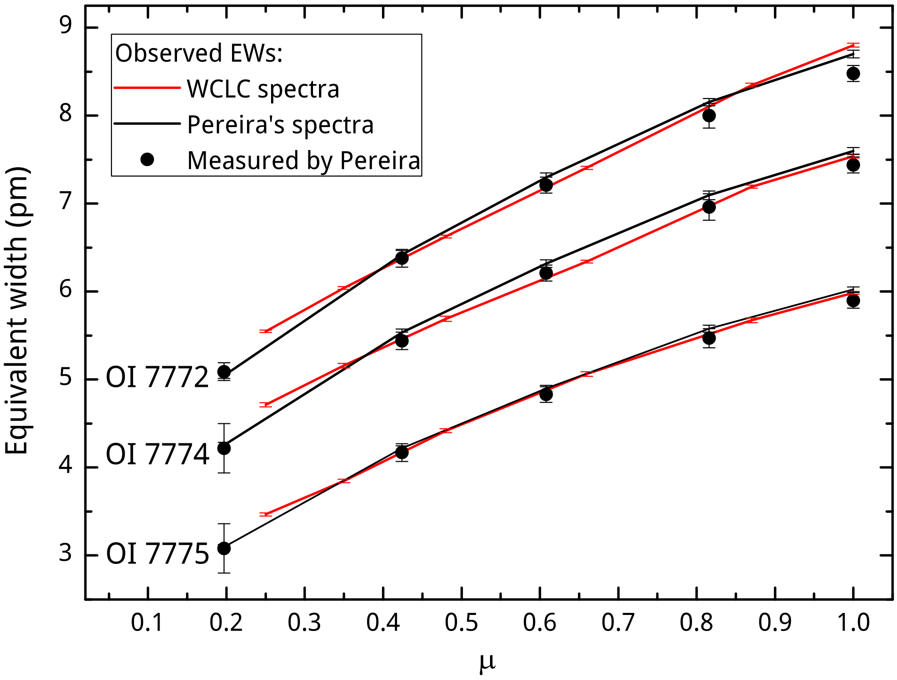

Fig. 3.4. Equivalent widths as measured in this work from WCLC and Pereira's spectra (red and black lines, respectively), compared to the measurements taken from the work of Pereira et al. (2009b) (black dots). See Table 3.2 for more details.

the Lorentzian wings is diminished, and the two measurements are in very close agreement (see Table 3.2). We argue that, for the purpose of W fitting, our W measurement method is superior to direct integration of the observed line profiles because it ensures consistency of theoretical and observed Ws.

3.6.2 *W* fitting of disk-center and full-disk spectra

We first apply the method to determine S_H and A(O) from the simultaneous fit of the disk-center and disk-integrated Ws in the Neckel intensity and flux spectra, respectively. For this purpose, we compute for each of the three triplet components two grids of equivalent widths, $W(S_\mathrm{H}, \mathrm{A(O)}; \mu{=}1)$ and $W(S_\mathrm{H}, \mathrm{A(O)}; \mathrm{flux})$, from the corresponding sets of 3D NLTE line profiles. These grids are then used to construct contour lines in the S_H – A(O) plane where $W_\mathrm{calc} = W_\mathrm{obs}$, as shown in Fig. 3.5. The thick (red) solid line and the thick (green) dashed line refers to the W measured in the Neckel disk-center and disk-integrated (flux) spectrum, respectively (see Table 3.2). The slope of the contour line of the flux W is somewhat steeper than that for disk-center, indicating that the lines in the flux spectrum are slightly more sensitive to changes in S_H. The unique solution (S_H, A(O)) defined by the intersection point of the two lines (red diamond) is given in the legend of each panel.

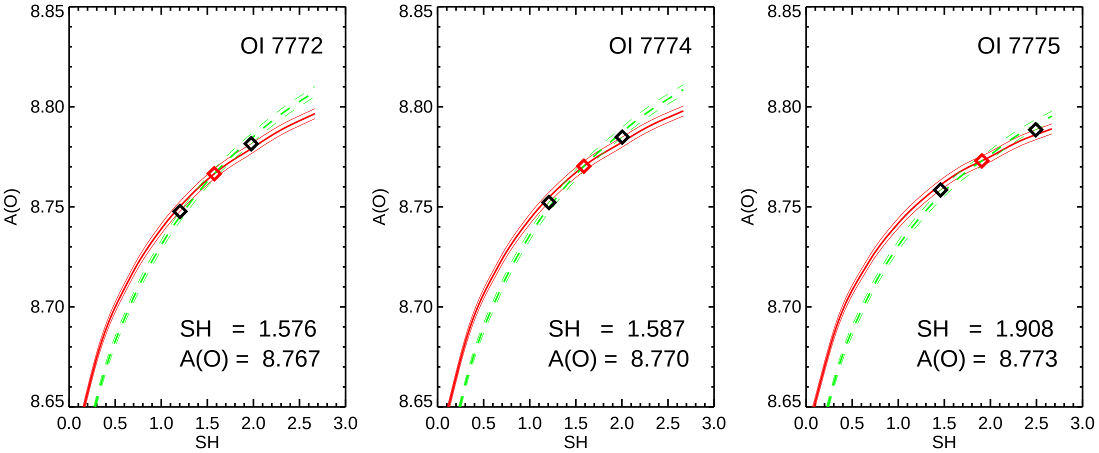

Fig. 3.5. Lines of constant equivalent width in the S_{H} – A(O) plane, as computed from the grid of 3D NLTE synthetic line profiles for the three triplet components. The thick (red) solid line refers to the W measured in the Neckel disk-center spectrum, while the thick (green) dashed line is for the measured W in the Neckel disk-integrated (flux) spectrum. The solution (S_{H}, A(O)) given in the legend is defined by the intersection point of the two lines (red diamond). The black diamonds define the uncertainty range of the solution, assuming an W measurement error of $\approx 0.5\%$, as indicated by the thin lines offset from the original S_{H} – A(O) relations by $\pm\Delta$A(O) = 0.0025.

Since the angle at which the two lines intersect is rather small, the position of the intersection point is very sensitive to the exact values of the two equivalent widths. To quantify the uncertainties, we have also plotted in Fig. 3.5 (thin lines) the contour lines shifted up and down by ΔA(O)= ± 0.0025 dex, corresponding to errors in W of less than 0.5%. The black diamonds show the solutions obtained by changing the two Ws by this small amount in opposite directions. With this definition of the error bars, we find A(O) = 8.77 ± 0.02, S_{H}= 1.85 ± 0.65.

These results are somewhat lower than the corresponding results obtained from line profile fitting (Sect. 3.5.3) , with a marginal overlap of the error bars. We conclude that the idea of simultaneously fitting intensity and flux spectra works in principle, but is highly sensitive to small errors in the measured Ws and to systematic errors in modeling the μ dependence of the oxygen triplet lines. The results obtained with this method are therefore only considered a rough indication of the range of A(O) compatible with our modeling. As we see below, a more accurate determination of the oxygen abundance is possible when fitting simultaneously the line profiles measured at different μ-angles.

3.6.3 *W* fitting of the μ-dependent WCLC and Pereira spectra

We now determine S_{H} and A(O) from the simultaneous fit of the Ws at all μ-angles, using the two independent sets of observed μ-dependent spectra of

WCLC and Pereira, respectively. As before, we treat the three triplet components separately. In contrast to the method employed by Pereira et al. (2009b), we do not assign a special role to the fit at disk center. In our case, the idea is to find the minimum χ^2 in the S_{H} – A(O) plane, where χ^2 is defined as

$$\chi^2(S_{\mathrm{H}}, \mathrm{A(O)}) = \sum_{\mathrm{j=1}}^{m} \frac{\left(W_j^{\mathrm{obs}} - W_j^{\mathrm{calc}}(S_{\mathrm{H}}, \mathrm{A(O)})\right)^2}{\sigma_{1,j}^2 + \sigma_{2,j}^2}\,. \tag{3.3}$$

We sum over the different μ-angles ($j = 1 \ldots m$); W^{obs} and W^{calc} are the measured and computed equivalent width, respectively; σ_1 is the measurement error of W^{obs} as given in Table 3.2, and σ_2 is the observational error due to insufficient time averaging given the limited field of view covered by the slit on the solar surface. The error σ_2 is only considered in case of the WCLC spectra, where the exposure times are less than the typical granule lifetime and the slit

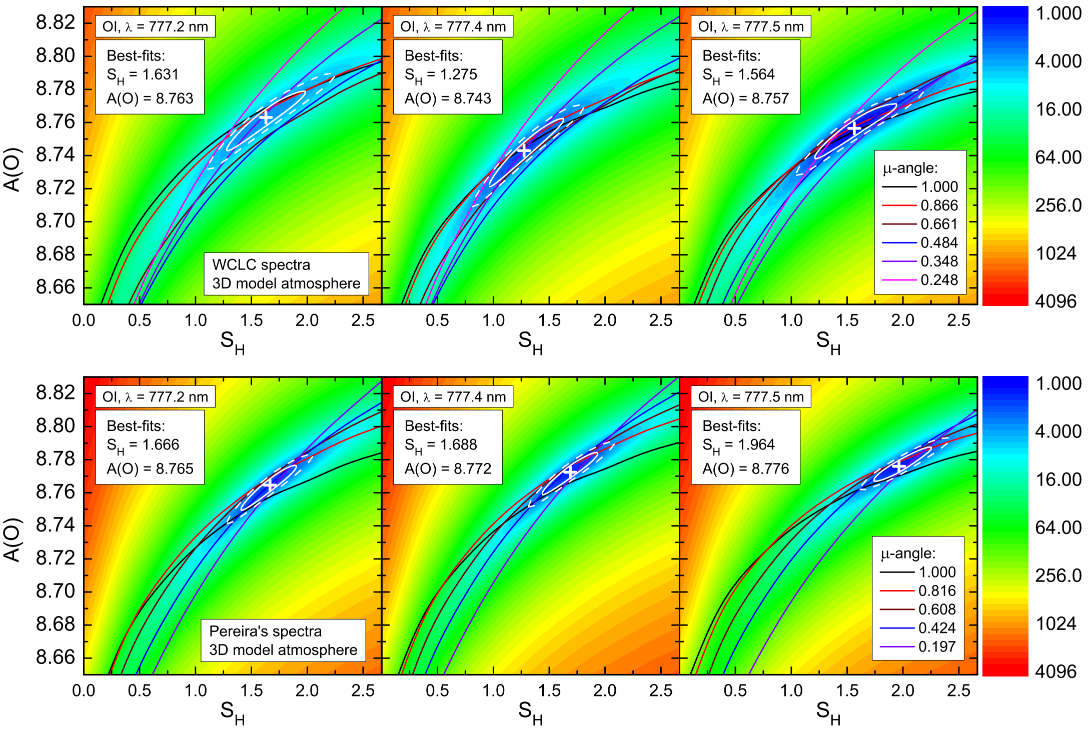

Fig. 3.6. Maps of χ^2 (color-coded) in the S_{H} – A(O) plane, indicating the quality of the simultaneous fit over all μ-angles of observed and computed 3D NLTE W, considering each of the three triplet components separately. The location of the minimum χ^2 is marked by a white plus sign, while the white ellipses bound the regions where $\chi^2 - \chi^2_{\mathrm{min}} < 1$ (solid) and 2.3 (dashed). The latter corresponds to the simultaneous confidence region of S_{H} and A(O) containing 68.3 % in the case of normally distributed data. Contour lines indicating where $W_{\mathrm{obs}} = W_{\mathrm{calc}}$ are superimposed for each μ-angle. The top and bottom panels show the results for the WCLC and Pereira spectra, respectively. Line identification and best-fit parameters are given at the top left of each panel.

covers roughly three times the surface area of the 3D model. We derive σ_2 from a bootstrap-like test, where a random subsample of three different snapshots is repeatedly drawn from a larger sample of 20 3D snapshots without replacement. For each μ-value, we generated 10 000 realizations of the possible appearance of the solar surface in the field of view, using the same A(O) – S_{H} combination as for the equivalent width measurement (see above). The trial-to-trial variance of the derived distribution of the subsample averaged Ws is then taken as σ_2. Pereira's spectra have much better statistics (large number of observations per μ-angle), and there is no need to consider this kind of measurement error in the case of these spectra.

For the purpose of W fitting, we compute a grid of equivalent widths, $W(S_{\mathrm{H}}$, A(O); $\mu)$ from the corresponding sets of 3D NLTE line profiles, where $0 \leq S_{\mathrm{H}} \leq 8/3$, $8.65 \leq$ A(O) ≤ 8.83, and μ covering the observed limb angles. This allows us to compute $\chi^2(S_{\mathrm{H}}, \mathrm{A(O)})$ in the S_{H} – A(O) plane, separately for each of the three triplet components, as shown in Fig. 3.6 for both observational data sets. The best-fit solution is defined by the location of the minimum of χ^2, as indicated in the plots by a white plus sign, which is found by W interpolation using third-order polynomials.

Table 3.3. Results of NLTE W fitting with various model atmospheres: A(O), S_{H}-values, and reduced χ^2 of the best fit for two different observed spectra (WCLC and Pereira 2009); the difference between A(O) derived from the two different spectra is given in Col. (4). Results from the ⟨3D⟩ and `LHD` model atmospheres are excluded because no minimum in χ^2 is found in the range $S_{\mathrm{H}} > 0$.

	A(O)		S_{H}		χ^2_{red}	
Data set:	WCLC	Pereira	WCLC	Pereira	WCLC	Pereira
λ, nm	3D model atmosphere					
777.2	8.763 ± 0.018	8.765 ± 0.014	1.63 ± 0.35	1.67 ± 0.25	0.831	0.500
777.4	8.743 ± 0.021	8.772 ± 0.013	1.28 ± 0.33	1.69 ± 0.25	0.448	0.457
777.5	8.757 ± 0.017	8.776 ± 0.010	1.56 ± 0.36	1.96 ± 0.26	0.235	0.401
Mean	8.754 ± 0.010	8.771 ± 0.006	1.49 ± 0.19	1.77 ± 0.17	–	–
λ, nm	HM model atmosphere, $\xi_{\mathrm{mic}} = 0.8$ km/s					
777.2	8.699 ± 0.030	8.677 ± 0.031	0.55 ± 0.25	0.38 ± 0.16	2.135	0.989
777.4	8.689 ± 0.031	8.705 ± 0.022	0.42 ± 0.22	0.49 ± 0.17	1.414	0.477
777.5	8.731 ± 0.022	8.748 ± 0.014	0.73 ± 0.26	0.90 ± 0.19	0.371	0.159
Mean	8.706 ± 0.022	8.710 ± 0.035	0.57 ± 0.16	0.59 ± 0.28	–	–
λ, nm	HM model atmosphere, $\xi_{\mathrm{mic}} = 1.2$ km/s					
777.2	8.670 ± 0.044	8.650 ± 0.026	0.50 ± 0.21	0.36 ± 0.08	2.330	1.371
777.4	8.660 ± 0.030	8.674 ± 0.026	0.37 ± 0.16	0.42 ± 0.16	1.578	0.695
777.5	8.705 ± 0.023	8.721 ± 0.015	0.65 ± 0.25	0.80 ± 0.18	0.420	0.208
Mean	8.678 ± 0.024	8.682 ± 0.036	0.51 ± 0.14	0.52 ± 0.24	–	–

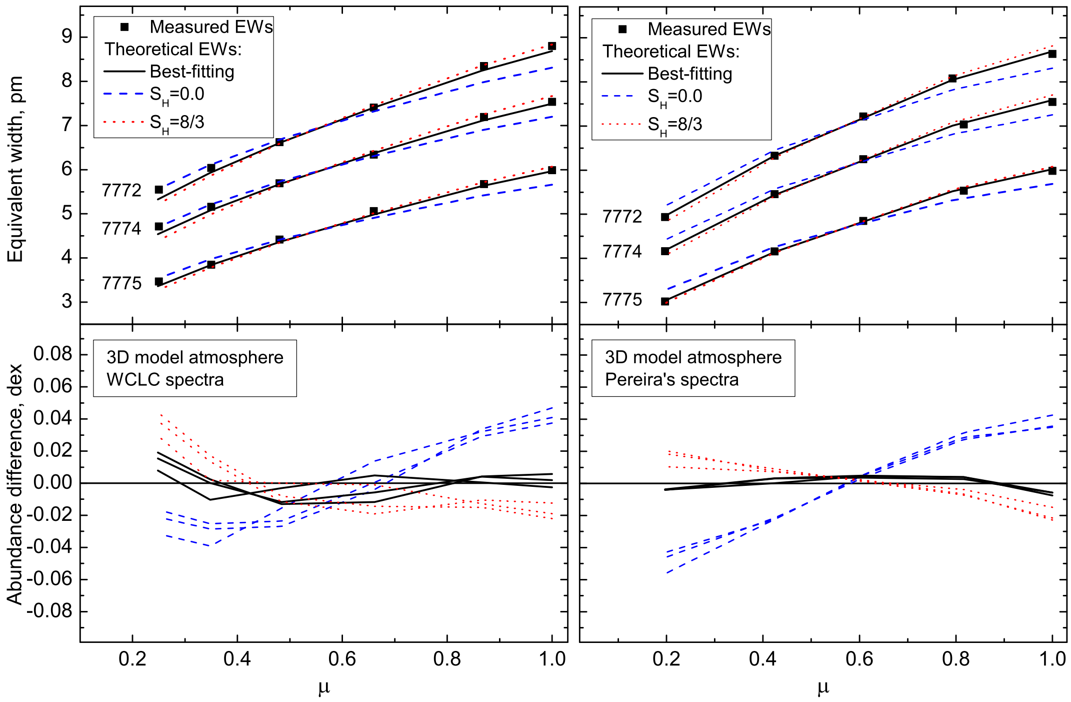

Fig. 3.7. *Top panels*: center-to-limb variation of observed (symbols) and theoretical Ws derived from the 3D model atmosphere for S_{H}=0 (blue dashed), 8/3 (red dotted) and best-fit value (black solid), shown individually for the three triplet components, with wavelength increasing from top to bottom. For each S_{H}, the corresponding A(O) is defined as the value that minimizes χ^2 (Eq. 3.3) at fixed S_{H}. *Bottom panels*: abundance difference A(μ) - $\overline{\mathrm{A}}$, where A(μ) and $\overline{\mathrm{A}}$ denote A(O) obtained from line profile fitting at individual μ-angles and at all μ-angles simultaneously. Left and right panels refer to the WCLC and Pereira spectra, respectively.

The results of the W fitting for various model atmospheres are summarized in Table 3.3, listing A(O) and S_{H} of the best fit for the WCLC and Pereira observed spectra. The fitting errors of A(O) and S_{H} are given by the projection of the contour line defined by $\chi^2 - \chi^2_{\mathrm{min}} = 1$ (white ellipse in Fig. 3.6) on the A(O) and S_{H} axis, respectively. We also provide the reduced χ^2 of the best fit, which is defined as $\chi^2_{\mathrm{red}} = \chi^2/(m-p)$, where $p = 2$ is the number of free fitting parameters, as a measure of the quality of the fit.

The high quality of the W fit achieved with the 3D model is also illustrated in Fig. 3.7, where we show the center-to-limb variation of observed and theoretical Ws for the best-fitting parameters and for the two extreme values S_{H}=0 and 8/3. Corresponding plots for all 1D model atmospheres investigated in this work are provided in appendixes of Steffen et al. (2015).

To derive the best estimate the solar oxygen abundance from W fitting, we rely on the results of the 3D model atmosphere, which show the smallest line-to-line scatter and the lowest χ^2. Computing the mean and errors for the two data sets as before in Sect. 3.5.2, we obtain $\langle \mathrm{A(O)} \rangle = 8.754 \pm 0.010$ dex (WCLC data set) and $\langle \mathrm{A(O)} \rangle = 8.771 \pm 0.006$ dex (Pereira data set). Again, the $1\,\sigma$ fitting error bars of these two abundance estimates do not overlap (by a narrow margin). Nevertheless, we derive the best estimate by averaging over the two data sets, arriving at $\langle\langle \mathrm{A(O)} \rangle\rangle = 8.763 \pm 0.012$, and $\langle\langle S_{\mathrm{H}} \rangle\rangle = 1.6 \pm 0.2$. These numbers are fully consistent with the final result obtained from the line profile fitting described in Section 3.5.2. As in the latter case, the best-fit solutions, derived from the ⟨3D⟩ and 1D LHD modelling, turn out to be unphysical (negative S_{H}). We discard these results as irrelevant and exclude them from Table 3.3 (see also Sect. 3.7.2 below).

3.7 Discussion

3.7.1 Comparison with previous work

In the present work, we simultaneously derived the oxygen abundance, A(O), and the scaling factor for collisions with neutral hydrogen, S_{H}, using two different methods of analyzing the μ-dependent spectra of the O I IR triplet: line profile fitting and equivalent width fitting. While the former method yields $\mathrm{A(O)} = 8.757 \pm 0.010$, $S_{\mathrm{H}} = 1.6 \pm 0.2$, the latter gives $\mathrm{A(O)} = 8.763 \pm 0.012$, $S_{\mathrm{H}} = 1.6 \pm 0.2$. In both methods, the spectra at the different μ-angles are assigned equal weight.

Pereira et al. (2009b) followed a different methodology, using a mix of W-fitting and line profile fitting, and assigning a distinguished role to the fits at disk center. More precisely, they first derive S_{H} from simultaneously fitting the equivalent widths at all μ-angles and all three triplet components. For a given S_{H}, the oxygen abundance is varied to find the local minimum $\chi^2(S_{\mathrm{H}})$. Then the minimum of this function defines the global minimum of χ^2, which corresponds to their best-fitting global value of $S_{\mathrm{H}} = 0.85$. Fixing S_{H} at this value, these authors determine the oxygen abundance by fitting the line profiles at disk center, separately for each triplet component, and average the resulting A(O) values to obtain their best estimate of the oxygen abundance, $\mathrm{A(O)} = 8.68$.

In Fig. 3.8, we show a comparison of the A(O) – S_{H} relation obtained from our 3D NLTE modeling with the results of Pereira et al. (2009b), for each of the three triplet lines and the two different disk-center spectra. For a given S_{H}, the oxygen abundance is determined from disk-center line profile fitting, as described in Sect. 3.5.1 (first sweep, but with fixed S_{H}). The figure immediately

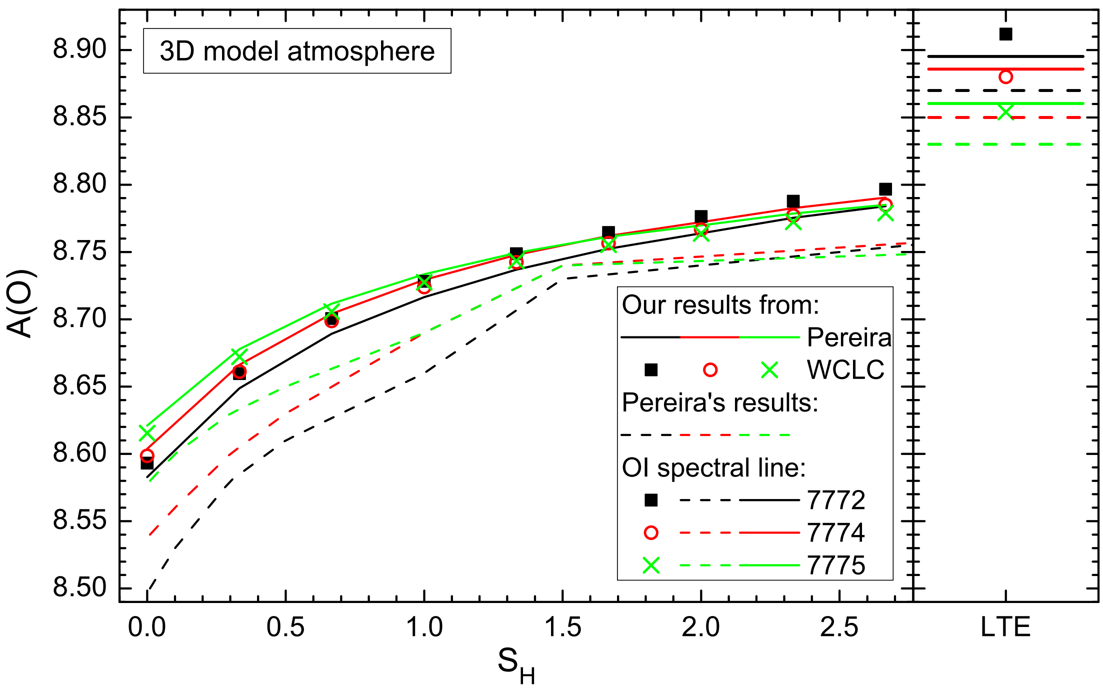

Fig. 3.8. Oxygen abundance determined from disk-center line profile fitting as a function of S_H for the three triplet lines and the two different observed spectra. The 3D NLTE results of the present work (solid lines, symbols) are compared with those of Pereira et al. (2009b, Tab. 3, dashed lines), obtained from their profile fits of the same disk-center spectra.

shows that our A(O) – S_H relation differs significantly from that of Pereira et al. (2009b, their Table 3), implying a systematically higher A(O) for given S_H. For the value $S_H = 0.85$, which was determined by Pereira et al. (2009b), our relation suggests A(O) ≈ 8.71 – 8.72. This value is clearly incompatible with the value A(O) ≈ 8.64 – 8.68, found by the latter authors. However, we are cautious about making a direct comparison of the A(O) – S_H relations since possible differences in the particular implementation of the Drawin formula (definition of S_H) might introduce a bias (see Sect. 3.7.3). This is the case with the exception of $S_H = 0$ and ∞ (LTE).

In addition, the line profile fits that we achieve with our 3D NLTE synthetic line profiles (see Fig. 3.3) are superior to the fitting results shown in the work of Pereira et al. (2009b) (see their Fig. 6 and Sect. 4.1.2.) where, generally, a less perfect agreement was found.

We can only speculate about what causes the systematic difference between our results and those obtained by Pereira et al. (2009b). Differences in the employed oxygen model atom, the adopted atomic data (like photoionization and collisional cross sections), and other numerical details entering the solution of the NLTE rate equations, are among the prime suspects. Since we even see systematic A(O) differences of about 0.03 dex in LTE (right column of Fig. 3.8), we conclude that differences in the 3D hydrodynamical model atmospheres and / or the spectrum synthesis codes must also play a role.

Also, as described in Sect. 3.6.1, we systematically derive larger equivalent widths than Pereira et al. (2009b) near the disk center and lower *W*s near the limb, from the same observed spectra (see Table 3.2) due to different measurement methods. One might therefore ask how much of the difference between the oxygen abundance derived in the present work and by Pereira et al. can be ascribed to differences in the measured equivalent widths. To answer this question, we have repeated our 3D NLTE *W* fitting procedure with the original equivalent widths as given by Pereira et al. (2009b). We find that the derived oxygen abundance decreases by $\Delta\mathrm{A(O)} \approx -0.045$ dex, explaining roughly half the discussed A(O) discrepancy. We point out, however, that the almost perfect consistency between profile fitting and *W* fitting results is destroyed if we were to adopt the equivalent widths measured by Pereira et al. (2009b). Note also that the mismatch illustrated in Fig. 3.8 is completely independent of any *W* measurements.

It seems very likely that the above mentioned differences in the theoretical 3D NLTE modeling are the main reason for the discrepancy in the final oxygen abundance of almost 0.1 dex between the present work and that of Pereira et al. (2009b). The different approaches of analyzing the data constitute an additional source of uncertainty.

3.7.2 Interpretation of the obtained 1D NLTE results

As mentioned in Sect. 3.5, the oxygen abundance derived from line profile fitting based on 1D models (in particular ⟨3D⟩ and `LHD`) is significantly lower, by up to -0.15 dex, than the value derived with the 3D modeling. A very similar discrepancy between 1D and 3D results is obtained from the method of equivalent width fitting. The main reason is that the 1D models predict a steeper gradient of the line strength with respect to limb angle μ. Under such circumstances, the best global fit of the observed center-to-limb variation of the triplet lines would formally require a negative S_H, as demonstrated in Fig. 3.9. Because of the tight correlation between S_H and A(O) (see Fig. 3.8), a low S_H implies a low oxygen abundance: while $S_\mathrm{H} \approx 1.6$ for the 3D model, $S_\mathrm{H} \equiv 0$ for the ⟨3D⟩ and `LHD` models, explaining the exceedingly low oxygen abundance derived with these 1D models. We add that our findings are in line with the results of Pereira et al. (2009b, their Fig. 5).

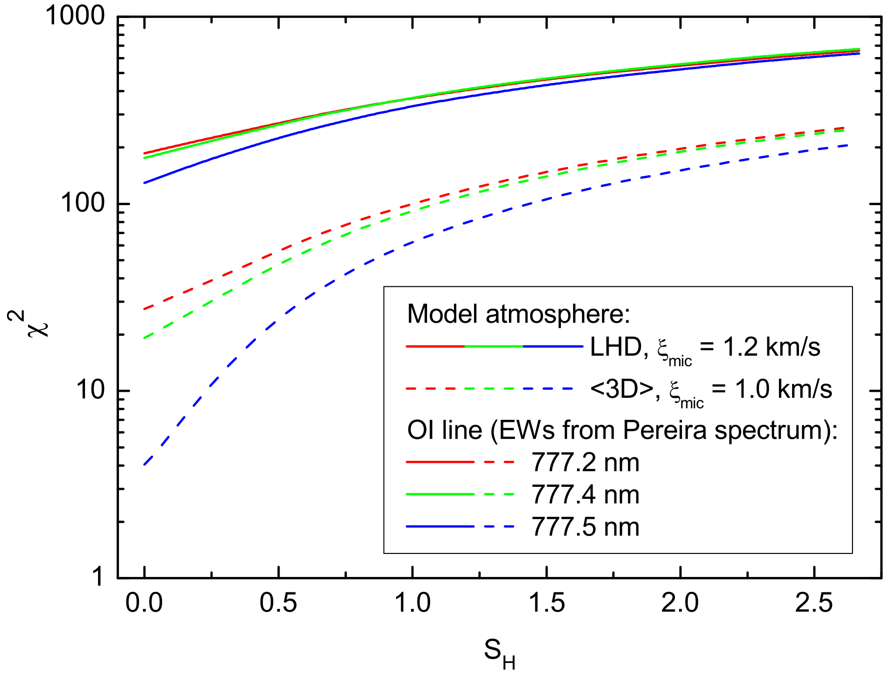

Fig. 3.9. Minimum χ^2 as a function of $S_{\rm H}$ obtained from global W fitting with the ⟨3D⟩ and `LHD` model atmospheres. For each of the three triplet lines, we plot the minimum of χ^2 (nonreduced) at fixed $S_{\rm H}$. No minimum of χ^2 is found in the range $0 \leq S_{\rm H} \leq 8/3$. At $S_{\rm H}$=0, the implied oxygen abundances are A(O) = 8.61, 8.62, 8.63 (⟨3D⟩), and A(O) = 8.59, 8.60, 8.61 (`LHD`), for λ 777.2, 777.4, and 777.5 nm, respectively. The best fits would be obtained at negative $S_{\rm H}$ and even lower A(O).

Since the triplet lines are partially saturated, their formation is sensitive to the choice of the microturbulence parameter, $\xi_{\rm mic}$, to be used with the 1D models. While the value of $\xi_{\rm mic}$ can be determined empirically, the main issue in the present context is the common assumption that $\xi_{\rm mic}$ is independent of μ. In fact, it is well known empirically that both micro- and macroturbulence increase towards the solar limb (e.g., Holweger et al. 1978). Evidently, we could improve the quality of the 1D fits by introducing a μ-dependent microturbulence parameter. With a more realistic $\xi_{\rm mic}$ increasing towards the limb, the slope of $W(\mu)$ at fixed A(O) would diminish, such that the best fit would require a larger (positive) $S_{\rm H}$ and hence a higher oxygen abundance. Although it may be worthwhile, we have refrained from exploring the effects of a μ-dependent microturbulence on the results of the 1D models in the present work.

It is obvious that the 1D models with a fixed microturbulence are unrealistic, and lead to unphysical conclusions about the scaling factor ($S_{\rm H} < 0$). The oxygen abundance derived from these 1D models for the O I IR triplet lines is therefore systematically biased towards exceedingly low values. Even though the analysis based on the HM model atmosphere yields positive $S_{\rm H}$ values, the

Table 3.4. Results of NLTE W fitting with various model atmospheres for given disk-center equivalent width W_1 (as measured from the Pereira data set, see Table 3.2) and $S_{\rm H}$-factor (as obtained from the global W fit with the 3D model, see Table 3.3). The oxygen abundance A(O) required to reproduce W_1 with the 3D, averaged 3D, HM, and LHD model, respectively, is listed in Cols. (4) – (7). For all 1D models, a microturbulence of $\xi_{\rm mic}$ = 1.0 km/s is assumed.

λ [nm]	W_1 [pm]	$S_{\rm H}$	A(O) 3D	⟨3D⟩	HM	LHD
777.2	8.63	1.67	8.758	8.744	8.753	8.686
777.4	7.55	1.69	8.766	8.753	8.765	8.695
777.5	5.99	1.96	8.770	8.759	8.778	8.703
Mean	–	–	8.765	8.752	8.765	8.695

resulting A(O) is considered as misleading, too, since the HM model suffers from the same microturbulence issues as the ⟨3D⟩ and `LHD` models, albeit in a less obvious way, because the problems are somehow masked by the empirical temperature structure of the HM model. Consequently, we have ignored all 1D results for the estimation of the final solar oxygen abundance. We rather rely on the analysis with the 3D model, which has a built-in hydrodynamical velocity field that properly represents a μ-dependent micro- and macroturbulence.

As described above, the microturbulence problem renders a direct comparison of the abundance determinations from 1D and 3D models meaningless. Nevertheless, it is possible to ask what oxygen abundance would be obtained from the 1D models if we use the same $S_{\rm H}$-value as found in the 3D analysis, i.e., considering this $S_{\rm H}$-value as a property of the model atom. Fixing $S_{\rm H}$ in this way, we determined A(O) from the 1D models by fitting the observed equivalent width at disk center, assuming the canonical microturbulence value of $\xi_{\rm mic}$ = 1.0 km/s. The results are summarized in Table 3.4.

Remarkably, the HM model atmosphere requires almost exactly the same oxygen abundance as the 3D model to match the measured disk-center equivalent width. This is indeed what is expected from a semi-empirical model. The averaged 3D model gives only a slightly lower A(O), suggesting that the effect of horizontal inhomogeneities is of minor importance, at least for the line formation at $\mu = 1$. In contrast, the LHD model indicates a significantly lower oxygen abundance, which we attribute to the somewhat steeper temperature gradient in the line forming region (see Fig. 3.1).

3.7.3 Treatment of inelastic collisions with neutral hydrogen

Collisions of neutral oxygen atoms with neutral hydrogen give rise to bound-bound (excitation) and bound-free (ionization) transitions. As shown previously, they play a very important role in establishing the statistical equilibrium level population of O I. Unfortunately, quantum mechanical calculations or experimental measurements of the relevant collisional cross sections are so far unavailable. We have therefore resorted to calculating the excitation and ionization rates due to collisions by neutral hydrogen by the classical Drawin formula. Following common practice, we scaled the resulting rates by an adjustable factor, S_{H}, which is determined from the best fit to the observations together with the oxygen abundance, as detailed above.

In the present work, the cross sections for inelastic collisions with neutral hydrogen are computed according to the classical recipe of Drawin (Drawin 1969; Steenbock & Holweger 1984; Lambert 1993), and hence are proportional to the oscillator strength f for all bound-bound transitions. For optically forbidden transitions, the collisional cross section is therefore zero. All hydrogen related collision rates included in our oxygen model atom, bound-bound and bound-free, are then scaled by the same factor S_{H}. It is not clear whether other authors (e.g., Pereira et al. 2009b) might have adopted different assumptions. We have therefore investigated two test cases to understand the consequences for the derived oxygen abundance of (i) allowing for collisional coupling through optically forbidden transitions, and (ii) assuming a constant collision strength independent of f for all allowed transitions.

To reduce the computational cost, we have restricted the test calculations to W fitting of the Pereira data set, using the HM 1D model atmosphere with ξ_{mic}=1.2 km/s. The results are summarized in Table 3.5. The oxygen abundance and S_{H}-factor obtained with the standard setup are shown in Cols. (2) and (3) ('Case 0', cf. Table 3.3).

In 'Case 1', we have included collisional excitation for all possible transitions according to the Drawin formula, where the cross sections of the optically allowed transitions are proportional to the oscillator strength f (as in 'Case 0'). In this case, an effective minimum oscillator strength of $f = 0.001$ is adopted for all forbidden transitions, including the transitions between the triplet and quintuplet system, as suggested by Fabbian et al. (2009). Scaling by S_{H} is restricted to the allowed transitions. The effect of the additional collisional coupling via

Table 3.5. Resulting oxygen abundance A(O) and scaling factor S_H derived from NLTE W fitting of the Pereira data set, using the HM model atmosphere with ξ_mic=1.2 km/s. Cases (0) – (2) refer to different assumptions about the excitation rates due to collisions by neutral hydrogen (see text for details).

λ	Case 0		Case 1		Case 2	
[nm]	A(O)	$S_\mathrm{H}^{(0)}$	ΔA(O)	$S_\mathrm{H}^{(1)}/S_\mathrm{H}^{(0)}$	ΔA(O)	$S_\mathrm{H}^{(2)}/S_\mathrm{H}^{(0)}$
777.2	8.650	0.36	−0.004	0.818	−0.011	0.515
777.4	8.674	0.42	−0.005	0.854	−0.014	0.512
777.5	8.721	0.80	−0.003	1.000	−0.006	0.722
Mean	8.682	0.52	−0.004	0.891	−0.010	0.583

the forbidden transitions on the oxygen abundance derived from W fitting of the triplet lines is marginal: on average, A(O) is reduced by only 0.004 dex.

In ‘Case 2’, the treatment of the collisional coupling in the forbidden transitions is the same as in ‘Case 1’, but the cross sections of all optically allowed transitions are computed with $f = 1$. Again, scaling by S_H is restricted to the allowed transitions. The effect of removing the proportionality between collision strength and oscillator strength for the allowed transitions on the derived oxygen abundance amounts to ≈ -0.01 dex, while the numerical value of the required S_H is reduced by roughly a factor 2 with respect to ‘Case 0’.

The effects shown in Table 3.5 are expected to be of similar magnitude in the full 3D analysis. We conclude from this experiment that the oxygen abundance derived from the NLTE analysis of the O I IR triplet lines is not particularly sensitive to the details of the implementation of the Drawin formula, even if the numerical value of S_H can differ significantly.

Although this approach is commonly accepted, the assumption of a universal scaling factor is questionable. It could well be that each line is characterized by a slightly different value of S_H, and / or that individual bound-bound and bound-free transitions require significantly different scaling factors. This would not be surprising, as it is well known that the classical treatment of collisions does not have a rigorous physical foundation. In fact, such nonuniform scaling has recently been demonstrated for Mg + H by Barklem et al. (2012). In principle, S_H should depend on temperature (see Barklem et al. 2011) and, because the different triplet lines form at different atmospheric heights, S_H could be expected to vary slightly from line to line. Our analysis allows for this possibility, since we treat each of the triplet components separately. However, we do not find any systematic trend in S_H with wavelength, and consider the line-to-line variation of S_H as random, reflecting the intrinsic uncertainties of our method. With this reasoning, a systematic variation of S_{H} as a function of the limb angle also seems unlikely, and our analysis assumes a μ-independent S_{H}. In summary, the treatment of the collisions by neutral hydrogen in terms of the empirical scaling factor S_{H} appears unsatisfactory.

Chapter 4

Influence of convection on the formation of molecular spectral lines in the atmospheres of RGB stars

4.1 Introduction

Carbon, nitrogen, and oxygen (CNO) are important chemical elements that could be used to trace early evolution of galaxies. However, abundances of these elements are studied using rather weak atomic spectral lines that become invisible in spectra of metal-poor stars ([Fe/H] < –3). Moreover, the number of atomic CNO lines is small. In such stars the only probes of CNO abundances are molecular lines.

By applying `STAGGER` model atmospheres, Asplund & García Pérez (2001) has performed 3D analysis of OH line formation in the atmospheres of turn-off stars, while Collet et al. (2007) investigated formation of various molecules in RGB stars. Both groups of authors found significant impact of 3D hydrodynamical effects on molecular abundances that are mainly caused by horizontal fluctuations of thermodynamic and hydrodynamical quantities in stellar atmospheres. These fluctuations led to the appearance of the cool photospheric layer that is characterized by much lower temperatures than those in the counterpart 1D models and, hence, for more efficient formation of molecules. Higher number densities of molecular absorbers lead towards stronger theoretical spectral lines and lower abundance estimates. Collet et al. (2007) found that for some molecular lines the 3D hydrodynamical effects may reduce abundance estimates by 1.2 dex.

In this Chapter we therefore use CO^{5}BOLD model atmospheres of RGB stars to study the role of 3D hydrodynamical effects in the formation of molecular lines in stellar atmospheres. We focus not only on oxygen-bearing molecules, because, as it will be shown below, formation of different molecules in stellar atmospheres is interrelated in various complex ways, thus in order to gain a deeper understanding of this phenomenon, an extended analysis was required.

Table 4.1. Characteristics of the `CO5BOLD` and `LHD` model atmospheres used in this study.

(1) Name	(2) $\langle T_{\rm eff}\rangle$ K	(3) $\log g$ [cgs]	(4) [Fe/H]	(5) Grid dimension Mm	(6) resolution nx×ny×nz	(7) opacity bins
d3t50g25mm00	4970	2.5	0	573×573×243	160×160×200	5
d3t50g25mm10	4990	2.5	−1	573×573×245	160×160×200	6
d3t50g25mm20	5020	2.5	−2	584×584×245	160×160×200	6
d3t50g25mm30	5020	2.5	−3	573×573×245	160×160×200	6

Also, model atmospheres used in this Section are similar to those of Collet et al. (2007) what allows for a direct comparison of the results derived using `CO5BOLD` and `STAGGER` model atmospheres. In Sections 4.2 and 4.3 we describe our model atmospheres and spectral line synthesis. In Sect. 4.4 we describe the methodology of comparison of 1D and 3D results present and discuss our results.

4.2 Model atmospheres

In order to study the effects of convection on the molecular line formation we used four hydrodynamical model atmospheres of RGB stars computed with the `CO5BOLD` code (see Sect. 1.1.1). Also, mean ⟨3D⟩ model atmospheres produced with the `Linfor3D` package were utilised (see. Sect. 1.2.2). Parameters of the 3D hydrodynamical and averaged ⟨3D⟩ model atmospheres used in this work are provided in the Table 4.1.

Besides 3D hydrodynamical and averaged ⟨3D⟩ model atmospheres, we used classical 1D model atmospheres that were calculated using the `LHD` code (see, e.g., Caffau et al. 2008, and Sect. 1.1.2). Both 3D and 1D models used in this work shared identical atmospheric parameters (Table 4.1), chemical composition, equation of state, and schemes of radiation transport and opacity binning. Convection in the `LHD` models was treated according to the formalism of the mixing-length theory by Mihalas (1978). The mixing-length parameter used throughout the `LHD` simulations was $\alpha_{\rm MLT} = 1.0$. The temperature stratification of the 3D, averaged ⟨3D⟩ and 1D hydrostatic models at [M/H] = 0.0 and –3.0 are shown in Figures 4.1 and 4.2, respectively.

4.3 Spectral line synthesis

We probe the influence of convection on the formation of spectral lines using fictitious spectral line profiles computed under the assumption of LTE. For these lines, their central wavelengths, excitation potentials, χ, and oscillator strengths,

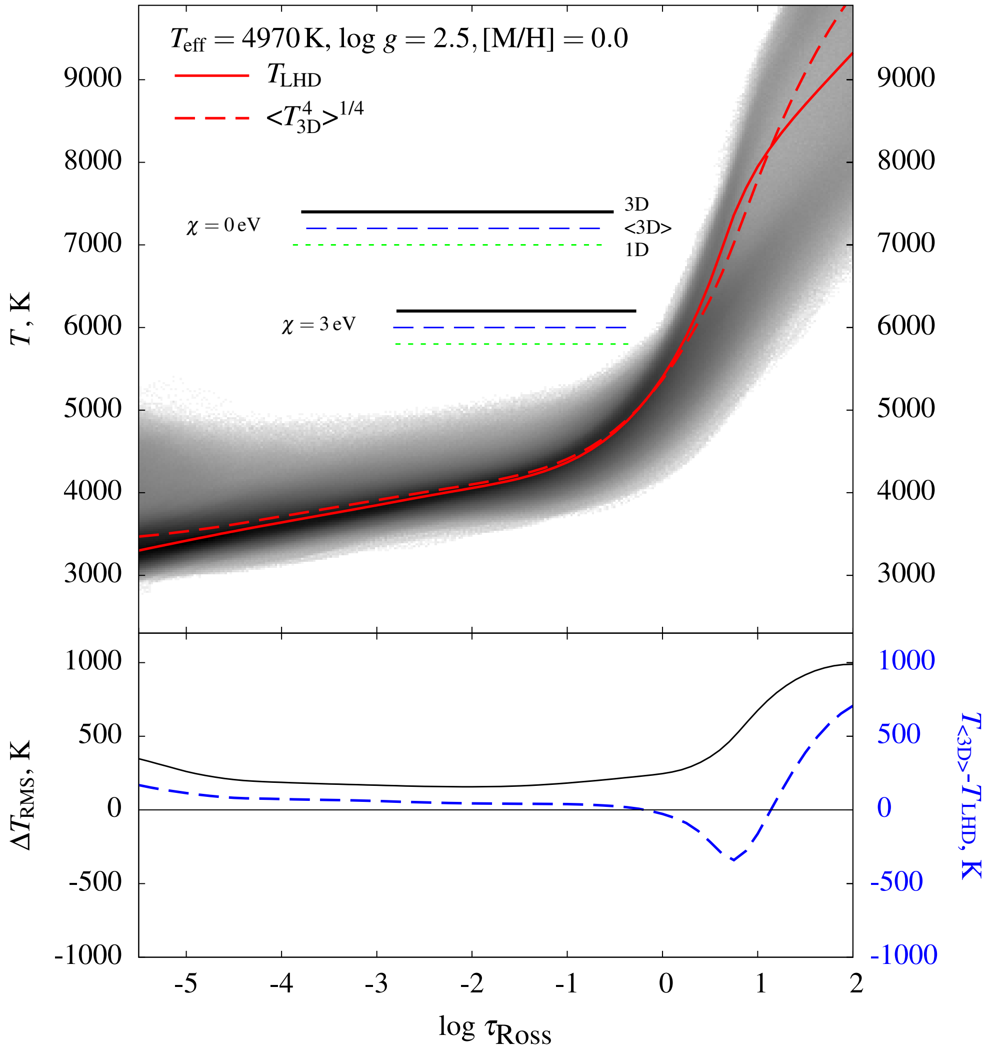

Fig. 4.1. Upper panel: temperature profiles of model atmosphere with $T_{\rm eff}/\log g/$ [M/H] = 4970/2.5/0.0 plotted versus the Rosseland optical depth, $\tau_{\rm Ross}$, and shown for the following model atmospheres: 3D hydrodynamical (density plot), averaged ⟨3D⟩ (dashed line), and 1D hydrostatic (solid line). Horizontal bars mark the approximate location of the CO line formation regions in the 3D hydrodynamical (black), averaged ⟨3D⟩ (blue) and 1D hydrostatic (black) atmosphere models, at λ = 400 nm and χ = 0 and 3 eV (bars mark the regions where the equivalent width, W, of a given spectral line grows from 5% to 95% of its final value). Lower panel: RMS horizontal temperature fluctuations in the 3D hydrodynamical model (solid line); and difference between the temperature profiles of the averaged ⟨3D⟩ and 1D hydrostatic models (dashed line), shown as functions of the Rosseland optical depth..

log gf, were chosen to cover the range of values of real spectral lines. These quantities and the assumption of LTE allow to compute necessary data (population of the ground level, line and continuum opacities, and source functions) required for synthesising a spectral line. Such an approach allows to study the relation between the atomic line parameters and line formation properties in the presence of realistically modelled convection, and has been already applied suc-

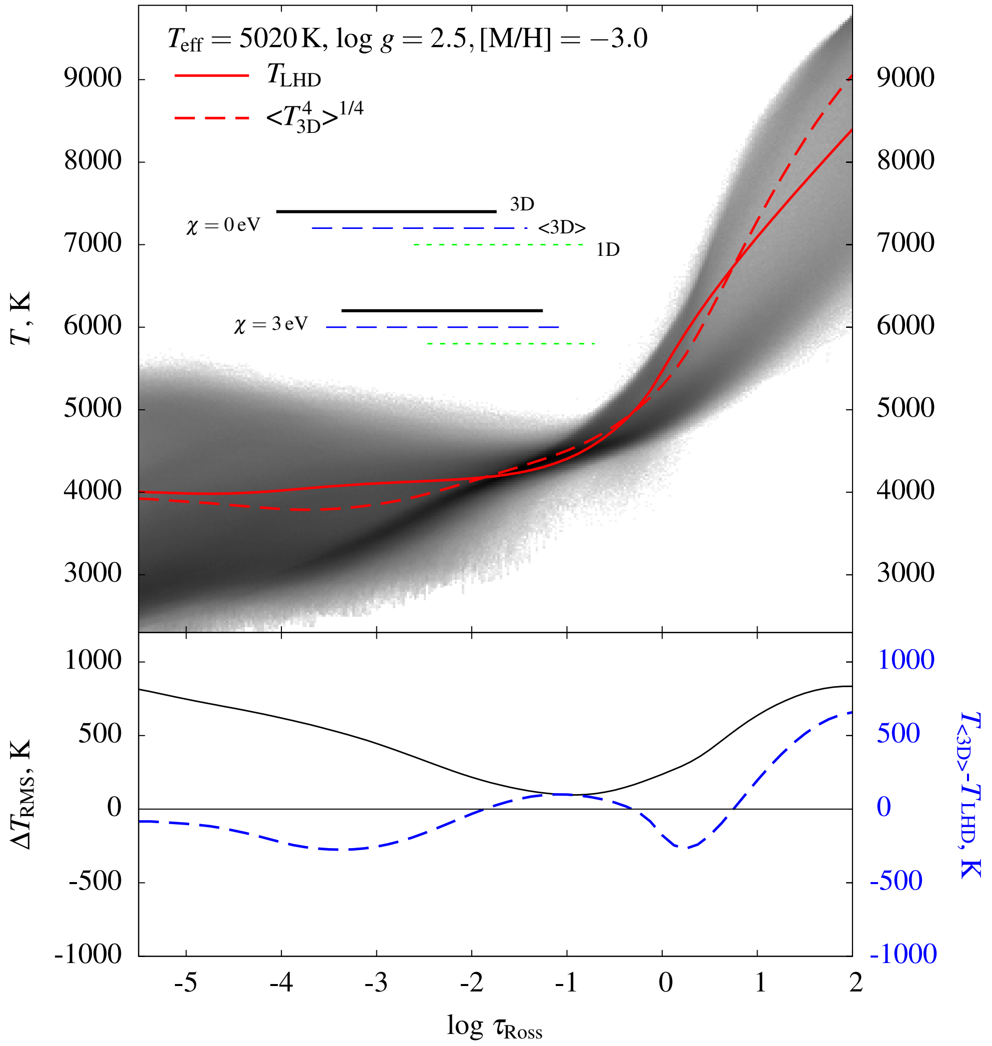

Fig. 4.2. Same as in Fig. 4.1, but for the model atmosphere with $T_{\rm eff}$/ log g/ [M/H] = 5020/2.5/ − 3.0.

cessfully in a number of studies (e.g., Steffen & Holweger 2002; Collet et al. 2007; Kučinskas et al. 2013).

Spectral line synthesis calculations were done using the `Linfor3D` code[1], which solves the radiative transfer equation using the method of long characteristics. In our simulations the radiative intensities were computed for 3 angles in the vertical plane and 4 azimuthal angles. The intensities were summed-up using Gauss-Lobatto scheme in order to obtain disk-integrated flux. The line synthesis calculations covered the Rosseland optical depth range of $\log \tau_{\rm Ross} = -6 \ldots 2$, in steps of $\Delta \log \tau_{\rm Ross} = 0.08$.

In this study, we used weak lines located on the linear part of the curve of growth, with the line equivalent widths $W < 0.5$ pm. Strengths of such lines

---

[1] http://www.aip.de/~mst/linfor3D_main.html

Table 4.2. Dissociation potential (D_0) and wavelength (λ) of the bluest molecular lines studied in this work (see text for details).

	CO	CN	C_2	OH	CH	NH
D_0, eV	11.1	7.8	6.3	4.4	3.5	3.5
λ, nm	400.0	388.3	400.0	313.9	430.8	336.0

should be independent from the variations in microturbulence velocity, $\xi_{\rm mic}$, used in the spectral line synthesis with the averaged $\langle 3D \rangle$ and 1D model atmospheres. Analysis of such lines allows to investigate the influence of 3D hydrodynamical effects on the spectral line formation.

4.4 Influence of convection on the formation of molecular lines

The influence of convection on molecular spectral line formation was studied with the aid of abundance corrections. Abundance correction is defined as a difference in the abundance, ϵ(X), of the chemical element X calculated at a fixed equivalent width between the curves of growth that were computed with the 3D hydrodynamical and 1D hydrostatic model atmospheres. We are mainly interested in 3D–1D abundance corrections, $\Delta_{\rm 3D-1D}$, that represent difference between abundances inferred from the 3D and 1D model atmospheres[2]. If $\Delta_{\rm 3D-1D}$ is negative then it means that 3D model atmosphere predicts stronger lines and lower abundances (and vice versa). Since we also compute synthetic spectra using the averaged $\langle 3D \rangle$ model atmospheres, we also derived two additional abundance corrections, $\Delta_{\rm 3D-\langle 3D \rangle}$ and $\Delta_{\rm \langle 3D \rangle-1D}$. Since the averaged $\langle 3D \rangle$ model atmosphere is one-dimensional and is devoid of information about horizontal inhomogeneities of thermodynamic and hydrodynamical quantities, $\Delta_{\rm 3D-\langle 3D \rangle}$ correction shows the effect of horizontal fluctuations of these quantities in 3D model atmosphere. Also, $\Delta_{\rm \langle 3D \rangle-1D}$ correction measures differences in the abundances due to different temperature profiles in the averaged $\langle 3D \rangle$ and 1D model atmospheres. Since the mean $\langle 3D \rangle$ model atmospheres are obtained by averaging full 3D hydrodynamical model atmospheres which are computed by solving full set of hydrodynamical equations, the $\Delta_{\rm \langle 3D \rangle-1D}$ correction may help to reveal the possible shortcomings of MLT implemented in the 1D model atmospheres.

Abundance corrections were calculated for a number of molecules: CH, CO, C_2, NH, CN, and OH. All of these molecules are important tracers of CNO el-

---

[2] $\Delta_{\rm 3D-1D} \equiv \epsilon({\rm X})_{\rm 3D} - \epsilon({\rm X})_{\rm 1D}$

ements and sometimes are the only abundance tracers in the metal-poor stars where strong atomic lines are lacking. Abundance corrections for molecular lines were calculated at blue, red and near-infrared wavelengths. For the shortest wavelengths, we have chosen the wavelengths of the real molecular bands (see Table 4.2) and, if those were not available, we have used $\lambda = 400$ nm. For the red and near-IR wavelengths, calculations were performed at 850 and 1600 nm. The two shorter wavelengths were chosen to probe the typical blue and red limits of modern optical spectrographs, such as UVES/GIRAFFE@VLT, HIRES@Keck, HDS@SUBARU, while the $\lambda = 16000$ nm approximately coincides with the H-band of near-infrared spectrographs, such as CRIRES@VLT, NIRSPEC@Keck. The two longest wavelengths also coincide with the maximum and minimum absorption of the H^- ion at $\sim$ 850 and $\sim$ 1640 nm, respectively, while at the bluest wavelengths the H^- absorption becomes progressively smaller and opacities from various metals become increasingly more important. The abundance corrections for the molecular lines were computed at four excitation potentials, $\chi = 0$, 1, 2, and 3 eV.

The 3D–1D abundance corrections for molecular lines are shown in Fig. 4.3, 4.4, and 4.5, at the bluest wavelength, 850, and 1600 nm, respectively. In case when real molecular bands were not available at the shortest wavelengths, the abundance corrections were obtained for fictitious spectral lines at $\lambda = 400$ nm. We provide three abundance corrections, $\Delta_{\mathrm{3D}-\langle\mathrm{3D}\rangle}$, $\Delta_{\langle\mathrm{3D}\rangle-\mathrm{1D}}$, and $\Delta_{\mathrm{3D}-\mathrm{1D}}$, plotted versus metallicity at four different excitation potentials, $\chi = 0$, 1, 2, and 3 eV.

3D–1D abundance corrections for the molecules are strongly dependent on the metal content in the model atmosphere and are largest at the lowest metallicities. While for the majority of molecules the total abundance correction, $\Delta_{\mathrm{3D}-\mathrm{1D}}$, generally does not exceed –0.5 dex at $[\mathrm{M/H}] = -3.0$, in case of CO it reaches to –1.5 dex. The large total abundance corrections are mostly due to the large $\Delta_{\mathrm{3D}-\langle\mathrm{3D}\rangle}$ corrections, which indicates the importance of horizontal temperature fluctuations in the formation of molecular lines. The contribution due to differences in the average 3D and 1D temperature profiles, however, is also non-negligible and may reach –0.5 dex in case of model atmospheres characterized by the lowest metallicity.

The trends in the abundance corrections for molecules seen in Fig. 4.3–4.5 are determined by a subtle interplay of a number of different factors. In cases studied here, horizontal temperature fluctuations play an essential role in defining abundance corrections for the molecules. In the first place, they are larger in the

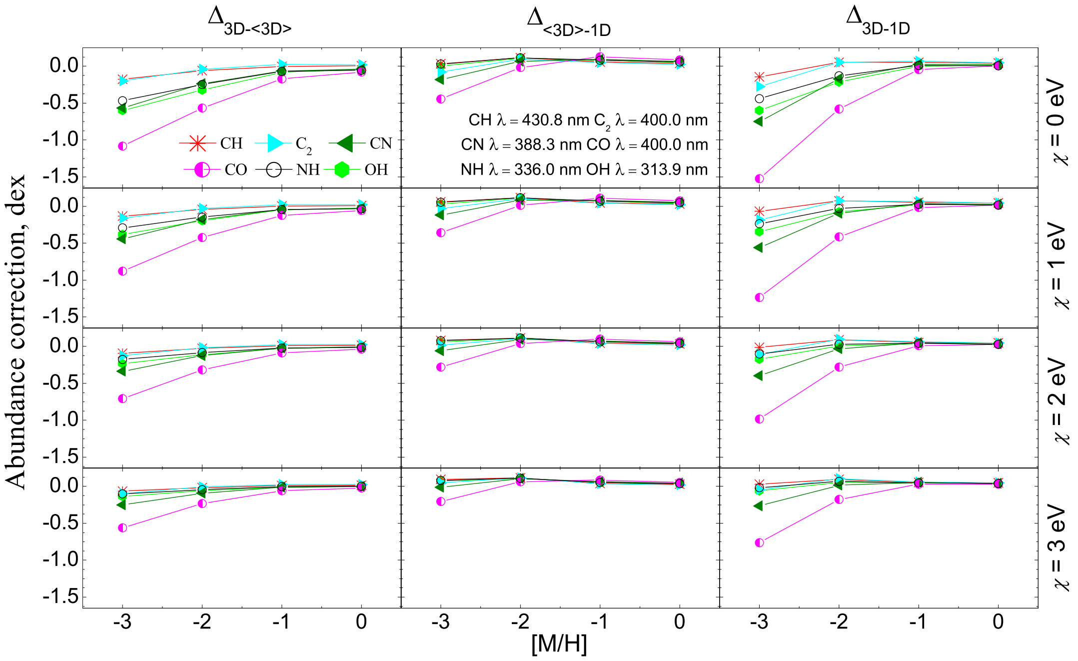

Fig. 4.3. Abundance corrections of molecular spectral lines plotted versus computed at the bluest wavelengths (see the middle panel in the top row for the wavelength value of a given molecular species) and plotted versus model metallicity: $\Delta_{\rm 3D-\langle 3D\rangle}$ (left column), $\Delta_{\rm \langle 3D\rangle-1D}$ (middle column), and $\Delta_{\rm 3D-1D}$ (right column). Corrections in each row were calculated at different excitation potentials, as indicated on the right side of each row.

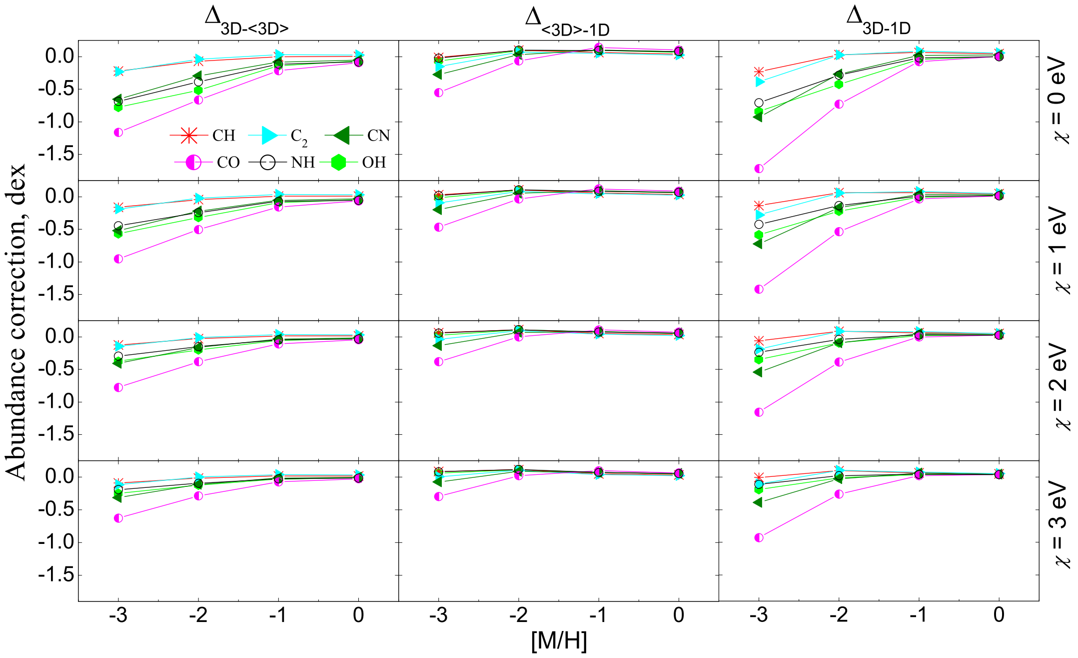

Fig. 4.4. The same as in Fig. 4.3 but at λ = 850 nm.

3D hydrodynamical models at lower metallicity (cf. Fig. 4.1 and Fig. 4.2), which leads to the largest fluctuations in molecular number densities and line opacity in the lowest metallicity models. Also, in a model of a given metallicity differ-

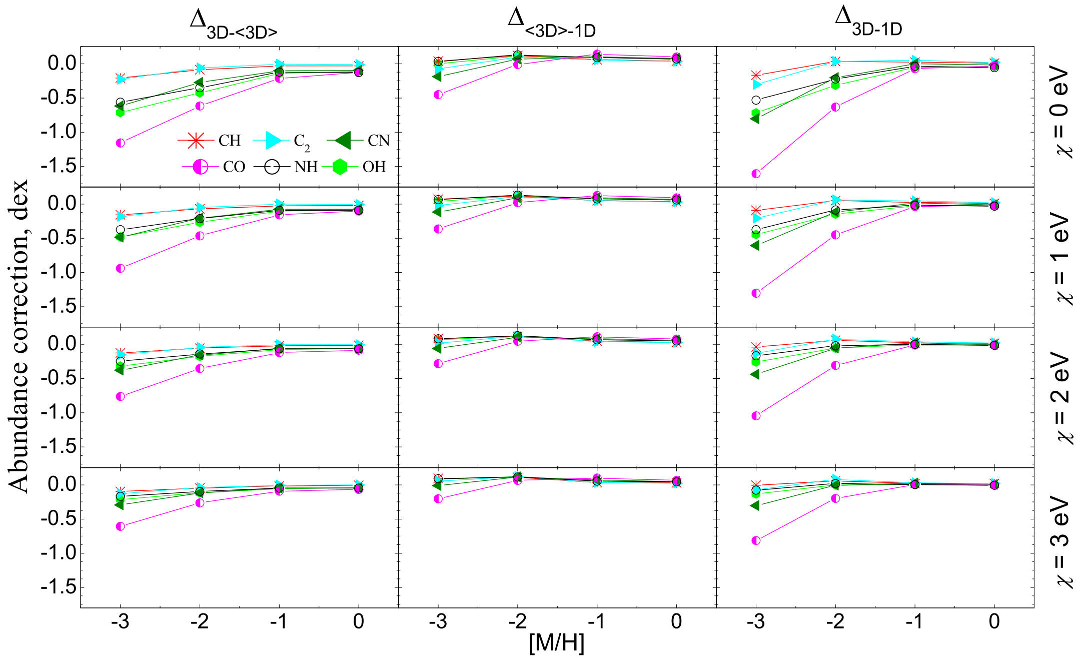

Fig. 4.5. The same as in Fig. 4.3 but at $\lambda = 1600$ nm

ent molecules form at different optical depths. These optical depths are characterized by different amplitudes of the horizontal temperature fluctuations. For example, in the model atmosphere with [M/H] = −3.0, CO formation occupies the outermost range in terms of Rosseland optical depth amongst all molecules studied here (Fig. 4.6). Consequently, its lines form in the atmospheric layers characterized by the largest horizontal temperature fluctuations, i.e., in comparison to those in the layers where other molecules form. The fluctuations of the line opacity are therefore largest in the case of CO in the 3D hydrodynamical model at [M/H] = −3.0, which partly explains the large abundance corrections for CO. However, further factors are important.

The number density of molecules per unit mass (calculated as $X_i = N_i/\rho$, here ρ is the mass density) can be computed using the following Saha-like equation (see, e.g., Kučinskas et al. 2013)

$$X_{AB} = \rho\ Q_{AB}(T)\,\frac{X_A}{U_A(T)}\,\frac{X_B}{U_B(T)}\left(\frac{h^2}{2\pi\, m_{AB}\, kT}\right)^{3/2}\ \mathrm{e}^{\,D_0/kT} \tag{4.1}$$

where Q_{AB} is partition function of the molecule AB, X_A and X_B are number densities per unit mass of the constituent species A and B, with their partition functions U_A and U_B, respectively, mass of the molecule m_{AB}, its dissociation energy D_0, and temperature, T.

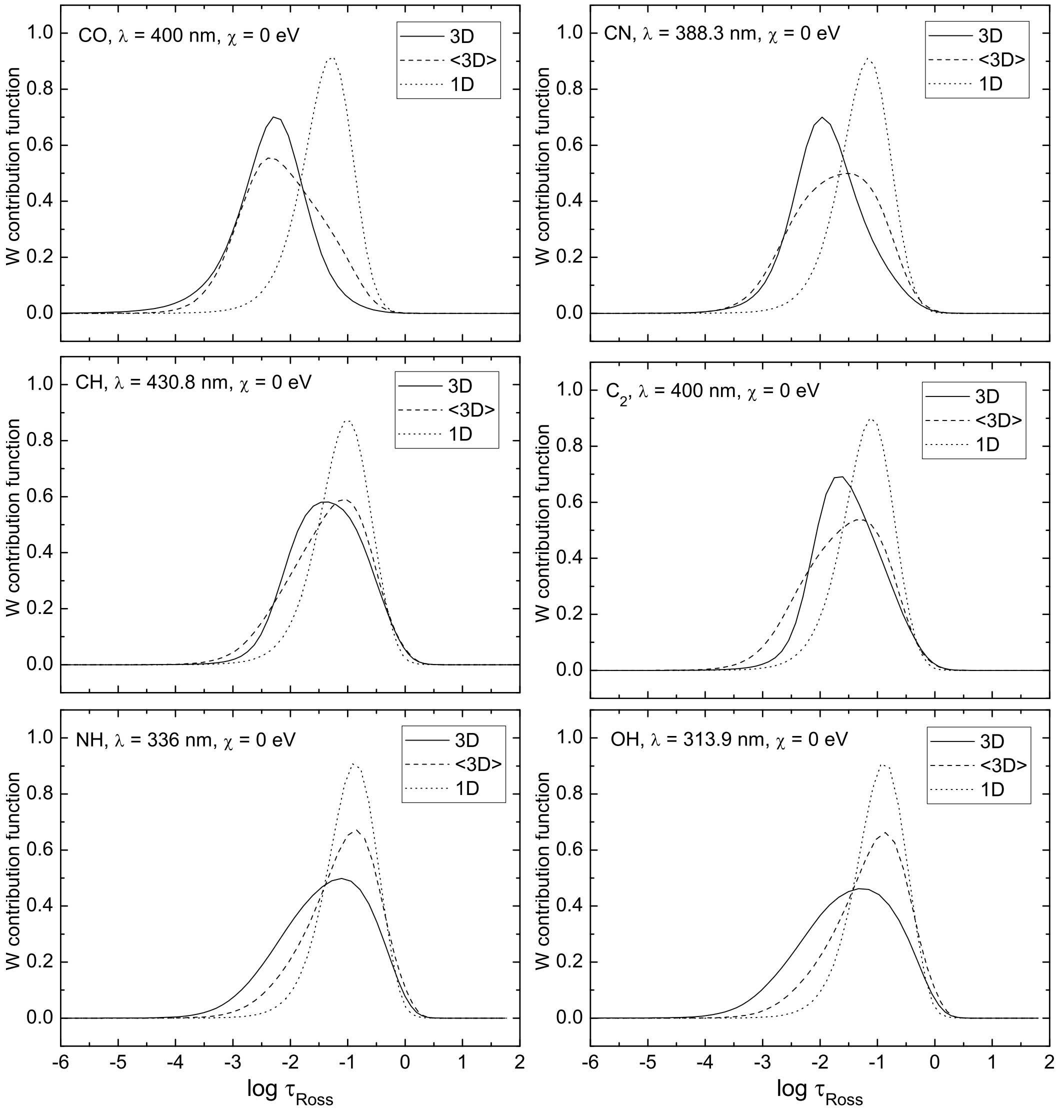

Fig. 4.6. Equivalent width contribution function (flux) of a weak ($W \leq 0.5$ pm) artificial molecular lines of CO, CN, CH, C_2, NH, OH (top left to bottom right) with lower level excitation potential $\chi = 0$ eV in the full 3D hydrodynamical , averaged ⟨3D⟩, and 1D hydrostatic model atmospheres ([M/H] = −3.0).

From Eq. (4.1) one may expect different temperature sensitivity of the number densities of different molecules. Indeed, this is clearly seen in Fig. 4.7 where we show normalized number densities of CO, CN, CH, C_2, NH and OH in the 3D hydrodynamical model atmosphere ([M/H] = −3.0) at different levels of Rosseland optical depths, plotted versus inverse temperature, $\theta = 5040/T$. It is obvious that CO is significantly more sensitive to changes in T than the other molecules are, essentially due to the high dissociation energy of CO ($D_0 = 11.1$ eV) that enters into the exponent of Eq. (4.1). Since the line opacity is directly proportional to X_{AB}, larger fluctuations of the number densities should lead to larger fluctuations and larger non-linearities in the line opacities, and thus to larger abundance

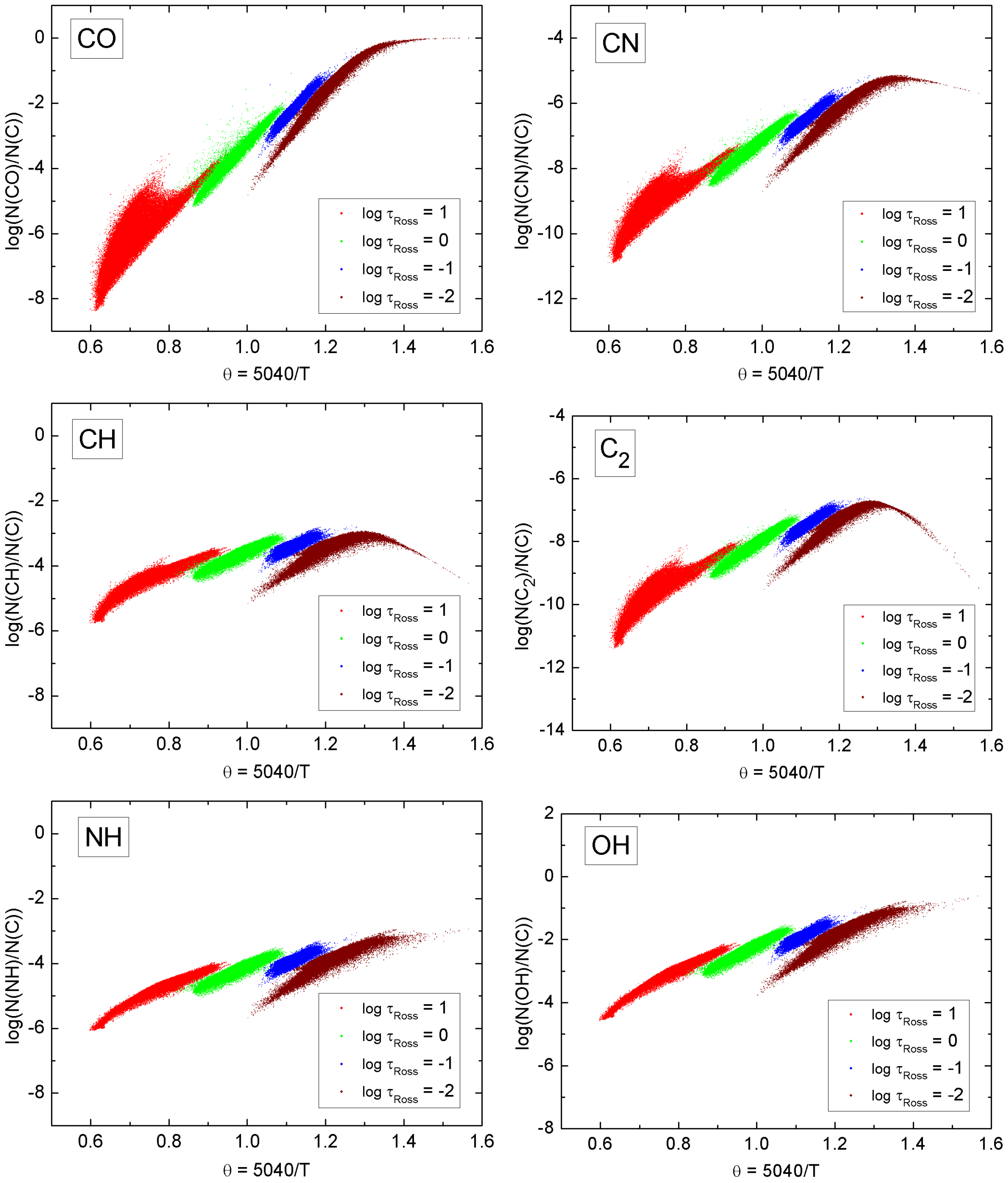

Fig. 4.7. Normalized number densities of CO, CN, CH, C_2, NH, OH (top left to bottom right) in the 3D hydrodynamical model atmosphere ($[M/H] = -3.0$) plotted at different levels of Rosseland optical depth (identified by color) as a function of inverse temperature, $\theta = 5040/T$.

corrections. This is basically what one sees in case of CO: the largest range of fluctuations in the case of CO leads to the largest abundance corrections seen amongst all molecules investigated here.

Other carbon-bearing molecules show somewhat different behavior. For example, CH ($D_0 = 3.5$ eV) and C_2 ($D_0 = 6.3$ eV) show the smallest (least negative) 3D–1D abundance corrections. Unexpectedly, the corrections for these two molecules are almost identical, although their dissociation energies are rather different. The explanation for this unexpected behavior is related to the fact that the temperature dependence of the number densities at the optical depth $\tau_{\mathrm{Ross}} = -2$ changes sign, both for CH and C_2 (see middle panels of Fig. 4.7). At these optical depths, almost all carbon is locked up in CO and an increase in temperature (i.e., decrease in θ) leads to the destruction of CO, and in turn, to a larger concentration of atomic carbon that enables an enhanced formation of carbon-bearing molecules. High concentrations of CO at $\tau_{\mathrm{Ross}} = -2$ prohibit high number densities of other carbon-bearing molecules, thus strengthening their spectral lines and placing a higher limit on the magnitude of their 3D–1D abundance corrections. Carbon-free molecules do not show this unexpected behavior at low temperature (see lower panels of Fig. 4.7) where their abundance corrections scale with their individual dissociation potentials.

Chapter 5

Oxygen abundance in the metal-poor giant HD 122563 determined using OH UV lines

5.1 Introduction

Since the amount of oxygen produced in a given stellar population depends on the details of its star formation history (such as initial mass function and star formation rate), the knowledge of the oxygen abundance in the oldest (i.e., metal-poor) Galactic stars may allow us to put stricter constraints on the possible scenarios of early Galactic evolution. However, measurements of oxygen abundance in the metal-poor stars are difficult, for several reasons. First, only a few spectral lines of atomic oxygen are available for oxygen diagnostics in the metal-poor ($[\mathrm{Fe/H}] < -2$) stars: the forbidden [O I] 630 nm line in giants, and the permitted O I 777 nm triplet in main sequence stars and subgiants. Therefore, different spectral lines are used to study different types of stars. Besides, all atomic oxygen lines become very weak at these low metallicities - and thus difficult to measure. Because of these reasons, OH vibrational-rotational and pure rotational lines in the infrared ($\sim 1500 - 2100$ nm) and electronic lines in the ultraviolet ($\sim 310 - 330$ nm) are often used to probe the oxygen abundance in the metal-poor stars. However, oxygen abundances obtained from OH lines typically show large line-to-line scatter and/or trends with the line equivalent width and/or excitation potential (see, e.g., Meléndez & Barbuy 2002; Barbuy et al. 2003; Aoki 2015). Finally, oxygen abundances obtained using different indicators are frequently inconsistent. For example, abundances determined using OH lines may be up to ~ 0.4 dex higher than those obtained using the [O I] line (see, e.g., Dobrovolskas et al. 2015, and references therein). All these factors lead to large systematic uncertainties in the derived oxygen abundances. As a consequence, our current knowledge about the oxygen trends at low metallicities is still incomplete: some authors claim that the [O/Fe] ratio increases towards the lowest metallicities and reaches $[\mathrm{O/Fe}] \approx 1.0$ at $[\mathrm{Fe/H}] \approx -3$ (e.g., Israelian et al. 2001), while others find that there is a plateau around $[\mathrm{O/Fe}] \approx 0.4 - 0.7$ at $[\mathrm{Fe/H}] \approx -2 \ldots -3$ (e.g., Cayrel et al. 2004; Amarsi et al. 2015).

It is possible that inconsistencies in the oxygen abundances obtained using different spectral indicators are partly caused by insufficient physical realism of the classical abundance analysis techniques which rely on 1D hydrostatic model atmospheres. It is well known that oxygen lines are sensitive to 3D hydrodynamical effects, such as convection and/or shock waves (e.g., Collet et al. 2007; Kučinskas et al. 2013; Dobrovolskas et al. 2013). However, these effects are not properly taken into account with the classical approach. Although the influence of 3D hydrodynamical effects on the spectral line strengths is different for different lines and depends on the structure of a given stellar atmosphere (which, in turn, is defined by the atmospheric parameters of a given star), 3D–1D differences in the oxygen abundances can reach or even exceed ~ 0.4 dex (Collet et al. 2007; Dobrovolskas et al. 2013). Such differences are similar in their size to the discrepancies in oxygen abundances obtained using different indicators described above and therefore may point to inadequacies in 1D model atmospheres as a possible culprit[1].

Authors of Dobrovolskas et al. (2015) therefore investigated whether 3D hydrodynamical model atmospheres may help to solve these problems. In that study the authors determined 3D LTE oxygen abundances in four metal-poor red giants using infrared (IR) vibrational-rotational OH lines. It was found that in the 3D LTE analysis the difference between the average oxygen abundances obtained in the four metal-poor giants using OH IR lines and [O I] 630 nm line was 0.09 dex, down from 0.34 dex determined in 1D LTE[2]. Unfortunately, it is still unclear whether similar improvements could be expected in case of OH lines that are located in the ultraviolet (UV) part of the spectrum. To our knowledge, the only studies where OH UV lines were investigated using 3D hydrodynamical model atmospheres were carried out by Asplund & García Pérez (2001), who focused on dwarfs, González Hernández et al. (2010); Behara et al. (2010) where the authors targeted a sample of metal poor subgiant stars; and by Bessell et al. (2015) who studied the extremely metal-poor halo subgiant SMSS J031300.36-670839.3 (though the atmospheric parameters of this star, $T_{\mathrm{eff}} = 5125\,\mathrm{K}$ and $\log g = 2.3$, are in fact more similar to those of a giant) and Collet et al. (2006), who analysed a giant and a dwarf. Other studies of red giant stars are still lacking.

---

[1] Although non-local thermodynamic equilibrium (NLTE) effects may play an important role here too, their study is beyond the scope of the present work.

[2] It is known that the forbidden [O I] line is insensitive to 3D hydrodynamical and NLTE effects, therefore oxygen abundances determined using this line offer a convenient reference point (see, e.g., Dobrovolskas et al. 2015, and references therein).

In this Chapter we therefore extend the previous work and focus on OH UV lines which we use to determine 1D LTE and 3D LTE oxygen abundances in the well-studied metal-poor giant HD 122563. The main goals of this work are: (a) to better understand the role of 3D hydrodynamical effects/convection in the formation of OH UV lines in the atmospheres of metal-poor red giant stars; (b) to find out whether the analysis of OH UV lines with 3D hydrodynamical model atmospheres may provide oxygen abundances that are more precise and reliable than those obtainable in 1D LTE analysis; and (c) to determine whether the use of 3D hydrodynamical model atmospheres may help to reconcile abundances determined using OH UV, OH IR, and [O I] lines. Therefore, ultimately, we aim to provide a prescription for future studies of oxygen abundances based on 3D LTE analysis of OH UV lines that, besides of being stronger and more numerous than atomic oxygen lines, frequently can be the only available indicators of oxygen abundance in the metal-poor red giants.

The Chapter is structured as follows: we describe our target object, the metal-poor red giant HD 122563 and the spectroscopic material are described in Sect. 5.2, the 1D hydrostatic and 3D hydrodynamical model atmospheres are outlined in Sect. 5.3 while the 1D and 3D abundance analysis techniques are presented in Sect. 5.4. The obtained results are presented and discussed in Sect. 5.5.

5.2 Target star and observations

In this work we focus on a well-studied metal-poor red giant HD 122563. This bright ($V = 6.2$) halo star has been thoroughly investigated in a number of studies and has reliably determined atmospheric parameters, as well as abundant high quality spectroscopic observations. All this makes HD 122563 a suitable target for the study of OH UV line formation in the atmospheres of metal-poor red giant stars.

After assessing available determinations of the atmospheric parameters of HD 122563, we have chosen to use $T_{\rm eff} = 4600\,{\rm K}$ and $\log g = 1.60$, as determined using precise interferometric measurements by Creevey et al. (2012). The metallicity, $[{\rm Fe/H}] = -2.60$, was adopted from Mashonkina et al. (2011). This result was obtained using 1D NLTE abundance analysis techniques and the model atmosphere characterized by the atmospheric parameters identical to those used in our study (more recently Jofré et al. 2014 has obtained a similar value of $[{\rm Fe/H}] = -2.64$ which was determined in a careful 1D NLTE analysis of Fe I and Fe II lines in HD 122563).

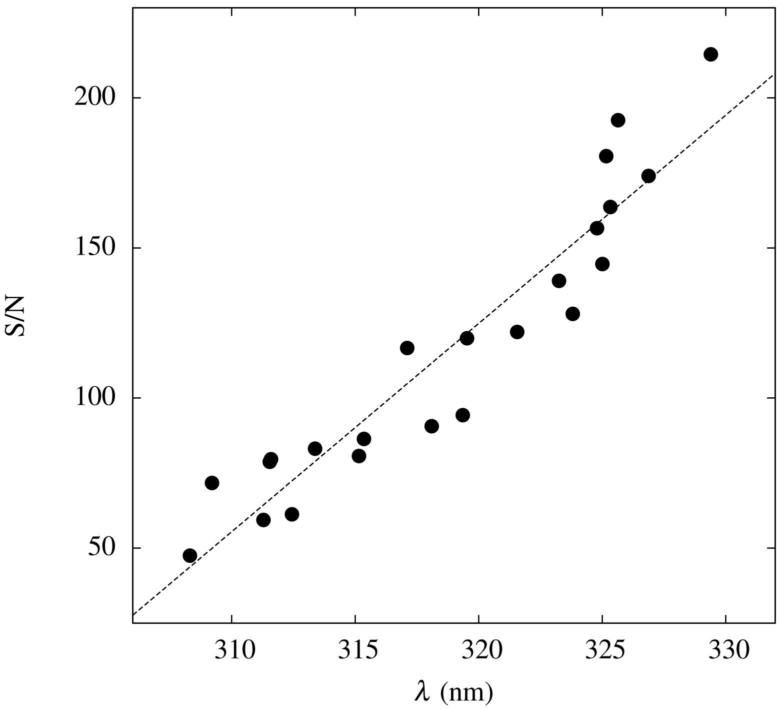

Fig. 5.1. Signal-to-noise ratio in the investigated spectral region. The dashed line indicates a linear fit to the data.

We used a high-resolution (R = 60 000) spectrum of HD 122563 that was obtained with the UVES spectrograph mounted on the ESO VLT UT2 telescope. A reduced spectrum was taken from the ESO UVES Paranal Observatory Project (UVES-POP) archive (program ID 266.D-5655; Bagnulo et al. 2003). The UVES-POP spectrum of HD 122563 was obtained using both the blue and red arms of the spectrograph, and covered a total spectral range of 304 – 1040 nm. In our study we focused only on the UV part of the spectrum where OH UV lines used for the oxygen abundance analysis were located, i.e., the region between 308 – 330 nm.

Further investigation required an estimate of error $\sigma_{\rm flux}$ (Sect. 5.4.1), which is an inverse of the signal-to-noise ratio (S/N). This quantity was obtained as a standard deviation of flux values in a blend-free (continuum) spectral regions. Measurements were done in the entire investigated spectral range and 10-20 wavelength points were used for each measurement of $\sigma_{\rm flux}$. The results are shown in Fig. 5.1. A rather tight relationship between S/N and λ was found and for further applications it was approximated with a linear fit.

5.3 Model atmospheres

Three types of model atmospheres were used in this work:

- a 1D hydrostatic `ATLAS9` model atmosphere;
- a 1D hydrostatic model atmosphere computed using the `LHD` code (Caffau et al. 2008);
- a 3D hydrodynamic model atmosphere computed with the $\mathtt{CO}^5\mathtt{BOLD}$ package (Freytag et al. 2012).

Both 1D model atmospheres were identical to those used in Dobrovolskas et al. (2015) while our 3D model atmosphere had the same atmospheric parameters but was more extended in the vertical direction than the one used in Dobrovolskas et al. (2015, see below). The atmospheric parameters of the model atmospheres are listed in Table 5.1.

The three model atmospheres were computed having slightly different purposes in mind. The classical `ATLAS9` model atmosphere was used to determine oxygen abundances from the OH UV lines in the observed spectrum of HD 122563 (see Sect. 5.4.1). The model atmosphere was computed using the Linux port of the `ATLAS9` code (Sbordone et al. 2004; Sbordone 2005). Model computations were done with the overshooting switched off and the mixing length parameter set to $\alpha_{\rm MLT} = 1.25$. The radiative transfer included continuum scattering and was solved by adopting NEWODF opacity distribution functions (ODFs) that were computed with metallicity [Fe/H] = −2.5 and microturbulence velocity of $\xi = 2\,{\rm km\,s^{-1}}$ (Castelli & Kurucz 2003).

The 1D hydrostatic `LHD` and 3D hydrodynamical $\mathtt{CO}^5\mathtt{BOLD}$ model atmospheres were used for computing 3D–1D LTE abundance corrections which were further used to determine 3D LTE oxygen abundances (see Sect. 5.4.2). The abundance corrections were also used to assess the influence of convection on the formation of OH UV lines (Sect. 5.5). The `LHD` and $\mathtt{CO}^5\mathtt{BOLD}$ model atmospheres

Table 5.1. Atmospheric parameters of the model atmospheres used in this work. In case of the 3D hydrodynamical model atmosphere temporal RMS of the $T_{\rm eff}$ is also provided.

Model atmosphere	$T_{\rm eff}$ K	$\log g$ [cgs]	[Fe/H] dex
`ATLAS9` (1D)	4600	1.6	−2.60
`LHD` (1D)	4600	1.6	−2.50
$\mathtt{CO}^5\mathtt{BOLD}$(3D)	4597 ± 7	1.6	−2.50

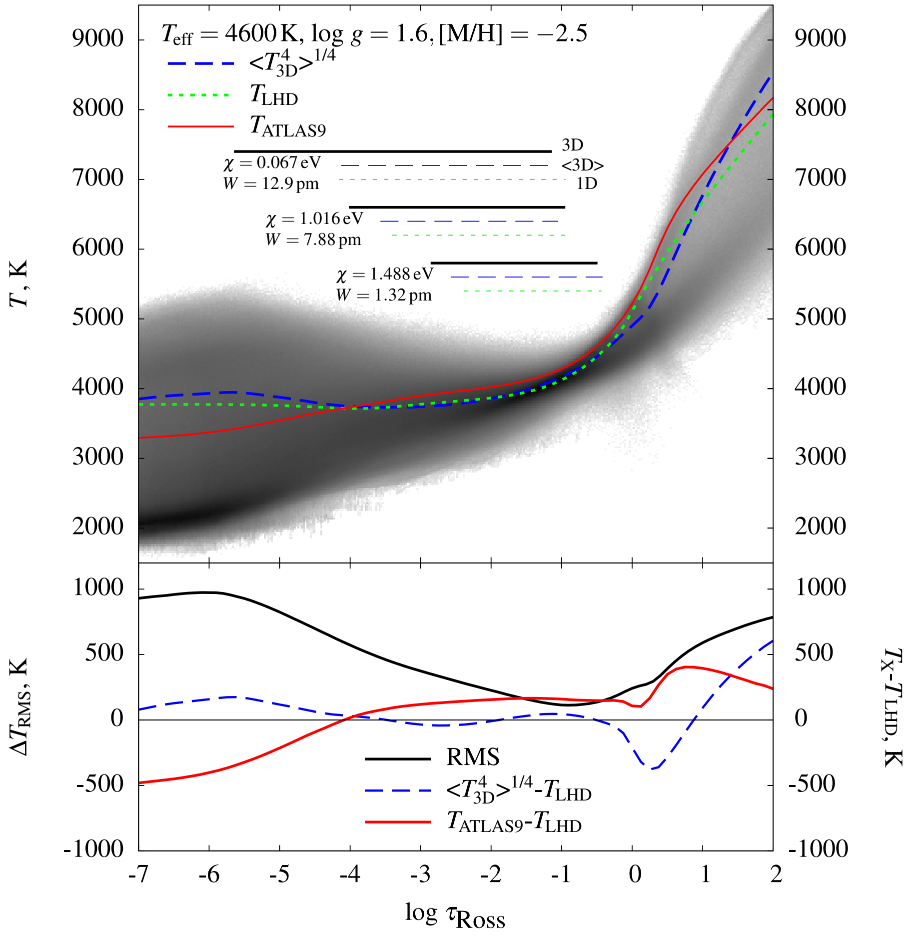

Fig. 5.2. Top: temperature structure of the 3D hydrodynamical (grey scale map of the logarithmic temperature probability density), average $\langle 3D \rangle$ (blue dashed line), and 1D LHD (green dotted line) model atmospheres of HD 122563. For comparison, we also show the temperature profile of the ATLAS9 model atmosphere (red solid line). Horizontal bars indicate the optical depth intervals where 90% of the equivalent width (i.e., between 5% and 95%) of three representative OH lines is formed in the 3D hydrodynamical (black solid bar), average $\langle 3D \rangle$ (blue dashed bar), and 1D LHD (green dotted bar) model atmospheres (spectral line parameters are given next to each set of horizontal bars). Bottom: RMS value of horizontal temperature fluctuations in the 3D model (black solid line, $\Delta T_{\rm RMS}$), temperature difference between the average $\langle 3D \rangle$ and 1D models, $\left\langle T_{\rm 3D}^{4} \right\rangle^{1/4} - T_{\rm LHD}$ (blue dashed line), and temperature difference between the ATLAS9 and LHD model atmospheres (red solid line).

were computed using identical atmospheric parameters, chemical composition, equation of state, opacities, and radiative transfer scheme. Our goal therefore was to minimize the differences between the LHD and CO^{5}BOLD models so that the role of convection in the OH UV line formation could be assessed by comparing the differences in the atmospheric structures and observable properties of the two model atmospheres (see Sect. 5.5).

We stress that `ATLAS9` model atmospheres are better suited for 1D LTE abundance analysis than `LHD` models, because of the more realistic radiative transfer scheme based on opacity distribution functions. On the other hand, `LHD` models are better suited for assessing the influence of convection on the spectral line formation which can be done using 3D–1D abundance corrections, because `LHD` and $\texttt{CO}^5\texttt{BOLD}$ model atmospheres are computed employing identical radiative transfer schemes and microphysics.

The 3D hydrodynamical $\texttt{CO}^5\texttt{BOLD}$ simulations were performed following the procedures described in our earlier studies (see, e.g., Ludwig & Kučinskas 2012; Kučinskas et al. 2013; Dobrovolskas et al. 2013). The model atmosphere was computed using a "box-in-a-star" setup and Cartesian grid of $160 \times 160 \times 300$ points ($3.85 \times 3.85 \times 3.78$ Gm) in $x \times y \times z$, respectively (z denotes the vertical direction). The radiative transfer was solved under the assumption of LTE, scattering was treated as true absorption. `MARCS` opacities were grouped into six bins following the methodology described in Nordlund (1982); Ludwig et al. (1994); Vögler et al. (2004). The model atmosphere was computed using solar-scaled chemical composition, with the α-element abundances enhanced by $[\alpha/\mathrm{Fe}] = +0.4$ dex (see Dobrovolskas et al. 2013, for details). The simulation box covered the Rosseland optical depth range of $-11 \lesssim \log \tau_{\mathrm{Ross}} \lesssim 9$.

Our 3D hydrodynamical model atmosphere was more extended than the one used in Dobrovolskas et al. (2015) which had the outer boundary set at $\log \tau_{\mathrm{Ross}} \approx -6.5$. The larger vertical extension in our case was needed to accommodate the formation of strong OH UV lines since in the most extreme cases it was extending to $\log \tau_{\mathrm{Ross}} \approx -7$ (one of such extreme examples is shown in Fig. 5.9, left panel; see Sect. 5.5.2 for details).

The $\texttt{CO}^5\texttt{BOLD}$ model simulation run covered a span of ~ 10 convective turn-over times as measured by the Brunt-Vaiasälä timescale (see Ludwig & Kučinskas 2012, for details). For further analysis, we have selected a sub-sample of 20 representative snapshots (i.e., 3D model structures computed at different instants in time). The snapshots were chosen by ensuring that the average thermodynamic and hydrodynamical properties of the 20-snapshot sub-sample and those of the entire simulation run would be as similar as possible (see Ludwig & Kučinskas 2012, for details).

As in our previous work, we also used an average $\langle 3\mathrm{D} \rangle$ $\texttt{CO}^5\texttt{BOLD}$ model atmosphere. It was obtained by averaging the fourth moment of temperature on surfaces of equal Rosseland optical depth in the 20-snapshot sub-sample. This model atmosphere was used to evaluate the influence of temperature fluctuations on the formation of OH UV lines (see Sect. 5.4.2 below).

The 1D hydrostatic `LHD` model atmosphere was computed using the `LHD` model atmosphere package, by utilizing the same atmospheric parameters, equation of state, opacities, and chemical composition as used in the computation of the 3D hydrodynamical $\mathtt{CO}^5\mathtt{BOLD}$ model atmosphere. The convective energy transport in the `LHD` model was treated using mixing-length theory, with a mixing-length parameter of $\alpha_{\mathrm{MLT}} = 1.0$.

Temperature profiles of the 3D hydrodynamical, average ⟨3D⟩, and 1D model atmospheres used in this work are shown in Fig. 5.2.

5.4 Oxygen abundance in HD 122563 from OH UV lines

The oxygen abundance determination in HD 122563 was carried out in several steps. First, 1D LTE oxygen abundances were determined from the individual OH UV lines in the observed spectrum of HD 122563, by using the `ATLAS9` model atmosphere and synthetic line profiles computed with the `SYNTHE` package (Sect. 5.4.1). Next, we used the `Linfor3D` spectral synthesis package together with the `LHD` and $\mathtt{CO}^5\mathtt{BOLD}$ model atmospheres to compute 1D LTE and 3D LTE curves of growth (COGs) for each OH UV line. The COGs were used to determine 3D–1D abundance corrections, $\Delta_{\mathrm{3D\ LTE-1D\ LTE}}$ (Sect. 5.4.2). Finally, the 3D LTE abundances were computed by adding 3D–1D abundance corrections to the 1D LTE oxygen abundances determined using individual OH UV lines. The details of these procedures are summarized in the sections below.

5.4.1 Determination of 1D LTE oxygen abundances

We determined 1D LTE oxygen abundances by fitting theoretical line profiles to OH UV lines in the observed UVES spectrum of HD 122563.

The list of OH UV lines used in our analysis is provided in the Table B.1. When selecting lines for the abundance analysis we tried to make sure that they are sufficiently strong (but not saturated) and free from severe blends, so that a reliable determination of oxygen abundances was possible. Nevertheless, nearly all lines in the list are blended, some of them strongly. Therefore, we divided them into three categories according to their quality:

- A-class lines: strong and weakly blended: 3 lines;
- B-class lines: strong and moderately blended: 23 lines;
- C-class lines: weak or significantly blended: 45 lines.

Obviously, the most reliable oxygen abundances were determined using lines of classes A and B which constitute ∼35% of all lines used in the abundance analysis.

Since the spectral region of interest is severely affected by strong line blends, it makes it difficult to choose an accurate continuum level in the observed spectrum of HD 122563. We therefore determined the continuum interactively, by comparing the observed spectrum with the synthetic 1D LTE spectrum computed using the `SYNTHE` spectral synthesis package, by trying to find the best match between the two types of spectra. Obviously, the lack of accuracy of the continuum placement had an impact on the derived oxygen abundances; this issue is further discussed in Sect 5.4.3.

Theoretical profiles of OH UV lines were computed with the `SYNTHE` package in the implementation of Sbordone et al. (2004); Sbordone (2005), using the 1D `ATLAS9` model atmosphere of HD 122563 computed as described in Sect 5.3. The `SYNTHE` calculations included a proper treatment of continuum scattering. For the majority of OH UV lines, atomic line parameters were taken from Aoki (2015). Additionally, we also used data from Israelian et al. (1998), García Pérez et al. (2006), and Kurucz line lists (see Table B.1). The Kurucz atomic and molecular line lists (Castelli & Kurucz 2004) were used for computing spectral line profiles of all other chemical species. In the spectral synthesis computations we used a depth-independent microturbulence velocity of $\xi_{\rm mic} = 2.0$ km/s taken from Spite et al. (2005). Abundances of chemical elements other than oxygen were not determined in our analysis, despite the fact that lines of these elements were sometimes blending with OH UV lines. Instead, we used a solar-scaled chemical composition with constant $[\alpha/{\rm Fe}] = +0.4$ enhancement in the abundances of all α-elements, in accordance with the results of Barbuy et al. (2003). All synthetic line profiles were convolved with a Gaussian profile characterized by the broadening velocity, $v_{\rm brd}$, which accounted for the cumulative effect of macroturbulence, stellar rotation, and instrumental broadening.

Apart from the atomic parameters that were different for each OH UV line (line wavelength, oscillator strength, line excitation potential) and those parameters that were identical for all lines (e.g., microturbulence velocity), synthetic 1D LTE profiles of individual OH UV lines were shaped by two variables – the oxygen abundance, A(O), and broadening velocity, $v_{\rm brd}$. These parameters had to be determined simultaneously, by fitting theoretical to the observed line profiles. During the fitting procedure, we also determined an arbitrary wavelength shift between the observed and synthetic spectra, $\Delta\lambda$, in order to compensate for various wavelength-related shifts (e.g., those caused by wavelength calibration errors, imprecise spectral line wavelengths, convective wavelength shifts). All three fitting parameters – $\Delta\lambda$, $v_{\rm brd}$, and A(O) – were determined by minimizing χ^2 residuals between the observed and synthetic line profiles (see below). For this, we computed a grid of synthetic 1D LTE OH UV line profiles which covered a range in oxygen abundances and line broadening velocities of $5.60 < {\rm A(O)} < 6.80$ and $5.5 < v_{\rm brd} < 11.0$ km/s in steps of 0.1 dex and 0.5 km/s, respectively. Tests made with finer grids have shown that the spacing of our grid was sufficient to limit the error in the oxygen abundance due to the finite step size to ~0.005 dex. This is because during the fitting procedure our grid was further interpolated to obtain better precision in the determined abundances (see below).

During the fitting of the theoretical to the observed line profiles we therefore first determined $\Delta\lambda$, $v_{\rm brd}$, and A(O). This was done by comparing synthetic and observed fluxes, $F_{\rm syn}$ and $F_{\rm obs}$, respectively, for each individual line in our OH UV line list. The wavelength interval for the fitting of $F_{\rm obs}$ and $F_{\rm syn}$ was tailored specifically in case of each OH UV line, in order to avoid blends, neighbouring lines of other elements, artefacts (see Fig. 5.3 and Sect. 5.5.1 below). Then, for each spectral line i we used a number of trial values of $\Delta\lambda^j$ and for each wavelength point m in the line profile i and each value of ${v_{\rm brd}}^k$ and ${\rm A(O)}^l$ in our grid of synthetic line profiles we computed an array of χ^2 values according to

$$\chi_i^2(\Delta\lambda^j, {v_{\rm brd}}^k, {\rm A(O)}^l) = \sum_{m=1}^{N^i} \frac{({F_{\rm obs}}^m - {F_{\rm syn}}^{m,j,k,l})^2}{\sigma_{\rm m}^2} \tag{5.1}$$

where

$$\sigma_m = \frac{{F_{\rm obs}}^m}{S/N} \tag{5.2}$$

is the uncertainty in the observed flux and S/N is the signal-to-noise ratio in the continuum (Sect. 5.2). Further, this array of χ^2 estimates was quadratically inter-

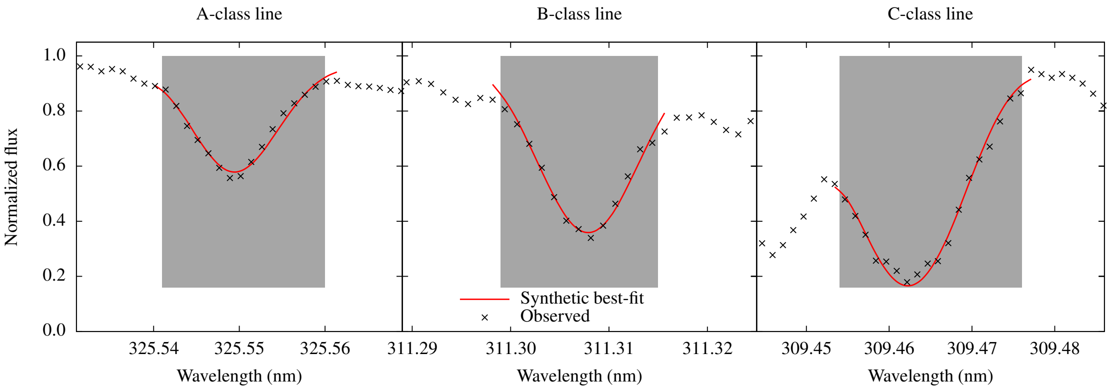

Fig. 5.3. Typical fits of synthetic line profiles to OH UV lines in the observed spectrum of HD 122563. The observed lines belong to different quality classes, as indicated above each panel (see Sect. 5.4.1 for details). Black crosses show the observed spectrum, red lines are best-fitting synthetic spectra selected using a globally fixed $v_{\rm brd}$. Shaded areas mark the fitting regions that were selected individually for each OH UV line.

polated in the $j, k, l-$ space to obtain better precision in the determined $\Delta\lambda^i$, ${v_{\rm brd}}^i$, and A(O)^i. The latter three values were determined individually for each OH UV line, by finding a minimum in the array of χ^2 estimates in the $j, k, l-$ space. The best-fitting synthetic line profiles obtained in this step were used to compute the line equivalent widths of each OH UV line, W_i, which were used further in the determination of 3D–1D abundance corrections and 3D LTE oxygen abundances (Sect. 5.4.2). Note, however, that oxygen abundances determined in this step, A(O)^i, were used solely for the estimation of $W_{\rm i}$ and excluded from further analysis. We also add that the individual $\Delta\lambda^i$ values are consistent with a single value of radial velocity within ±1 km/s.

In the last step, the ${\chi^2}_i$ estimates were summed up over all i spectral lines to find the global best-fitting broadening velocity, ${v_{\rm brd}}^{\rm 1D}$. We then used this fixed value of ${v_{\rm brd}}^{\rm 1D}$, together with the individual estimates of $\Delta\lambda^i$ for each OH UV line, and recomputed χ^2 values again, with the only fitting parameter now being the oxygen abundance, A(O)^i. A search for the minimum in the array of these new ${\chi^2}_i$ estimates yielded the final 1D LTE oxygen abundances as derived from each oxygen line, $\mathrm{A(O)}^i_{\rm 1D\ LTE}$. Therefore, our final 1D LTE oxygen abundances were determined using a fixed value of $v_{\rm brd}$ with all OH UV lines. In fact, these abundances were very similar to those obtained using individual values of $v_{\rm brd}$, i.e., as determined in the previous step above; the largest difference between the estimates obtained using the two methods would rarely exceed $\approx$ 0.05 dex and typically would be below $\approx$ 0.01 dex.

The final 1D LTE oxygen abundance estimates obtained from each OH UV line, $\mathrm{A(O)}^{i}_{\mathrm{1D\ LTE}}$, are listed in the Table B.1. Typical fits of OH UV lines obtained during the last step in the χ^2 minimization procedure are shown in Fig. 5.3.

5.4.2 Determination of 3D LTE oxygen abundances

As in Dobrovolskas et al. (2015), 3D LTE oxygen abundances were determined using 3D–1D LTE abundance corrections.

The 3D–1D abundance correction, $\Delta_{\mathrm{3D-1D}}$, is defined as difference in the oxygen abundance, A(O), determined using the same spectral line of a given equivalent width, W, with the 3D hydrodynamical and 1D hydrostatic model atmospheres (see, e.g., Kučinskas et al. 2013; Dobrovolskas et al. 2015, for details). To determine the abundance corrections, for each individual OH UV line, we utilized COGs that were constructed using the 3D hydrodynamical `CO5BOLD` and 1D hydrostatic `LHD` model atmospheres. Spectral line synthesis computations involved in the determination of 3D–1D abundance corrections were performed with the `Linfor3D` package[3]. In this step we used the W_{i} that were determined in the first sweep of the line profile fitting (Sect. 5.4.1). Abundance corrections were then obtained by measuring the difference in the oxygen abundance between the two COGs at a given value of W_{i}. Finally, 3D LTE oxygen abundances, $\mathrm{A(O)}^{i}_{\mathrm{3D\ LTE}}$, were determined by adding the 3D–1D abundance corrections to the 1D LTE abundances, $\mathrm{A(O)}^{i}_{\mathrm{1D\ LTE}}$, obtained from the individual OH UV lines using `ATLAS9` model atmospheres (Sect. 5.4.1). The 3D–1D abundance corrections, $\Delta_{\mathrm{3D-1D}}$, together with 3D LTE oxygen abundances obtained from the individual OH UV lines, $\mathrm{A(O)}^{i}_{\mathrm{3D\ LTE}}$, are provided in Table B.1.

For each OH UV line we also produced COGs that were constructed using the averaged $\langle\mathrm{3D}\rangle$ model atmosphere. These COGs, together with those produced with the 3D hydrodynamical and 1D hydrostatic model atmospheres, were used to compute two additional abundance corrections, $\Delta_{\mathrm{3D-\langle 3D\rangle}}$ and $\Delta_{\mathrm{\langle 3D\rangle-1D}}$. Since the $\langle\mathrm{3D}\rangle$ model atmosphere is one-dimensional and is devoid of information about the horizontal inhomogeneities of thermodynamic and hydrodynamical quantities, the $\Delta_{\mathrm{3D-\langle 3D\rangle}}$ correction may be used to estimate the role of horizontal fluctuations in the line formation. Similarly, the $\Delta_{\mathrm{\langle 3D\rangle-1D}}$ correction measures the role of differences between $\langle\mathrm{3D}\rangle$ and 1D model atmospheres.

We also note that in the `Linfor3D` calculations we treated scattering as true absorption. The effects of continuum scattering on the 3D–1D abundance cor-

---

[3] `http://www.aip.de/Members/msteffen/linfor3d`

rections of OH UV lines were investigated in Hayek et al. (2011, see Fig. 18 and 19), but for hotter model atmospheres characterized by higher surface gravities. The authors found that the treatment of scattering may alter the 3D–1D abundance corrections by 0.05–0.1 dex at the metallicity of HD 122563. However, the authors used 1D `MARCS` model atmospheres for reference which does not warrant a differential comparison, because their 3D hydrodynamical and 1D reference models were computed using different opacities, equation of state, radiative transfer schemes and so on. Since the `CO`^{5}`BOLD` and `LHD` models share identical input microphysics, we expect that in our case the effect of scattering would be smaller with respect to the results of Hayek et al. (2011). A deeper investigation of the effects of continuum scattering on OH UV lines is however beyond the scope of the current work.

Since the OH UV lines are strong (equivalent widths of the strongest lines reach $\approx$ 13 pm), they are influenced by microturbulent broadening. It was therefore critical to select a correct value of the microturbulent velocity to be used in the computations of 1D LTE COGs with the 1D `LHD` model atmospheres. We approached this problem in the following way.

Our first step was to determine $\xi_{\rm mic}$ that would result from the 3D hydrodynamical `CO`^{5}`BOLD` model atmosphere of HD 122563. This was done by utilizing Method 1 from Steffen et al. (2013). In short, we selected 15 OH UV lines that covered the range of excitation potentials $0 < \chi < 2$ eV. For each of these lines, we computed 3D LTE COGs using the `CO`^{5}`BOLD` model atmosphere with the original (hydrodynamic) velocity field. Subsequently, the velocity field in the `CO`^{5}`BOLD` model was replaced by a depth-independent and isotropic $\xi_{\rm mic}$. We then utilized this modified model atmosphere to compute a number of COGs using various values of $\xi_{\rm mic}$. For each OH UV line we then picked the value of $\xi_{\rm mic}$ which replicated the line equivalent width, $W_{\rm i}$, determined using the original `CO`^{5}`BOLD` model atmosphere. Fig. 5.4 shows the resulting $\xi_{\rm mic}$ obtained using this approach for each of the 15 OH UV lines.

It is obvious from Fig. 5.4 that $\xi_{\rm mic}$ derived in this way is significantly lower than 2 km/s that was determined in the 1D NLTE analysis by Mashonkina et al. (2011) based on iron lines. This might be partly due to the deficiencies of the 3D model atmosphere (e.g., insufficient spatial resolution, issues with artificial viscosity, and so forth; see Steffen et al. 2013, for a detailed discussion). However, as it will be shown below, such a procedure for selecting the microturbulent velocity allows to compensate for the inadequacies in the 3D model atmosphere,

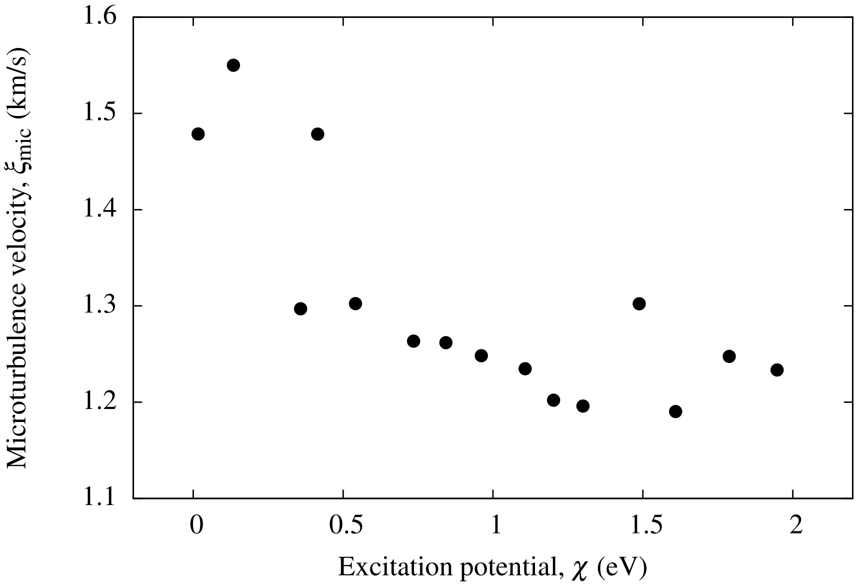

Fig. 5.4. Microturbulence velocities derived from individual OH UV lines using the 3D hydrodynamical `CO5BOLD` model atmosphere.

in effect yielding nearly identical 3D–1D abundance corrections irrespective of $\xi_{\rm mic}$ used to obtain 1D LTE oxygen abundances. Therefore, for the computation of 1D `LHD` and ⟨3D⟩ COGs – which were further used to compute 3D–1D abundance corrections (see below) – we used the average $\xi_{\rm mic} = 1.30$ km/s. The uncertainty of this estimate is ±0.11 km/s which is a standard deviation of line-to-line variation of the determined $\xi_{\rm mic}$.

In order to justify our claims regarding the choice of microturbulence, we have used two 3D model atmospheres of different spatial resolution and very similar spatial extent in order to compute $\xi_{\rm mic}$ values using the procedure described above (see Table 5.2 for a description of the model atmospheres and results). The results are shown in Fig. 5.5 (top). One may note immediately that the high-resolution model atmosphere predicts higher $\xi_{\rm mic}$ values. This is expected since higher spatial resolution allows for the appearance of smaller-scale turbulent eddies (e.g., Steffen et al. 2013). Then, for each of the two models we computed a mean microturbulence velocity by averaging $\xi_{\rm mic}$ values determined using 15 OH UV lines. These two values (cf. Table 5.2) of the mean

Table 5.2. Spatial characteristics of the model atmospheres of HD 122563 used and respective mean $\xi_{\rm mic}$ values derived for the 3D–1D analysis of HD 122563.

Spatial resolution	Spatial extent [Mm]	Grid points $x \times y \times z$
Low	$4.38 \times 4.38 \times 2.90$	$160 \times 160 \times 200$
High	$4.40 \times 4.40 \times 3.13$	$375 \times 375 \times 330$

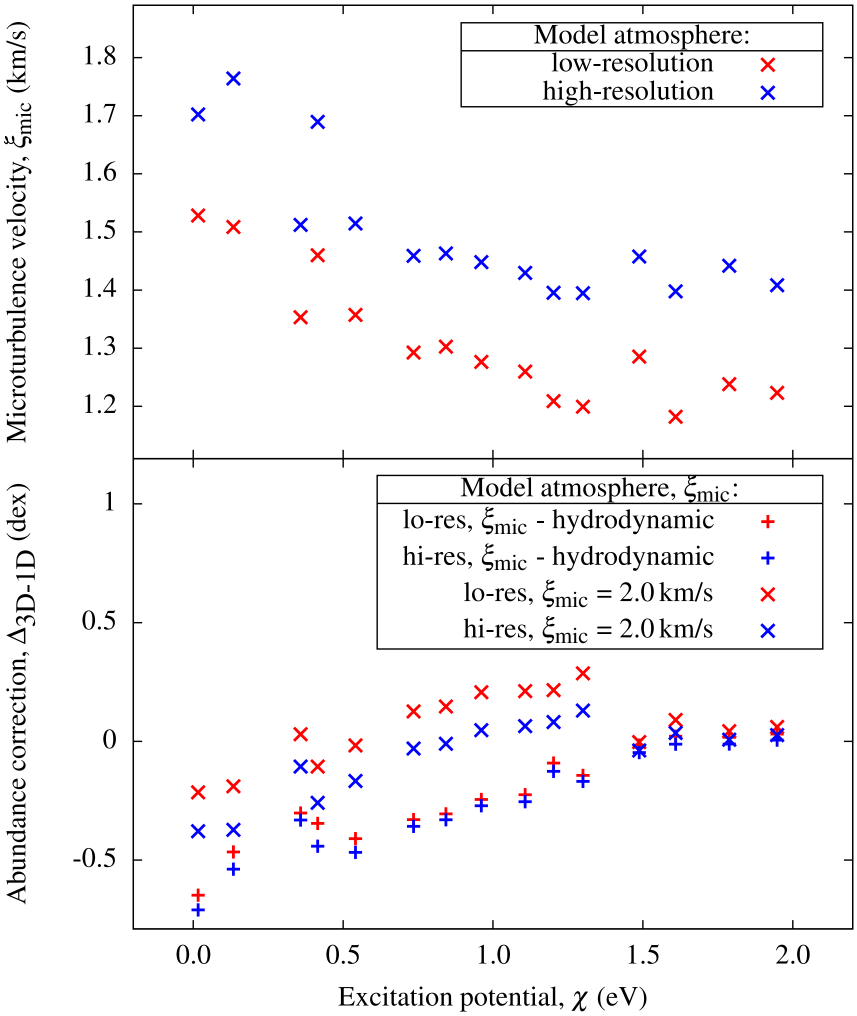

Fig. 5.5. Top: microturbulence velocities, $\xi_{\rm mic}$, determined from the model atmospheres that were computed using different spatial resolution. Bottom: 3D–1D abundance corrections computed with the two model atmospheres and different approach to $\xi_{\rm mic}$ (see text and legend for details).

microturbulence velocity were used to compute 3D–1D abundance corrections corresponding to the low- and high-resolution cases (Fig. 5.5, bottom).

The obtained results show that, once $\xi_{\rm mic}$ is calibrated with the help of the 3D model atmosphere, the resulting abundance corrections are very similar. This is because in both the low- and high-resolution case $\xi_{\rm mic}$ was adjusted in such a way that the 1D model atmospheres would reproduce the line strengths predicted with the corresponding 3D hydrodynamical model atmosphere as accurately as possible. This, in effect, made the 3D–1D abundance corrections insensitive to both the shortcomings of the 3D hydrodynamical model atmospheres (i.e., spatial resolution in our case) and microturbulence used in the 1D LTE abundance analysis. On the other hand, if the 3D–1D abundance corrections were computed using some fixed value of $\xi_{\rm mic}$ (for example, the one determined in the process of

1D LTE abundance analysis), the abundance corrections obtained using the low- and high-resolution 3D hydrodynamical model atmospheres will be different. This is illustrated in Fig. 5.5 (Bottom) where we also show 3D–1D abundance corrections computed using the two 3D hydrodynamical model atmospheres and identical $\xi_{\rm mic} = 2.0\,$km/s utilized with the 1D `ATLAS9` model atmospheres. Indeed, in this case the differences in the abundance corrections are significant and reach $\sim 0.2\,$dex.

As recently noted by Gallagher et al. (2016), formation of carbon- and oxygen- bearing molecules is very sensitive to the C/O abundance ratio and abundances of these elements should be determined simultaneously (see also González Hernández et al. 2010). The C/O ratio determines which chemical species – carbon or oxygen – is in minority and which of these chemical species will be locked by the formation of CO molecules (see Dobrovolskas et al. 2013, who, in their Appendix C, investigated case where $\mathrm{C/O} < 1$). Moreover, line formation in 3D model atmospheres is expected to be more sensitive to the C/O ratio than that of 1D model atmospheres, hence we cannot expect that the possible errors would cancel in our differential approach.

In case of HD 122563, a 1D-based analysis of (Spite et al. 2005) suggests $A(\mathrm{C}) = 5.23$ and $A(\mathrm{O}) = 6.54$, what results in a very low $\mathrm{C/O} \approx 0.05$. Alexeeva & Mashonkina (2015) used LTE analysis of molecular lines and NLTE analysis of atomic lines and derived $A(\mathrm{C}) = 5.10$, which implies even lower $\mathrm{C/O} \approx 0.03$. Also, such C/O ratio means that oxygen is majority species with respect to carbon, variation of $A(\mathrm{C})$ should not influence formation of OH lines and we should be safe with using 1D-based $A(\mathrm{C})$. Even if in principle a 3D analysis may yield a C/O ratio that is slightly different from the one obtained by Spite et al. (2005), i.e., because of different 3D–1D abundance corrections for oxygen and carbon, this (supposedly, small) change in the carbon abundance should not have a noticeable effect on the strengths of the OH lines. However, we have carried out tests in order to test our claims.

Fig. 5.6 shows 3D–1D abundance corrections plotted versus C/O ratio for a set of 14 real (i.e., real χ and measured $W_{\rm i}$) OH lines. It is seen that when $0.025 < \mathrm{C/O} < 0.1$ (nearly, 0.6 dex in $A(\mathrm{C})$) the abundance corrections of most lines vary by less than 0.01 dex. We hence conclude that uncertainties on the C/O ratio does not influence our results in any significant way and 1D-based $A(\mathrm{C})$ could be used without introducing additional uncertainties. We add that this could be expected for the majority of RGB stars because such stars have experienced the

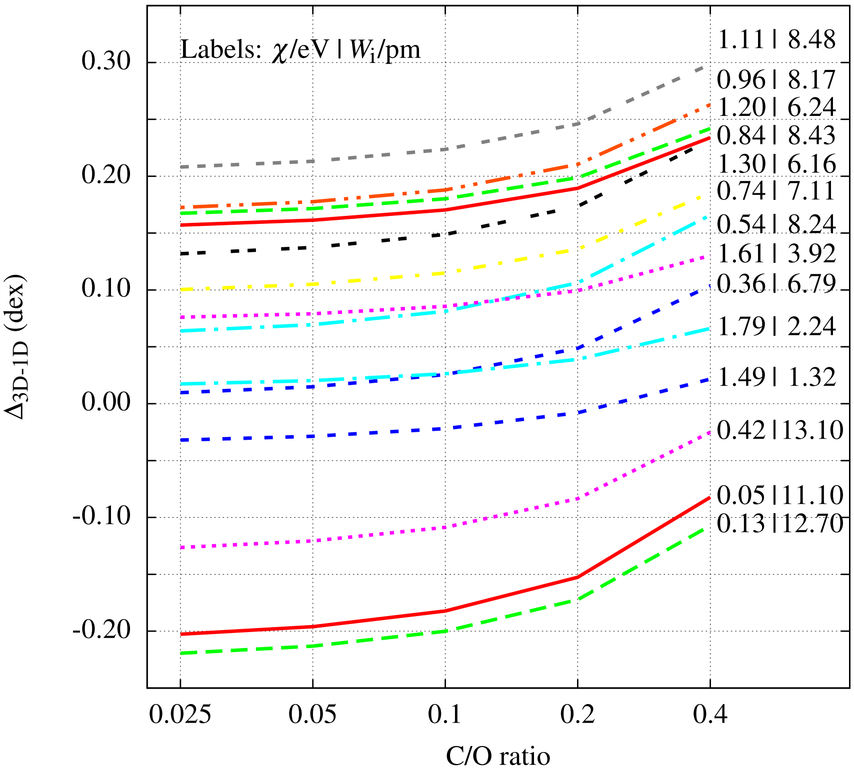

Fig. 5.6. Dependency of $\Delta_{\rm 3D-1D}$ on C/O ratio in a sample of 14 OH UV lines. Labels indicate $\chi \mid W_{\rm i}$ of individual lines (in eV and pm, respectively).

first dredge-up and had their carbon depleted relative to the initial value. Note, however, that the situation is entirely different when $\mathrm{C/O} \gtrsim 1$: in this case even small changes in the carbon abundance have a dramatic effect on the strength of OH lines. As it has been recently demonstrated by Gallagher et al. (2016), that in such situations carbon and oxygen abundances should be determined in 3D simultaneously.

5.4.3 Error budget

Four factors contribute to the uncertainty of the oxygen abundances determined from individual OH lines:

- line profile fitting error;
- errors in the atmospheric parameters;
- error in the continuum placement;
- error in equivalent width measurements.

In case of each individual OH UV line, the line profile fitting error, σ_{χ^2}, was computed by evaluating the difference in $\mathrm{A(O)}^{i}_{\mathrm{1D\ LTE}}$ that satisfied the condition $\chi^2 - \chi^2{}_{min} = 1$, with the oxygen abundances determined using a fixed value of v_{brd} for all lines (Sect. 5.4.1).

Creevey et al. (2012) quotes errors on the determined T_{eff} and $\log g$ to be 41 K and 0.04 dex, respectively. We therefore computed four additional `ATLAS9` model atmospheres with T_{eff} and $\log g$ shifted from the values listed in Table 5.1 by ±41 K and ±0.04 dex, respectively. The differences between the oxygen abundances obtained from each OH UV line with these model atmospheres and those determined in Sect. 5.4.1 yielded errors due to uncertainties in the atmospheric parameters, $\sigma_{\Delta \mathrm{Teff}}$ and $\sigma_{\Delta \log\ \mathrm{g}}$.

According to Spite et al. (2005), the error in ξ_{mic} is 0.2 km/s. In order to evaluate the uncertainties in the oxygen abundances due to the imprecise determination of ξ_{mic}, we have repeated the spectral synthesis computations with `SYNTHE` for each OH UV line, using $\xi_{\mathrm{mic}} = 1.8$ and 2.2 km/s. A subsequent abundance determination using these new theoretical line profiles and comparison of the obtained abundances with those determined in Sect. 5.4.1 provided errors due to the uncertainty in ξ_{mic}, $\sigma^{\mathrm{1D}}_{\mathrm{vmic}}$. For most lines, this error was very small and only in rare cases exceeded 0.1 dex.

As noted in Sect. 5.4.2, for the calculation of $\Delta_{\mathrm{3D-1D}}$, we used $\xi_{\mathrm{mic}} = 1.30 \pm 0.11$ km/s. In order to estimate the error due to the uncertainty in the determined value of ξ_{mic}, we carried out 1D LTE line synthesis computations using the `Linfor3D` package and `LHD` model atmosphere, again with $\xi_{\mathrm{mic}} = 1.41$ and 1.19 km/s. The obtained COGs were used to determine abundance corrections $\Delta_{\mathrm{3D-1D}}$ and, subsequently, 3D LTE oxygen abundances. Comparison of these 3D LTE abundances with those determined in Sect. 5.4.2 provided us with the error on the 3D LTE abundances, $\sigma^{\mathrm{3D}}_{\mathrm{vmic}}$. Again, these errors were very small and typically well below 0.03 dex.

To estimate the error in the oxygen abundance due to the uncertainty in the continuum placement, we used a wavelength-dependent error $\sigma_{\mathrm{flux}}(\lambda) \equiv (S/N)^{-1}$ that was determined as described in Sect. 5.2. The observed spectrum was scaled by dividing it by $1.0 \pm \sigma_{\mathrm{flux}}(\lambda)$. We then repeated the 1D LTE abundance determination with the scaled observed spectrum and determined σ_{cont} by comparing the obtained result with that determined in Sect. 5.4.1.

The final source of uncertainty stems from the imprecise measurements of W_{i}. As discussed in Sect. 5.4.2, W_{i} measurements were used solely for the estimation of the 3D–1D abundance corrections and hence they influence only $\mathrm{A(O)}^{i}_{\mathrm{3D\ LTE}}$. We assumed that the uncertainty on the determined W_{i} was 5%, a rather conservative estimate. Using this error, we recomputed the $\Delta_{\mathrm{3D-1D}}$ abundance corrections and found that the resulting influence on $\mathrm{A(O)}^{i}_{\mathrm{3D\ LTE}}$ never exceeded 0.025 dex and, typically, was below 0.01 dex.

The final errors in oxygen abundances as determined from each OH UV line were computed as a square root of the sum of relevant errors in quadratures and are given in Table B.1.

5.5 Results and discussion

5.5.1 1D LTE and 3D LTE oxygen abundance in HD 122563

The 1D LTE oxygen abundances obtained from individual OH UV lines are plotted against the line excitation potential, equivalent width, and central wavelength in Fig. 5.7 (left panels). The weighted least squares fitting of 1D LTE abundances yielded a slope $d\mathrm{A(O)}_{\mathrm{1D\ LTE}}/d\chi = -0.25\pm0.03$ dex/eV. This result is very similar to the one derived by Aoki (2015), who has analysed the extremely metal-poor subgiant star BD+44°493 and derived $d\mathrm{A(O)}_{\mathrm{1D\ LTE}}/d\chi = -0.23 \pm 0.03$ dex/eV. Applying the Student's *t*-test to our data, the null hypothesis that the slope between the abundance and χ is zero can be rejected at *a posteriori* significance level $\alpha = 0.01\%$.

These results demonstrate that 1D LTE oxygen abundance depends on these line parameters indicating systematic errors in the modelling. For example, the negative slope in the $\mathrm{A(O)}^{i}_{\mathrm{1D\ LTE}} - \chi$ plane may indicate that the model atmosphere is too hot, whereas accurate flux measurements (Creevey et al. 2012) and non-LTE analysis of iron lines (Mashonkina et al. 2011) suggest that this is not the case. The lowest quality lines (class C) typically show a larger line-to-line scatter of the oxygen abundances. The trends, however, are seen in cases of both best (classes A–B) and lower (class C) quality lines. Similar results have been obtained earlier by other authors who also noticed that the oxygen abundance determined from OH lines either in the UV or IR showed trends with the line parameters, such as excitation potential and/or line equivalent width (e.g., Meléndez & Barbuy 2002; Aoki 2015; Dobrovolskas et al. 2015)[4].

---

[4] Trends seen in the different panels of Fig. 5.7 are not entirely independent. For example, lines with the highest excitation potential are also the weakest, thus negative slope seen in the $\mathrm{A(O)}^{i}_{\mathrm{1D\ LTE}} - \chi$ plane translates into opposite trend seen in the $\mathrm{A(O)}^{i}_{\mathrm{1D\ LTE}} - W_{\mathrm{i}}$ plane.

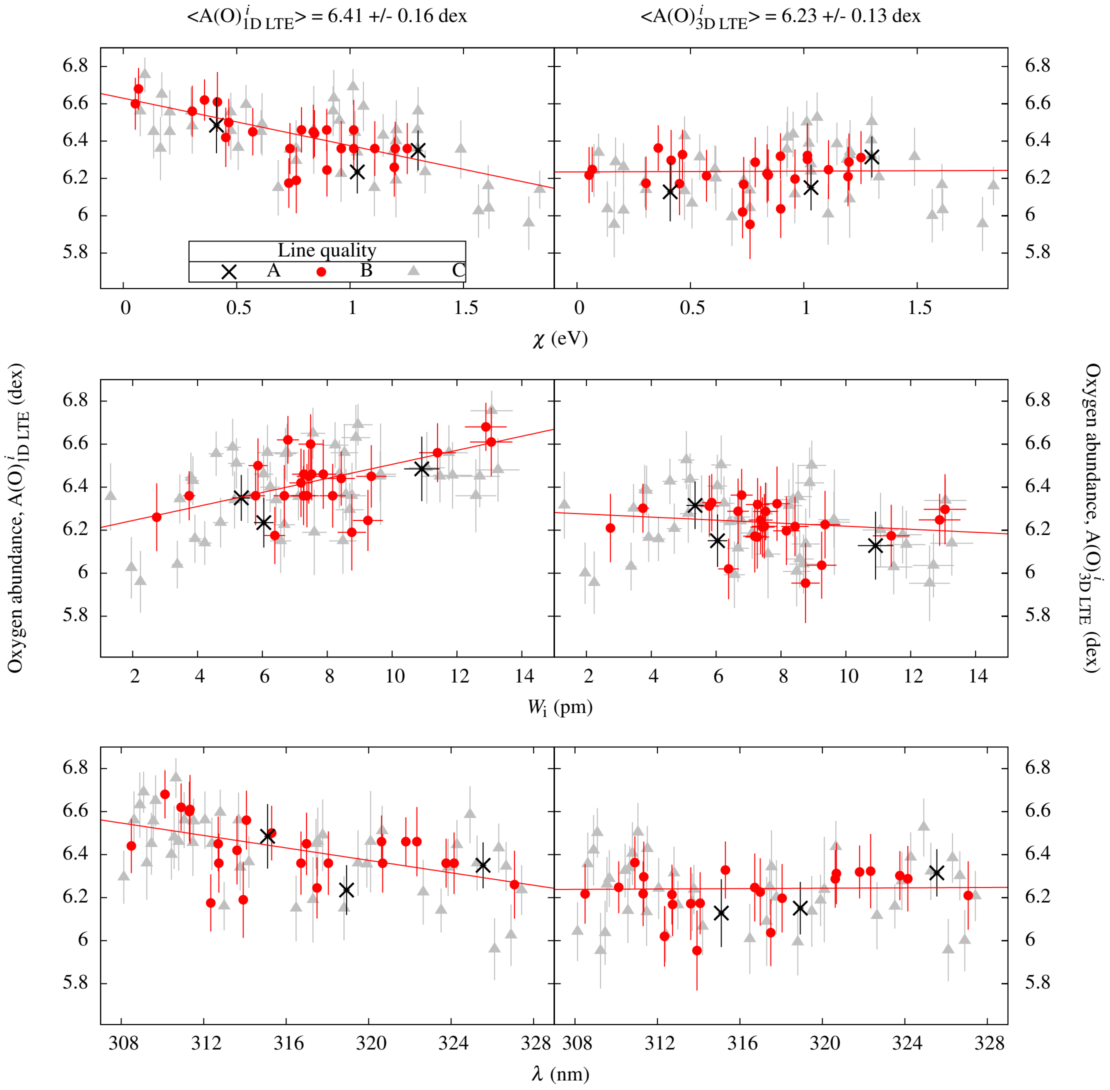

Fig. 5.7. Oxygen abundances determined from the individual OH UV lines using a classical 1D LTE (left) and 3D LTE abundance analysis techniques (right; see text for detail) The top, middle, and bottom panels show A(O) plotted versus excitation potential, χ, line equivalent width, $W_{\rm i}$, and wavelength, λ, respectively. Different symbols mark spectral lines of different quality where A-class lines are the best/cleanest (see Sect. 5.4.1 for details). The mean abundance (noted at the top of each column) was computed as a weighted average and the error is RMS of all abundances and reflect spread in the derived abundances (all derived abundances are provided in Appendix B).

The situation looks significantly better when 3D LTE oxygen abundances are used instead (Fig. 5.7, right panels). The trends now virtually vanish, with, e.g., $d\text{A(O)}_{\rm 3D\ LTE}/d\chi = 0.00 \pm 0.04$ dex/eV. This is confirmed by the Student's t-test which yields a *a posteriori* significance level $\alpha = 15\%$ computed using our data. This large number gives a clear indication that the rejection of the null hypothesis is not warranted. In this context it is interesting to note that Dobrovolskas et al. (2015) have also applied 3D–1D abundance corrections to their 1D LTE oxygen abundances determined from OH IR lines in four-metal

Table 5.3. 1D LTE and 3D LTE abundances of oxygen in the atmosphere of HD 122563 determined using OH UV and IR and [O I] lines. Oxygen abundances obtained using IR lines are from Dobrovolskas et al. (2015), while that determined using the [O I] line was taken from Spite et al. (2005)

	A(O)		[O/Fe]	
	1D LTE	3D LTE	1D LTE	3D LTE
OH UV	6.41 ± 0.16	6.23 ± 0.13	0.25 ± 0.16	0.07 ± 0.13
OH IR	6.63 ± 0.10	6.39 ± 0.11	0.47 ± 0.10	0.23 ± 0.11
[O I]	6.54 ± 0.15	6.53 ± 0.15	0.38 ± 0.15	0.37 ± 0.15

poor giants, including HD 122563. In their case, however, this procedure did not help to entirely remove the trends seen in the $\mathrm{A(O)}^{i}_{\mathrm{1D\ LTE}} - \chi$ plane, although one may also argue that the number of OH IR lines used in their study was small and thus it was difficult to judge whether these trends were statistically significant in the first place.

For comparison, we collected 1D LTE and 3D LTE oxygen abundances determined in HD 122563 using OH UV/IR lines (this work and Dobrovolskas et al. 2015) and the forbidden [O I] line (literature data) in Table 5.3 (in case of OH UV/IR lines we provide abundances that are weighted averages of measurements from individual lines; the RMS error given in Table 5.3 measures the spread in individual abundances). One may conclude that there is a fair agreement between the 3D LTE oxygen abundances obtained using OH UV and IR lines. On the other hand, there is a noticeable difference between the 3D LTE oxygen abundance determined from OH UV lines and that obtained from the forbidden [O I] line. It is possible that these differences may point to the importance of non-LTE effects in the formation of OH lines which were not taken into account in our study of OH UV/IR lines. Indeed, OH UV/IR lines form in the outer atmosphere where, for example, overdissociation due to the non-local UV radiation field may lead to smaller number densities of OH molecules (i.e., with respect to those expected in LTE), and thus, to slightly weaker lines in 3D NLTE than those in 3D LTE (see discussion in Asplund & García Pérez 2001). This would result in less negative 3D–1D abundance corrections and, consequently, to higher oxygen abundances obtained from OH lines – which would bring them into better agreement with those obtained from the forbidden [O I] line. Moreover, the 3D non-LTE effects may also influence the slope in the $\mathrm{A(O)}^{i}_{\mathrm{3D\ LTE}}$ vs. χ plane, as the size of these effects may be different for lines forming at different optical depths in the atmosphere (see, e.g., the 3D non-LTE study of iron line formation by Amarsi et al. 2016). However, a detailed investigation of this problem is beyond the scope of the present study.

5.5.2 OH UV line formation

To better understand the OH UV line formation in the 3D hydrodynamical and 1D hydrostatic model atmospheres we focus on the abundance corrections $\Delta_{\rm 3D-1D}$ and their components – $\Delta_{\rm 3D-\langle 3D\rangle}$ and $\Delta_{\rm \langle 3D\rangle-1D}$ (Fig. 5.8). It is evident that the $\Delta_{\rm 3D-1D}$ correction depends on both χ and $W_{\rm i}$. This is in contrast with the findings of Dobrovolskas et al. (2015) for OH IR lines where no such dependence has been found. In our case, the $\Delta_{\rm 3D-1D}$ corrections are negative for low excitation lines but then progressively approach 0.0 dex for higher excitation lines. The plot also indicates that the $\Delta_{\rm 3D-1D}$ corrections decrease with increasing $W_{\rm i}$. Such behaviour is not unexpected since in our OH UV line sample line strength anti-correlates with the line excitation potential, i.e., lines with lower χ values are stronger. We have not found any significant relation between the abundance corrections and line wavelength though. This, again, is plausible as the wavelength region where the OH UV lines are located is rather narrow and

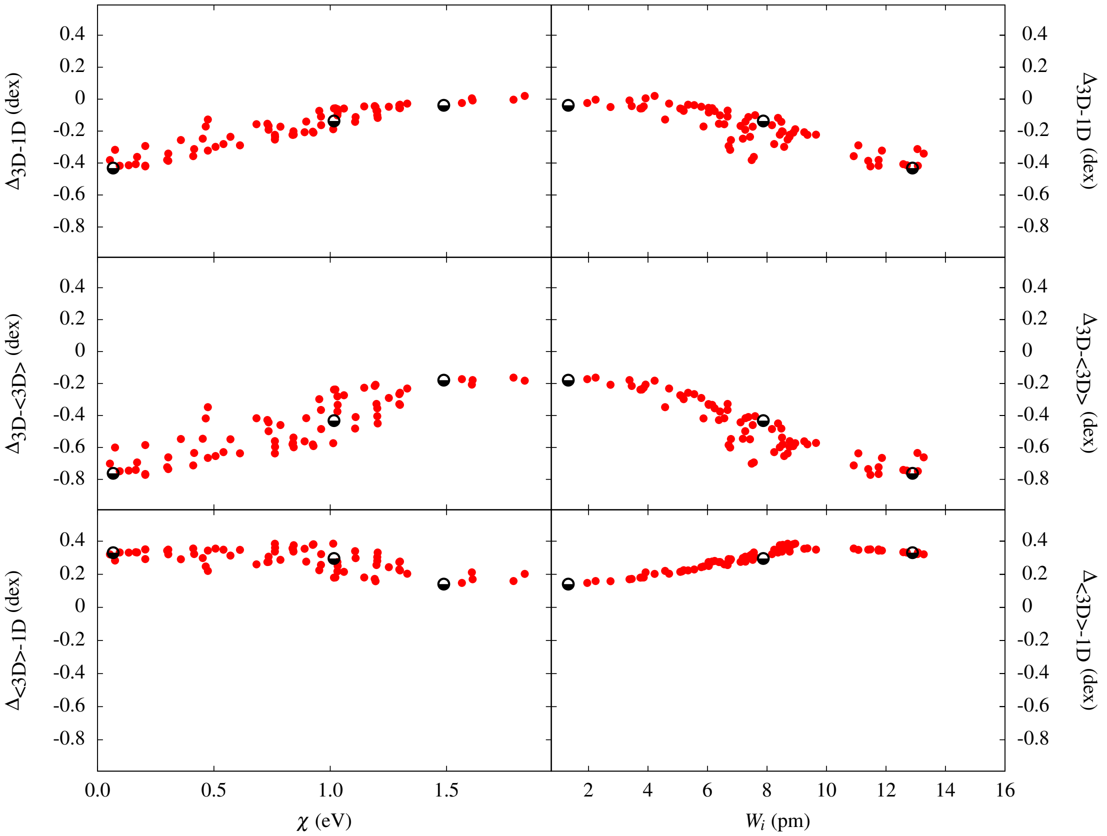

Fig. 5.8. The 3D–1D abundance corrections for individual OH UV lines: $\Delta_{\rm 3D-1D}$ (top panels), $\Delta_{\rm 3D-\langle 3D\rangle}$ (middle panels), and $\Delta_{\rm \langle 3D\rangle-1D}$ (bottom panels) plotted versus the line excitation potential, χ (left), and line equivalent width, W (right). Red dots mark all OH UV lines in our sample, half-filled black circles represent lines whose contribution functions are shown in Fig. 5.9 (see text for details). $\Delta_{\rm 3D-1D}$ abundance corrections are provided in Appendix B.

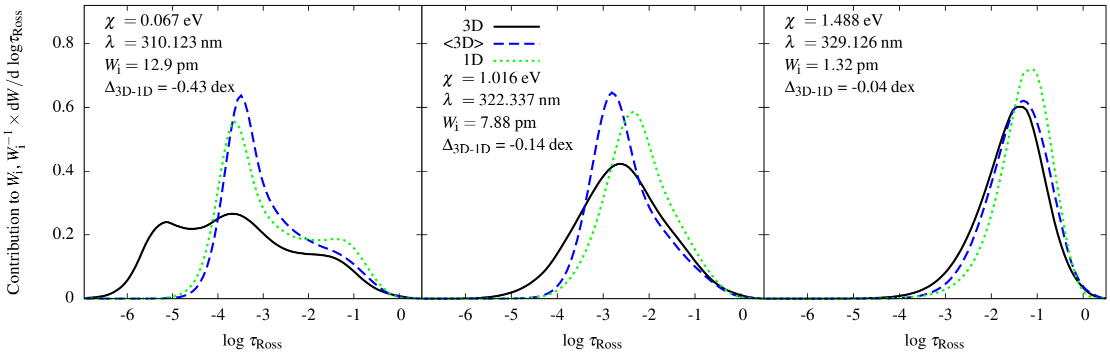

Fig. 5.9. Normalized contribution functions (contribution function of a given spectral line measures the rate at which line equivalent width changes at any given optical depth; see Magain 1986) computed using 3D hydrodynamical, averaged $\langle 3D \rangle$, and 1D hydrostatic model atmospheres for the three OH UV lines marked in Fig. 5.8. The parameters of these spectral lines sample the entire range of χ and W_i values of OH UV lines used in our work (see Table 5.4 and text for details).

thus the continuum opacity (as well as line formation depth) is similar for all OH UV lines.

The trends seen in Fig. 5.8 are caused by an interplay between several factors:

- lines with the lowest excitation potentials are on average strongest. Their formation therefore extends farthest into the outer atmosphere where temperature fluctuations are largest (cf. Fig. 5.9 and 5.2). This leads to stronger lines in 3D and, thus, to largest and negative $\Delta_{3D-\langle 3D \rangle}$ abundance corrections. Since with increasing χ (and thus decreasing W_i) the outer boundary of the line formation region slowly shifts to higher optical depths, the influence of temperature fluctuations becomes less important there and thus $\Delta_{3D-\langle 3D \rangle}$ corrections gradually decrease in their magnitude;

- on the other hand, while the difference between the average ⟨3D⟩ and 1D temperature profiles is small and varies little over the line formation region, there is a systematic difference in the temperature gradient in the continuum forming layers in the two model atmospheres (around $\log\tau_{Ross} \approx 0$, see Fig. 5.2). This not only leads to differences in the radiative continuum

Table 5.4. Line parameters, equivalent widths and abundance corrections – Δ_{3D-1D}, $\Delta_{3D-\langle 3D \rangle}$ $\Delta_{\langle 3D \rangle-1D}$ – of the OH UV lines shown in Fig. 5.9.

λ nm	χ eV	W_i pm	Δ_{3D-1D} dex	$\Delta_{3D-\langle 3D \rangle}$ dex	$\Delta_{\langle 3D \rangle-1D}$ dex
310.123	0.067	12.9	-0.43	-0.76	0.33
322.337	1.016	7.88	-0.14	-0.43	0.29
329.126	1.488	1.32	-0.04	-0.18	0.14

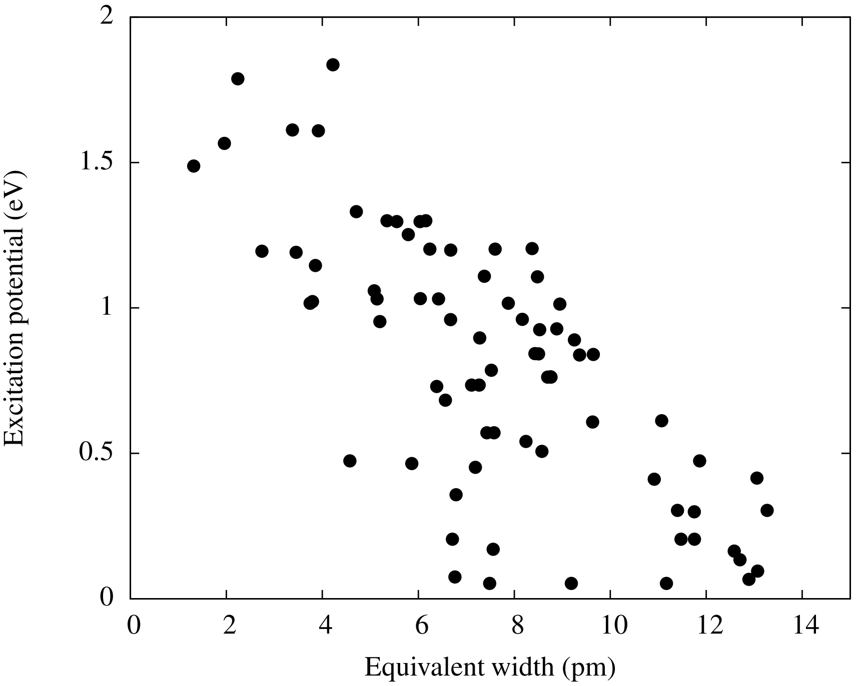

Fig. 5.10. Line excitation potential, χ, of OH UV lines used in our study, plotted versus the line equivalent width, $W_{\rm i}$.

> flux in the UV produced by the ⟨3D⟩ and 1D model atmosphere, respectively, but also translates into different slopes of the linear parts of the respective COGs. Obviously, the abundance corrections derived from two curves of growth characterised by different slopes must be proportional to the line strength, thus explaining the very tight correlations between the $\Delta_{\langle 3\rm D\rangle-1\rm D}$ correction and $W_{\rm i}$.

In order to gain more physical insights into the 3D LTE formation of OH UV lines we also consider fictitious lines. Let us first note that there is a relation between the line excitation potential, χ, and line equivalent width, $W_{\rm i}$ (Fig. 5.10), and this, as it will be shown below, has a direct influence on the 3D–1D abundance corrections for OH UV lines.

To understand the basic tendencies in the behaviour of 3D–1D abundance corrections seen in Fig. 5.8, we computed abundance corrections for fictitious spectral lines with variable line excitation potential, χ, and equivalent width, $W_{\rm i}$. The relation between χ and $W_{\rm i}$ was defined in such a way that it would follow the best-fitting line in Fig. 5.10. The resulting abundance corrections are shown in Fig. 5.11 while the contribution functions for four selected lines are shown in Fig. 5.12. These figures together give a clear indication that the relation between χ and $W_{\rm i}$ in our OH UV line sample plays an important role in defining the 3D–1D abundance corrections. At the lowest excitation potentials

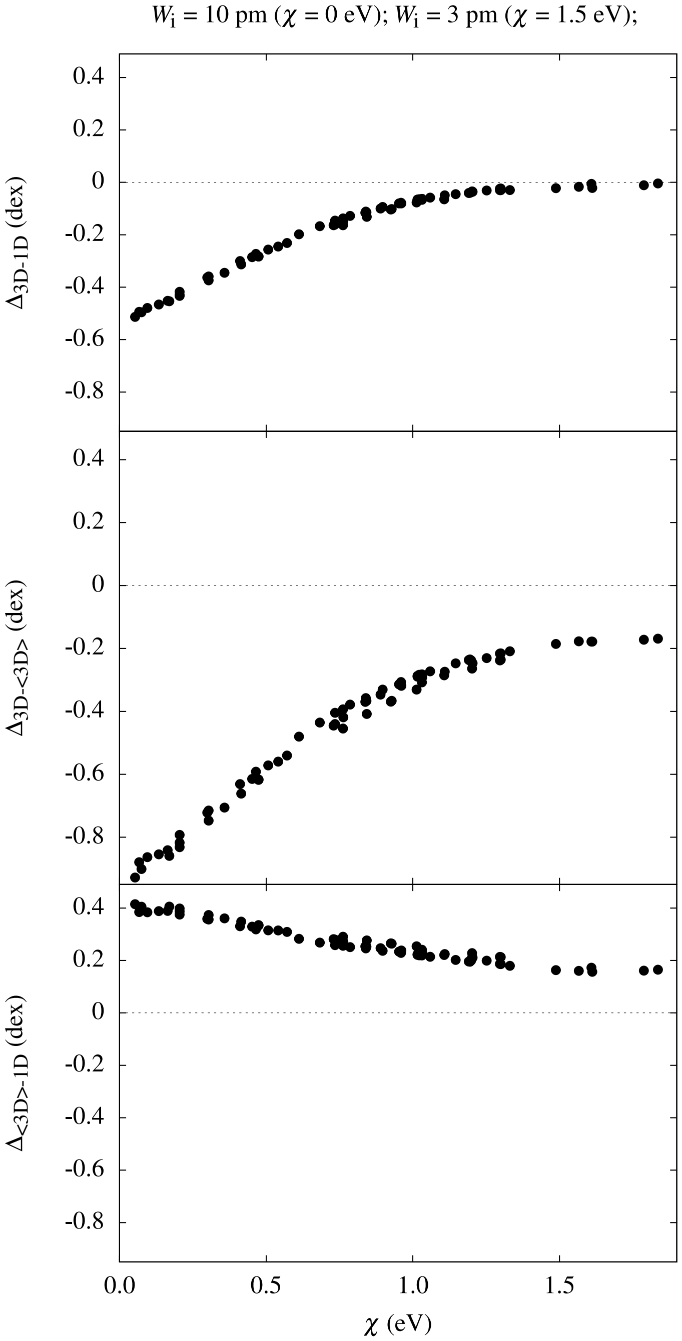

Fig. 5.11. The three abundance corrections plotted against excitation potential χ. Abundance corrections were computed for fictitious lines where the line strength varied linearly with the excitation potential, from W_i = 10 pm for lines with χ = 0 eV to W_i = 3 pm for lines with χ = 1.5 eV.

lines are strongest and thus their formation reaches the outermost atmospheric layers where temperature and line opacity fluctuations are largest. This leads to large negative $\Delta_{3D-\langle 3D\rangle}$ corrections which are counterweighted to some extent by significant but positive $\Delta_{\langle 3D\rangle-1D}$ abundance corrections. With increasing line excitation potential, lines also become weaker and thus their formation is confined to deeper atmospheric layers where temperature fluctuations are smaller. This

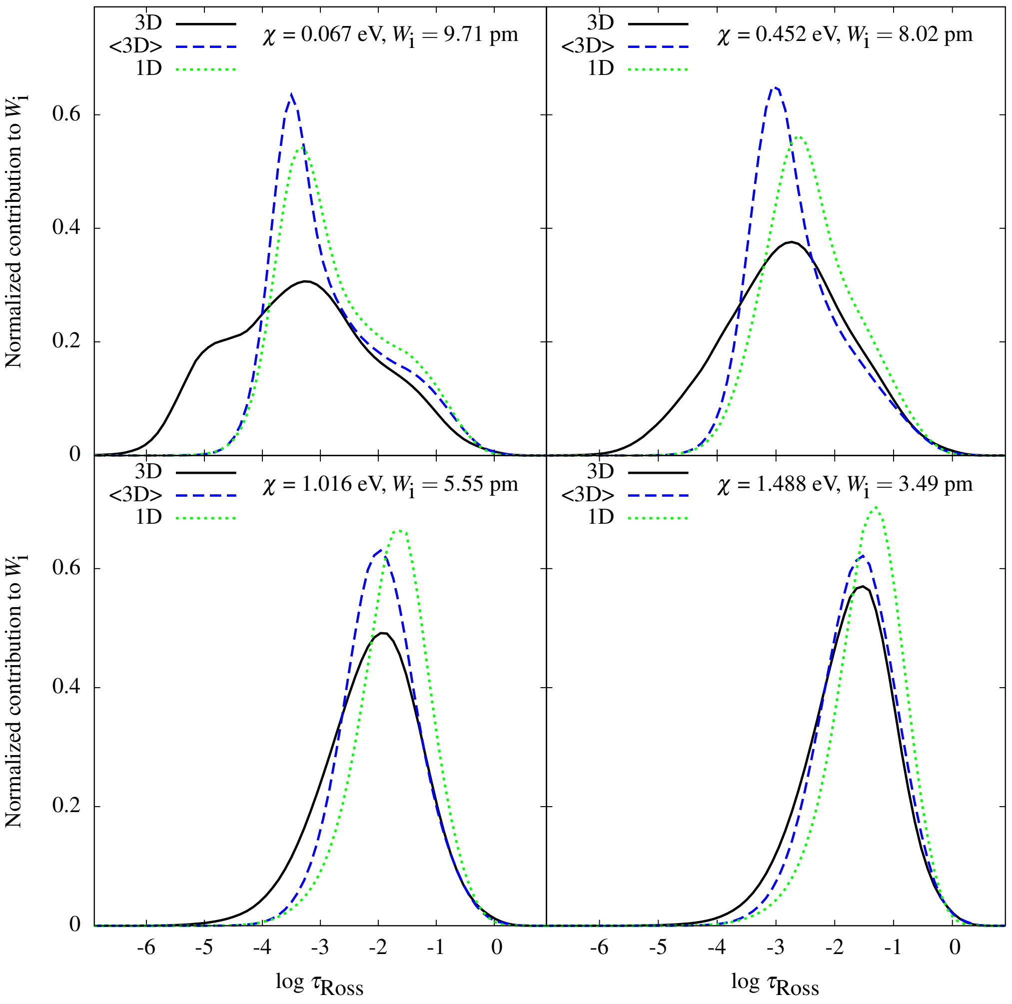

Fig. 5.12. Same as in Fig. 5.9, but for four fictitious lines that were defined by a linear $\chi - W_\mathrm{i}$ relationship. See Table 5.5 and text for details.

leads to smaller (i.e., more positive) $\Delta_{\mathrm{3D}-\langle\mathrm{3D}\rangle}$ corrections. Since the depth of the line formation changes only insignificantly with further increasing line excitation potential, the $\Delta_{\mathrm{3D}-\langle\mathrm{3D}\rangle}$ correction stops growing with χ and the behaviour of the total abundance correction, $\Delta_{\mathrm{3D}-\mathrm{1D}}$ is governed by the slowly decreasing $\Delta_{\langle\mathrm{3D}\rangle-\mathrm{1D}}$ correction.

Table 5.5. Line parameters and abundance corrections – $\Delta_{\mathrm{3D}-\mathrm{1D}}$, $\Delta_{\mathrm{3D}-\langle\mathrm{3D}\rangle}$, $\Delta_{\langle\mathrm{3D}\rangle-\mathrm{1D}}$ – for the four lines displayed in Fig. 5.12. These lines are defined by a fictitious W_i that is determined by an approximate linear fit to a χ - W_i relationship in Fig. 5.10

λ nm	χ eV	W_i pm	$\Delta_{\mathrm{3D}-\mathrm{1D}}$ dex	$\Delta_{\mathrm{3D}-\langle\mathrm{3D}\rangle}$ dex	$\Delta_{\langle\mathrm{3D}\rangle-\mathrm{1D}}$ dex
310.123	0.067	9.71	-0.50	-0.88	0.38
313.618	0.452	8.02	-0.29	-0.62	0.33
322.337	1.016	5.55	-0.07	-0.29	0.22
329.126	1.488	3.49	-0.02	-0.19	0.17

One may therefore conclude that the complex dependence of the total abundance correction, $\Delta_{\mathrm{3D-1D}}$, on both χ and W_{i} is mostly due to the fact that OH UV lines used in our study cover a wide range both in χ and W_{i}. This also explains why the $\Delta_{\mathrm{3D-1D}}$ abundance corrections were largely independent of χ in Dobrovolskas et al. (2015). All OH IR used in the latter study were very weak and thus formed at similar optical depths which resulted in similar abundance corrections for all lines.

5.5.3 Early Galactic evolution of oxygen

The mean [O/Fe] ratios determined in HD 122563 using OH UV/IR lines and the forbidden [O I] line are summarized in Table 5.3. To compute these [O/Fe] ratios we used the 1D NLTE estimate of [Fe/H] = −2.60 from Mashonkina et al. (2011) and the recently determined 3D NLTE solar oxygen abundance of $\mathrm{A(O)}_{\odot} = 8.76$ from Steffen et al. (2015)[5]. In the context of our study, it would be preferable to account for the 3D and non-LTE effects on the estimate of [Fe/H], too. However, this would require a full 3D NLTE study of iron abundance because, as shown by Klevas et al. (2016), simply adding 3D–1D abundance corrections to the 1D NLTE abundance estimates may lead to erroneous result. Such analysis is beyond the scope of the present study.

[O/Fe] values determined in HD 122563 using OH UV (this work) and OH IR lines (Dobrovolskas et al. 2015) suggest a mean (unweighted) value of $\langle[\mathrm{O/Fe}]\rangle = 0.16 \pm 0.12$. Oxygen abundance estimate obtained by Spite et al. (2005) using the forbidden [O I] line yields $[\mathrm{O/Fe}] = 0.37 \pm 0.15$. Although the oxygen-to-iron abundance ratios obtained from UV and IR lines are somewhat different, none of the values support the high over-abundance of oxygen in the early Galaxy, as argued by, e.g., Israelian et al. (2001). On the other hand, the two values are noticeably lower than the typical oxygen-to-iron abundance ratio that would be expected for the Galactic field stars at this metallicity, as seen in Fig. 5.13. This picture is also supported by the results of González Hernández et al. (2010) and Amarsi et al. (2015) who used 3D hydrodynamical model atmospheres to derive 3D LTE/NLTE oxygen abundances in a sample of Galactic subgiant and/or dwarf stars; the latter authors determined $[\mathrm{O/Fe}] \approx 0.4 - 0.6$ at the metallicity of HD 122563. Obviously, it would be premature to draw any firm conclusions based on the analysis of a single star.

---

[5] If the 3D NLTE Solar oxygen abundance of $\mathrm{A(O)}_{\odot} = 8.66$ determined by Asplund (2005) were used instead, the [O/Fe] ratios listed in Table 5.3 would increase by +0.1 dex

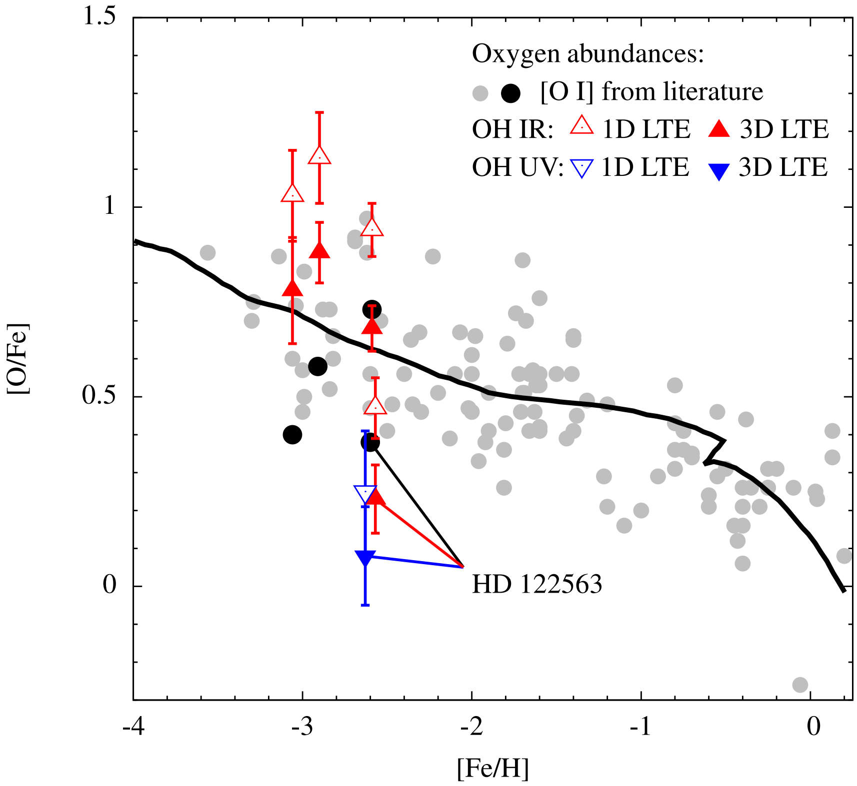

Fig. 5.13. Oxygen-to-iron ratios in the Galactic metal-poor stars (following Fig. 4 from Dobrovolskas et al. 2015). Solid grey circles depict [O/Fe] ratios in red giants, subgiants, and main sequence stars determined using the forbidden [O I] 630 nm line (literature data; see Dobrovolskas et al. 2015, for details). Red triangles show 3D LTE and 1D LTE [O/Fe] ratios in four metal-poor giants obtained from OH IR lines by Dobrovolskas et al. (2015, open and filled symbols, respectively). The [O/Fe] ratios determined in these stars from [O I] line are marked as black solid circles. Blue triangles are average [O/Fe] ratios in HD 122563 obtained in this study from 71 OH UV lines (for readability, abundances determined from OH UV and IR lines are shifted horizontally by ±0.03 dex). The solid line is the evolutionary model of François et al. (2004). Note that all abundance ratios are given in the reference scale where the solar oxygen abundance is $A(\mathrm{O}) = 8.76$ (Steffen et al. 2015).

Nevertheless, it seems that the oxygen abundance in HD 122563 loosely fits the scenario proposed by François et al. (2004), albeit on the lower boundary of the oxygen-to-iron ratios observed at this metallicity.

Summary and conclusions

In this Thesis we have developed a methodology for non-local thermodynamic equilibrium (NLTE) spectral synthesis computations of the spectral lines of atomic oxygen, using for this purpose `NLTE3D` package and three-dimensional `CO`^{5}`BOLD` model atmospheres. Prior to the work done in this Thesis, `NLTE3D` package was suited solely for the spectral synthesis of lithium lines, while in its current version it has been generalized, expanded and now suitable for solving a wider range of problems. Besides, with the implementation of ALI the `NLTE3D` package is able to reach the final solution faster, diminishing the computational time using 3D hydrodynamical model atmospheres by 3–5 times, while, in the 1D case, the speed-up factor might be as high as 100.

We have used state-of-the art atomic data in order to construct an O I model atom that can be used for the NLTE spectral synthesis with the `NLTE3D` code. The model atom consists of 22 atomic levels (and ground state of O II) and each level has associated bound-free transitions due to the photoionization and collisions with hydrogen and free electrons. The atomic levels are connected by 54 radiatively and collisionally permitted transitions, additional 10 transitions are purely collisional. We have performed various tests of the oxygen model atom (e.g., by adding additional atomic levels, radiative and collisional transitions) using solar model atmosphere and have shown that this model atom is sufficiently robust for determination of solar oxygen abundance. It was also found that we can safely ignore fine-structure of the O I IR triplet levels, as well as reduce the spatial resolution of the model atmosphere in horizontal directions without losing any accuracy on the computed spectral lines. The most significant remaining uncertainty of the model atom is collisional excitation and ionization by H I, which in our study was treated using the classical Drawin formula and scaled by a free parameter $S_{\rm H}$.

We have used this oxygen model atom in order to determine solar oxygen abundance using 3D hydrodynamical `CO`^{5}`BOLD`, 1D hydrostatic `LHD`, and 1D semi-empirical model atmospheres. We have utilized two sets of spectra – center-to-limb spectra obtained by William Livingston with the McMath-Pierce Solar Telescope (see Livingston et al. 2007, and references therein), and the high-quality center-to-limb spectra used by Pereira et al. (2009b) observed with the Swedish 1-m Solar Telescope (Scharmer et al. 2003). In order to derive two unknowns – solar oxygen abundance, A(O), and $S_{\rm H}$ parameter – we have performed fitting of the observed and theoretical spectral lines and line equivalent widths under the requirement that a single combination of A(O) and $S_{\rm H}$ would reproduce the observed spectrum at all inclination angles. The fitting procedures performed using 3D `CO5BOLD` model atmosphere and both center-to-limb spectra provided A(O) $= 8.76 \pm 0.02$ and $S_{\rm H} = 1.6 \pm 0.2$, which suggests a rather high solar oxygen abundance. Classical 1D `LHD` model atmospheres failed to produce a fitting solution and required unphysical $S_{\rm H} < 0$. It is also clear that the current treatment of collisions with hydrogen is not satisfactory and realistic collisional cross sections are urgently needed.

We have also used four 3D hydrodynamical `CO5BOLD` and 1D hydrostatic `LHD` model atmospheres of stars located near the base of RGB with $T_{\rm eff} \approx 5000$ K, $\log g = 2.5$ [cgs] and [Fe/H] $= 0, -1, -2, -3$ in order to study the impact of convection on the formation of weak fictitious molecular lines (CH, CO, C_2, NH, CN, and OH). The impact of convection was estimated via 3D–1D abundance corrections and its components, i.e., 3D–⟨3D⟩ and ⟨3D⟩–1D abundance corrections. It was found that strengths of molecular lines are very sensitive to the 3D hydrodynamical effects, thus 3D–1D abundance corrections may reach –1.8 dex for CO and –0.5 dex for OH at the lowest investigated metallicity [Fe/H] $= -3$. Investigation of the number densities of molecules has revealed that the formation of molecules in stellar atmospheres is very complex, non-linear process and which can be modelled in much more realistic way using 3D hydrodynamical model atmospheres.

We have also used high resolution VLT/UVES spectrum of the metal-poor halo giant HD 122563 in order to determine 1D LTE and 3D LTE oxygen abundances from OH lines located in the UV part of the spectrum (310–330 nm). We found that oxygen abundances determined from individual OH UV lines using 1D LTE techniques showed trends with line excitation potential and line strength, which may point to insufficient realism of the 1D hydrostatic model atmospheres used in 1D LTE abundance analysis. We further used 3D hydrodynamical `CO5BOLD` and 1D hydrostatic `LHD` model atmospheres to investigate the influence of convection on the formation of OH UV lines. Our results show that abundance trends with the line excitation potential and line strengths seen in the 1D analysis essentially disappear when 3D LTE abundances are used instead. It was also found that the convection-related effects lead to significant negative abundance corrections for OH UV lines that covered a range between ≈-0.45 dex at 0 eV to ≈0.0 dex at ≈1.5 eV. The oxygen-to-iron ratio in HD 122563 equal to [Fe/H] = 0.07 ± 0.13 dex, a value that falls on the lower boundary of the oxygen-to-iron ratio distribution observed in Galactic field stars at this metallicity.

References

Alexeeva, S. A., & Mashonkina, L. I. 2015, MNRAS, 453, 1619

Allen, C. W. 1973, Astrophysical Quantities (Athlone Press)

Allende Prieto, C., Lambert, D. L., & Asplund, M. 2001, ApJ, 556, L63

Allende Prieto, C., Asplund, M., & Fabiani Bendicho, P. 2004, A&A, 423, 1109

Amarsi, A. M., Asplund, M., Collet, R., et al. 2015, MNRAS, 454, L11

Amarsi, A. M., Lind, K., Asplund, M., et al. 2016, MNRAS, 463, 1518–1533

Aoki, W. 2015, ApJ, 811, 64

Arnaud, M., & Rothenflug, R. 1985, A&AS, 60, 425

Asplund, M., Nordlund, Å., Trampedach, R., et al. 1999, A&A, 346, L17

Asplund, M., & García Pérez, A. E. 2001, A&A, 372, 601

Asplund, M., Grevesse, N., Sauval, A. J., et al. 2004, A&A, 417, 751

Asplund, M., Grevesse, N., & Sauval, A. J. 2005, ASPC, 336, 25

Asplund, M. 2005, ARA&A, 43, 481

Auer, L. 1973, ApJ, 180, 469

Ayres, T. R., Lyons, J. R., Ludwig, H.-G., et al. 2013, ApJ, 765, 46

Bagnulo, S., Jehin, E., Ledoux, C., et al. 2003, Messenger, 114, 10

Bailey, J.E., Nagayama, T., Loisel, G.P., et al. 2015, Nature, 517, 56

Barbuy, B., Meléndez, J., Spite, M., et al. 2003, ApJ, 588, 1072

Barklem, P. S. 2007, A&A, 462, 781

Barklem, P. S., Belyaev, A. K., Guitou, M., et al. 2011, A&A, 530, A94

Barklem, P. S., Belyaev, A. K., Spielfiedel, A., et al. & Feautrier, N. 2012, A&A, 541, A80

Basu, S., & Antia, H. M. 2008, Phys. Rep., 457, 217

Beeck, B., Collet, R., Steffen, M., et al. 2012, A&A, 539, A121

Behara, N. T., Bonifacio, P., Ludwig, H.-G., et al. 2010, A&A, 513, A72

Bessell, M.S., Collet, R., Keller, S.C., et al. 2015, ApJ, 806, 16

Böhm-Vitense, E. 1958, ZAp, 46, 108

Caffau, E., & Ludwig, H.-G. 2007, A&A, 467, L11

Caffau, E., Ludwig, H.-G., Steffen, M., et al. 2008, A&A, 488, 1031

Caffau, E., 2009, Ph.D. thesis, Observatoire de Paris

Caffau, E., Ludwig, H.-G., Steffen, M., et al. 2011, Sol. Phys., 268, 255

Caffau, E., Ludwig, H.-G., Steffen, M., et al. 2015, A&A, 579, A88

Cannon, C. J. 1973, ApJ, 185, 621

Canuto, V. M., Goldman, I., & Mazzitelli, I. 1996, ApJ, 473, 550

Castelli, F., & Kurucz, R. L. 2004, arXiv:astro-ph/0405087

Castelli, F., Gratton, R. G., & Kurucz, R. L. 1997, A&A, 318, 841

Castelli, F., & Kurucz, R. L. 2003, in: 'Modeling of Stellar Atmospheres', Proc. IAU Symp. 210, eds. N. E. Piskunov, W. W. Weiss, & D.F. Gray, poster A20 (CD-ROM); synthetic spectra available at `http://cfaku5.cfa.harvard.edu/grids`

Cayrel, R., Depagne, E., Spite, M., et al. 2004, A&A, 416, 1117

Chiappini, C., Matteucci, F., & Romano, D. 2001, ApJ, 554, 1044

Chiappini, C., Matteucci, F., & Gratton, R. 1997, ApJ, 477, 765

Collet, R., Asplund, M., & Trampedach, R. 2007, A&A, 469, 687

Collet, R., Asplund, M., & Trampedach, R. 2006, ApJ, 644, L121

Creevey, O. L., Thévenin, F., Boyajian, T. S., et al. 2012, A&A, 545, 17

Cunto, W., Mendoza, C., Ochsenbein, F., et al. 1993, A&A, 275, L5

Dobrovolskas, V., Kučinskas, A., Steffen, M., et al. 2013, A&A, 559, A102

Dobrovolskas, V., Kučinskas, A., Bonifacio, P., et al. 2015, A&A, 576, A128

Dupree, A. K., Avrett, E. H., & Kurucz, R. L. 2016, ApJ, 821, L7

Drawin, H. W. 1969, ZPhy, 225, 483

Fabbian, D., Asplund, M., Barklem, P. S., et al. 2009, A&A, 500, 1221

François, P., Matteucci, F., Cayrel, R., et al. 2004, A&A, 421, 613

Freytag, B., Steffen, M., Ludwig, H.-G., et al. 2012, Journ. Comp. Phys., 231, 919

Freytag, B., & Salaris, M. 1999, ApJ, 513, L49

García Pérez, A. E., Asplund, M., Primas, et al. 2006, A&A, 451, 621

Gallagher, A. J., Caffau, E., Bonifacio, P., et al. 2016, A&A, 593, A48

González Hernández, J. I., Bonifacio, P., Ludwig, H.-G., et al. 2010, A&A, 519, A46

Gratton, R. G., Carretta, E., Matteucci, F., et al. 2000, A&A, 358, 671

Grevesse, N., & Sauval, A. J. 1998, Space Sci. Rev., 85, 161

Gustafsson, B., Edvardsson, B., Eriksson, K., et al. 2008, A&A, 486, 951

Hauschildt, P. H., Wehrse, R., Starrfield, S., et al. 1992, ApJ, 393, 307

Hayek, W., Asplund, M., Collet, R., et al. 2011, A&A, 529, A158

Holweger, H., Gehlsen, M., & Ruland, F. 1978, A&A, 70, 537

Holweger, H., & Mueller, E. A. 1974, Sol. Phys., 39, 19

Holweger, H. 1967, ZAp, 65, 365

Hubeny, I. 2003, Stellar Atmosphere Modeling, 288, 17

Hubeny, I., & Mihalas, D. 2014, Theory of Stellar Atmospheres, by I. Hubeny and D. Mihalas. Princeton, NJ: Princeton University Press, 2014,

Israelian, G., Rebolo, R., García L., et al. 2001, ApJ, 551, 833

Israelian, G., García López, R. J., & Rebolo, R. 1998, ApJ, 507, 805

Jofré, P., Heiter, U., Soubiran, C., et al. 2014, A&A, 564, A133

Kiselman, D. 1991, A&A, 245, L9

Kiselman, D. 1993, A&A, 275, 269

Klevas, J., Kučinskas, A., Steffen, M., et al. 2016, A&A, 586, A156

Kubát, J. 2010, EAS Publications Series, 43, 1

Kučinskas, A., Steffen, M., Ludwig, H.-G., et al. 2013, A&A, 549, A14

Kurucz, R. L. 1970, SAOSR, 309

Lambert, D. L. 1993, Physica Scripta Volume T, 47, 186

Livingston, W., Wallace, L., White, O. R., et al. 2007, ApJ, 657, 1137

Ludwig, H.-G., & Kučinskas, A. 2012, A&A, 547, A118

Ludwig, H.-G., Caffau, E., Steffen, M., et al. 2009, Mem. Soc. Astron. Italiana, 80, 711

Ludwig, H.-G., Jordan, S., & Steffen, M. 1994, A&A, 284, 105

Magain, P. 1986, A&A, 163, 135

Magic, Z., Collet, R., Asplund, M., et al. 2013, A&A, 557, A26

Markwardt, C. B. 2009, Astronomical Data Analysis Software and Systems XVIII, 411, 251

Mashonkina, L., Gehren, T., Shi, J.-R., et al. 2011, A&A, 528, A87

Matteucci, F., & Francois, P. 1992, A&A, 262, L1

Meléndez, J., & Barbuy, B. 2002, ApJ, 575, 474

Mihalas, D. Stellar Atmospheres, Freeman and Company

Neckel, H., & Labs, D. 1984, Sol. Phys., 90, 205

Neckel, H. 1999, Sol. Phys., 184, 421

Nordlund, Å. 1982, A&A, 107, 1

Nordlund, A., & Dravins, D. 1990, A&A, 228, 155

Pereira, T. M. D., Kiselman, D., & Asplund, M. 2009a, A&A, 507, 417

Pereira, T. M. D., Asplund, M., & Kiselman, D. 2009, A&A, 508, 1403

Prakapavičius, D., Kučinskas, A., Dobrovolskas, V., et al. 2017, A&A, 599, A128

Prakapavičius, D., Steffen, M., Kučinskas, A., et al. 2013, Proc. of the 2nd COBOLD Workshop, Mem. Soc. Astron. Italiana Suppl., 24, 111

Rybicki, G. B., & Hummer, D. G. 1991, A&A, 245, 171

Sbordone, L., Bonifacio, P., Castelli, F., et al. 2004, Mem. Soc. Astron. Italiana, 5, 93

Sbordone, L. 2005, Mem. Soc. Astron. Italiana, 8, 61

Scharmer, G. B., Bjelksjo, K., Korhonen, T. K., et al. 2003, Proc. SPIE, 4853, 341

Spite, M., Cayrel, R., Plez, B., et al. 2005, A&A, 430, 655

Stasińska, G., Prantzos, N., Meynet, G., et al. 2012, EAS Publications Series, 54, 255

Steenbock, W., & Holweger, H. 1984, A&A, 130, 319

Steffen, M., Prakapavičius, D., Caffau, E., et al. 2015, A&A, 583, A57

Steffen, M., Caffau, E., & Ludwig, H.-G. 2013, Memorie della Societa Astronomica Italiana Supplementi, 24, 37

Steffen, M., & Holweger, H. 2002, A&A, 387, 258

van Regemorter, H. 1962, ApJ, 136, 906

Villante, F.L., Serenelli, A. M., Delahaye, F., et al. 2014, ApJ, 787, 13

Vögler, A., Bruls, J. H. M. J., & Schüssler, M. 2004, A&A, 421, 741

Wedemeyer, S., Freytag, B., Steffen, M., Ludwig, H.-G., & Holweger, H. 2004, A&A, 414, 1121

Appendix A. The 3D–1D abundance corrections for the spectral lines of molecules observed in the spectra of red giant branch (RGB) stars located in the lower part of RGB

In this Appendix we provide lists of $\Delta_{\rm 3D-1D}$, $\Delta_{\rm 3D-<3D>}$ and $\Delta_{\rm <3D>-1D}$ corrections obtained for molecular (CO, CH, NH, OH, C_2, CN) lines in the atmospheres of red giant stars. The abundance corrections were computed at three different wavelengths (λ = 400, 850 and 1600 nm), four different model metallicities ([M/H] = 0, -1, -2, -3) and four different excitation potentials (χ = 0, 1, 2 and 3 eV). The abundance corrections are summarized in Tables A.1 (λ =400 nm), A.2 (λ =850 nm) and A.3 (λ =1600 nm).

Table A.1. 3D–1D abundance corrections for the spectral lines of molecules in the spectra of stars located close to the RGB base. Wavelength differs from molecule to molecule and are typical to those of molecular lines frequently used in the abundance work: λ (CO) = 400 nm, λ (CH) = 430.8 nm, λ (NH) = 336 nm, λ (OH) = 313.9 nm, λ (C_2) = 400 nm, λ (CN) = 388.3 nm.

molecule	[M/H]	$\Delta_{\rm 3D-1D}$				$\Delta_{\rm 3D-<3D>}$				$\Delta_{\rm <3D>-1D}$			
		0 eV	1 eV	2 eV	3 eV	0 eV	1 eV	2 eV	3 eV	0 eV	1 eV	2 eV	3 eV
CO	−3	−1.52	−1.24	−0.99	−0.77	−1.08	−0.88	−0.71	−0.56	−0.44	−0.36	−0.28	−0.20
	−2	−0.58	−0.41	−0.28	−0.17	−0.57	−0.42	−0.32	−0.24	−0.02	0.01	0.04	0.06
	−1	−0.05	−0.01	0.01	0.03	−0.17	−0.12	−0.09	−0.06	0.13	0.11	0.10	0.09
	0	0.01	0.02	0.03	0.03	−0.08	−0.06	−0.04	−0.02	0.09	0.07	0.06	0.05
CH	−3	−0.14	−0.07	−0.01	0.03	−0.18	−0.13	−0.09	−0.07	0.03	0.06	0.08	0.09
	−2	0.05	0.08	0.09	0.10	−0.06	−0.04	−0.03	−0.02	0.11	0.12	0.12	0.11
	−1	0.05	0.06	0.05	0.05	0.00	0.01	0.01	0.01	0.06	0.05	0.04	0.04
	0	0.04	0.04	0.05	0.05	0.01	0.01	0.01	0.02	0.04	0.03	0.03	0.03
NH	−3	−0.44	−0.23	−0.10	−0.02	−0.47	−0.29	−0.18	−0.10	0.03	0.06	0.07	0.08
	−2	−0.13	−0.03	0.03	0.07	−0.25	−0.15	−0.09	−0.05	0.12	0.12	0.12	0.11
	−1	0.01	0.03	0.04	0.05	−0.07	−0.04	−0.02	−0.01	0.08	0.07	0.06	0.05
	0	0.01	0.02	0.03	0.04	−0.05	−0.03	−0.01	0.00	0.06	0.05	0.04	0.04
OH	−3	−0.60	−0.34	−0.17	−0.06	−0.60	−0.38	−0.23	−0.13	0.00	0.03	0.06	0.07
	−2	−0.21	−0.08	0.01	0.05	−0.32	−0.19	−0.11	−0.06	0.11	0.11	0.11	0.11
	−1	0.00	0.02	0.04	0.05	−0.08	−0.05	−0.02	−0.01	0.08	0.07	0.06	0.05
	0	0.01	0.02	0.03	0.04	−0.04	−0.02	−0.01	0.01	0.05	0.04	0.04	0.03
C_2	−3	−0.28	−0.18	−0.11	−0.05	−0.20	−0.16	−0.12	−0.10	−0.08	−0.03	0.02	0.05
	−2	0.05	0.08	0.09	0.10	−0.04	−0.03	−0.02	−0.01	0.09	0.10	0.11	0.11
	−1	0.07	0.07	0.06	0.06	0.02	0.02	0.03	0.02	0.05	0.04	0.04	0.03
	0	0.05	0.05	0.05	0.05	0.02	0.02	0.03	0.03	0.03	0.02	0.02	0.02
CN	−3	−0.75	−0.56	−0.40	−0.26	−0.57	−0.44	−0.34	−0.25	−0.18	−0.12	−0.06	−0.01
	−2	−0.17	−0.09	−0.03	0.02	−0.24	−0.18	−0.13	−0.09	0.07	0.08	0.10	0.11
	−1	0.03	0.04	0.05	0.05	−0.06	−0.04	−0.02	−0.01	0.09	0.08	0.07	0.06
	0	0.02	0.03	0.04	0.04	−0.04	−0.03	−0.01	0.00	0.07	0.06	0.05	0.04

Table A.2. 3D–1D abundance corrections for the molecular lines located at λ = 850 nm in the spectra of stars located close to the RGB base.

molecule	[M/H]	$\Delta_{\rm 3D-1D}$				$\Delta_{\rm 3D-<3D>}$				$\Delta_{\rm <3D>-1D}$			
		0 eV	1 eV	2 eV	3 eV	0 eV	1 eV	2 eV	3 eV	0 eV	1 eV	2 eV	3 eV
CO	−3	−1.72	−1.42	−1.16	−0.93	−1.16	−0.96	−0.78	−0.63	−0.55	−0.46	−0.38	−0.30
	−2	−0.73	−0.54	−0.39	−0.26	−0.67	−0.51	−0.38	−0.29	−0.06	−0.03	−0.00	0.02
	−1	−0.08	−0.03	0.00	0.02	−0.22	−0.16	−0.11	−0.07	0.14	0.12	0.11	0.10
	0	0.00	0.02	0.03	0.03	−0.09	−0.07	−0.05	−0.03	0.10	0.08	0.07	0.06
CH	−3	−0.23	−0.13	−0.06	−0.01	−0.22	−0.16	−0.12	−0.09	−0.01	0.03	0.06	0.08
	−2	0.03	0.06	0.08	0.10	−0.07	−0.05	−0.03	−0.02	0.10	0.11	0.11	0.11
	−1	0.06	0.06	0.06	0.06	0.00	0.01	0.01	0.02	0.06	0.06	0.05	0.05
	0	0.05	0.05	0.05	0.05	0.00	0.01	0.01	0.02	0.04	0.04	0.04	0.03
NH	−3	−0.71	−0.42	−0.24	−0.11	−0.69	−0.45	−0.29	−0.19	−0.02	0.02	0.06	0.08
	−2	−0.29	−0.13	−0.04	0.02	−0.38	−0.24	−0.15	−0.09	0.10	0.11	0.11	0.12
	−1	−0.02	0.01	0.03	0.04	−0.11	−0.07	−0.05	−0.03	0.09	0.08	0.08	0.07
	0	0.00	0.01	0.03	0.03	−0.08	−0.05	−0.03	−0.02	0.08	0.07	0.06	0.05
OH	−3	−0.84	−0.58	−0.35	−0.19	−0.77	−0.57	−0.38	−0.25	−0.07	−0.02	0.03	0.06
	−2	−0.43	−0.22	−0.09	−0.01	−0.51	−0.32	−0.20	−0.12	0.09	0.10	0.11	0.11
	−1	−0.04	0.00	0.02	0.04	−0.14	−0.09	−0.06	−0.03	0.10	0.09	0.08	0.07
	0	0.00	0.02	0.03	0.04	−0.07	−0.04	−0.02	−0.01	0.07	0.06	0.05	0.05
C_2	−3	−0.38	−0.28	−0.19	−0.11	−0.23	−0.19	−0.15	−0.12	−0.15	−0.09	−0.04	0.01
	−2	0.02	0.06	0.08	0.10	−0.04	−0.02	−0.01	0.00	0.07	0.08	0.09	0.10
	−1	0.08	0.08	0.08	0.07	0.03	0.04	0.04	0.04	0.05	0.04	0.04	0.04
	0	0.06	0.05	0.05	0.05	0.03	0.03	0.03	0.03	0.03	0.02	0.02	0.02
CN	−3	−0.93	−0.72	−0.54	−0.39	−0.65	−0.52	−0.41	−0.32	−0.27	−0.20	−0.13	−0.07
	−2	−0.27	−0.17	−0.09	−0.03	−0.29	−0.22	−0.16	−0.11	0.03	0.05	0.07	0.08
	−1	0.02	0.03	0.05	0.06	−0.08	−0.05	−0.03	−0.02	0.10	0.09	0.08	0.07
	0	0.02	0.03	0.04	0.04	−0.05	−0.03	−0.02	−0.01	0.08	0.07	0.06	0.05

Table A.3. 3D–1D abundance corrections for the molecular lines located at λ = 1600 nm in the spectra of stars located close to the RGB base.

molecule	[M/H]	$\Delta_{\mathrm{3D-1D}}$				$\Delta_{\mathrm{3D-<3D>}}$				$\Delta_{\mathrm{<3D>-1D}}$			
		0 eV	1 eV	2 eV	3 eV	0 eV	1 eV	2 eV	3 eV	0 eV	1 eV	2 eV	3 eV
CO	−3	−1.61	−1.31	−1.05	−0.82	−1.15	−0.94	−0.76	−0.61	−0.45	−0.36	−0.28	−0.21
	−2	−0.63	−0.45	−0.31	−0.20	−0.62	−0.47	−0.35	−0.27	−0.01	0.02	0.04	0.07
	−1	−0.07	−0.04	−0.01	0.00	−0.21	−0.16	−0.12	−0.09	0.14	0.12	0.11	0.10
	0	−0.03	−0.02	−0.01	0.00	−0.13	−0.11	−0.09	−0.07	0.10	0.09	0.07	0.06
CH	−3	−0.17	−0.09	−0.04	−0.01	−0.21	−0.16	−0.13	−0.10	0.04	0.07	0.09	0.09
	−2	0.03	0.05	0.06	0.06	−0.09	−0.07	−0.06	−0.05	0.12	0.12	0.12	0.11
	−1	0.02	0.02	0.02	0.02	−0.03	−0.03	−0.02	−0.02	0.06	0.05	0.04	0.03
	0	0.01	0.01	0.01	0.02	−0.03	−0.02	−0.02	−0.01	0.04	0.03	0.03	0.03
NH	−3	−0.53	−0.37	−0.17	−0.08	−0.56	−0.37	−0.25	−0.17	0.03	0.06	0.08	0.09
	−2	−0.22	−0.09	−0.02	0.02	−0.35	−0.22	−0.14	−0.10	0.13	0.13	0.12	0.12
	−1	−0.04	−0.02	0.00	0.00	−0.12	−0.09	−0.07	−0.05	0.09	0.07	0.06	0.05
	0	−0.05	−0.04	−0.02	−0.01	−0.13	−0.09	−0.07	−0.05	0.07	0.06	0.05	0.04
OH	−3	−0.72	−0.44	−0.26	−0.13	−0.71	−0.48	−0.32	−0.21	0.00	0.04	0.06	0.08
	−2	−0.31	−0.15	−0.06	0.00	−0.43	−0.27	−0.18	−0.12	0.11	0.12	0.12	0.12
	−1	−0.05	−0.03	−0.01	0.00	−0.14	−0.11	−0.08	−0.06	0.09	0.08	0.07	0.06
	0	−0.04	−0.03	−0.01	0.00	−0.11	−0.08	−0.06	−0.04	0.07	0.06	0.05	0.04
C_2	−3	−0.30	−0.21	−0.13	−0.07	−0.23	−0.18	−0.15	−0.13	−0.08	−0.02	0.02	0.05
	−2	0.04	0.06	0.07	0.08	−0.06	−0.05	−0.05	−0.04	0.10	0.11	0.12	0.12
	−1	0.05	0.04	0.04	0.03	−0.01	0.00	0.00	−0.01	0.05	0.05	0.04	0.03
	0	0.02	0.02	0.02	0.02	−0.01	−0.01	0.00	0.00	0.03	0.03	0.02	0.02
CN	−3	−0.81	−0.61	−0.44	−0.30	−0.62	−0.49	−0.38	−0.29	−0.19	−0.12	−0.06	−0.01
	−2	−0.20	−0.12	−0.06	−0.01	−0.27	−0.21	−0.16	−0.12	0.07	0.09	0.10	0.11
	−1	0.00	0.01	0.02	0.02	−0.10	−0.08	−0.06	−0.05	0.10	0.09	0.08	0.07
	0	−0.02	−0.01	0.00	0.00	−0.10	−0.08	−0.06	−0.05	0.08	0.07	0.06	0.05

Appendix B. OH UV line list and oxygen abundances determined from individual lines in HD 122563

In this Appendix we provide a list of OH UV lines that were used in the oxygen abundance determination in HD 122563. We also provide oxygen abundances obtained from individual OH UV lines, as well as their errors (see Sect. 5.4.3 for details). All this information is summarized in Table B.1 the contents of which are as follows:

- column 1: line central wavelength;
- column 2: line excitation potential;
- column 3: log gf value;
- column 4: source of log gf value;
- column 5: line quality tag;
- column 6: line equivalent width;
- column 7: 1D LTE oxygen abundance and its error;
- column 8: 3D–1D abundance correction and its error;
- column 9: 3D LTE oxygen abundance and its error.

Table B.1. OH UV line parameters, 1D LTE abundances, 3D–1D LTE abundance corrections and 3D LTE abundances of oxygen determined in the atmosphere of the metal-poor red giant HD 122563 using different OH UV lines and 1D hydrostatic and 3D hydrodynamical model atmospheres.

λ nm	χ eV	log gf	Source	Quality	$W_{\rm i}$ pm	$A({\rm O})_{\rm 1D\ LTE}$ dex	$\Delta_{\rm 3D-1D}$ dex	$A({\rm O})_{\rm 3D\ LTE}$ dex
308.125	0.762	–1.882	WA	C	8.69	6.30±0.12	–0.26±0.05	6.04±0.13
308.489	0.843	–1.874	WA	B	8.43	6.44±0.12	–0.22±0.05	6.22±0.13
308.622	0.925	–1.852	WA	C	8.52	6.56±0.13	–0.20±0.05	6.36±0.14
308.900	0.928	–1.869	WA	C	8.88	6.63±0.15	–0.21±0.06	6.42±0.16
309.086	1.013	–1.850	WA	C	8.94	6.69±0.09	–0.19±0.06	6.50±0.11
309.239	0.164	–1.782	WA	C	12.5	6.36±0.17	–0.41±0.02	5.95±0.17
309.461	0.134	–1.899	WA	C	12.7	6.45±0.14	–0.41±0.02	6.04±0.14
309.554	0.205	–3.121	WA	C	6.71	6.56±0.11	–0.29±0.04	6.26±0.12

continued on next page

λ nm	χ eV	$\log gf$	Source	Quality	W_i pm	$A(\mathrm{O})_\mathrm{1D\ LTE}$ dex	$\Delta_\mathrm{3D-1D}$ dex	$A(\mathrm{O})_\mathrm{3D\ LTE}$ dex
309.665	0.170	–3.098	WA	C	7.55	6.65±0.11	–0.36±0.05	6.29±0.13
310.123	0.067	–2.205	WA	B	12.8	6.68±0.11	–0.43±0.04	6.25±0.12
310.435	1.202	–1.868	WA	C	6.24	6.40±0.11	–0.07±0.04	6.33±0.12
310.566	0.304	–1.708	WA	C	13.2	6.48±0.14	–0.34±0.02	6.14±0.15
310.654	0.095	–2.142	WA	C	13.0	6.76±0.09	–0.42±0.04	6.34±0.10
310.785	1.297	–1.858	WA	C	6.03	6.46±0.13	–0.05±0.04	6.41±0.14
310.907	0.358	–3.129	RK	B	6.78	6.62±0.11	–0.26±0.04	6.36±0.12
311.053	1.300	–1.873	WA	C	6.15	6.56±0.13	–0.06±0.04	6.50±0.13
311.307	0.053	–3.274	RK	B	7.48	6.60±0.13	–0.38±0.05	6.22±0.15
311.336	0.415	–1.649	WA	B	13.0	6.61±0.16	–0.31±0.02	6.30±0.16
311.477	0.474	–1.594	WA	C	11.8	6.46±0.15	–0.32±0.03	6.13±0.15
311.507	0.474	–3.170	RK	C	4.57	6.56±0.10	–0.13±0.02	6.43±0.10
312.058	0.075	–3.280	RK	C	6.76	6.56±0.13	–0.32±0.04	6.24±0.14
312.343	0.730	–2.102	RK	C	6.38	6.18±0.13	–0.15±0.04	6.02±0.14
312.394	0.205	–2.003	WA	C	11.4	6.45±0.12	–0.42±0.03	6.03±0.12
312.704	0.571	–2.442	WA	B	7.42	6.45±0.12	–0.24±0.05	6.21±0.13
312.735	0.735	–2.269	WA	B	7.26	6.36±0.13	–0.19±0.05	6.17±0.14
312.806	0.541	–2.511	WA	C	8.24	6.60±0.10	–0.28±0.05	6.31±0.12
312.993	1.609	–1.490	RK	C	3.91	6.16±0.11	0.01±0.01	6.16±0.11
313.617	0.452	–2.570	WA	C	7.18	6.42±0.15	–0.25±0.05	6.17±0.16
313.689	0.299	–1.939	WA	C	11.7	6.56±0.12	–0.38±0.03	6.18±0.13
313.770	1.031	–1.954	RK	C	6.42	6.34±0.10	–0.10±0.04	6.24±0.11
313.916	0.763	–1.564	WA	B	8.75	6.19±0.17	–0.24±0.05	5.95±0.18
314.073	0.304	–1.994	WA	C	11.4	6.56±0.13	–0.39±0.04	6.17±0.14
314.191	0.507	–2.186	WA	C	8.57	6.37±0.12	–0.30±0.05	6.07±0.13
315.100	0.411	–1.890	WA	A	10.9	6.49±0.15	–0.36±0.04	6.13±0.15
315.294	0.465	–2.961	RK	B	5.86	6.50±0.12	–0.17±0.03	6.33±0.13
316.482	1.107	–1.267	RK	C	8.48	6.15±0.15	–0.14±0.05	6.01±0.16
316.716	1.109	–1.694	GI	B	7.37	6.36±0.14	–0.11±0.05	6.25±0.15
316.986	0.838	–1.851	WA	B	9.35	6.45±0.14	–0.22±0.05	6.23±0.15
317.299	1.202	–1.526	WA	B	7.60	6.19±0.19	–0.10±0.05	6.09±0.20
317.319	0.842	–1.885	WA	C	8.50	6.45±0.11	–0.20±0.05	6.25±0.13
317.496	0.898	–1.673	RK	C	9.25	6.25±0.14	–0.21±0.05	6.04±0.15
317.530	1.204	–1.545	WA	C	8.37	6.46±0.15	–0.12±0.05	6.34±0.17

continued on next page

λ nm	χ eV	$\log gf$	Source	Quality	$W_{\rm i}$ pm	$A({\rm O})_{\rm 1D\ LTE}$ dex	$\Delta_{\rm 3D-1D}$ dex	$A({\rm O})_{\rm 3D\ LTE}$ dex
317.767	0.612	–1.720	RK	C	11.0	6.49±0.16	–0.29±0.04	6.20±0.17
318.047	0.961	–1.822	WA	B	8.16	6.36±0.14	–0.16±0.05	6.20±0.15
318.806	0.683	–2.182	WA	C	6.56	6.15±0.14	–0.15±0.04	6.00±0.15
318.931	1.032	–1.840	WA	A	6.04	6.24±0.11	–0.08±0.03	6.15±0.12
319.484	0.762	–1.848	WA	C	8.76	6.36±0.15	–0.22±0.05	6.14±0.16
319.910	0.735	–2.209	WA	C	7.11	6.36±0.10	–0.17±0.04	6.19±0.12
320.095	0.840	–1.810	WA	C	9.64	6.46±0.23	–0.22±0.05	6.24±0.24
320.623	0.786	–2.180	WA	B	7.52	6.46±0.12	–0.17±0.05	6.29±0.13
320.651	0.953	–2.387	WA	C	5.19	6.51±0.11	–0.07±0.02	6.44±0.12
320.677	1.252	–1.804	WA	B	5.79	6.36±0.13	–0.05±0.03	6.31±0.14
321.806	0.897	–2.093	WA	B	7.27	6.46±0.11	–0.14±0.04	6.32±0.12
322.336	1.016	–1.828	WA	B	7.87	6.46±0.16	–0.14±0.05	6.32±0.17
322.644	0.960	–1.927	RK	C	6.67	6.23±0.15	–0.11±0.04	6.12±0.15
323.514	1.836	–1.164	RK	C	4.22	6.14±0.10	0.02±0.01	6.16±0.10
323.757	1.016	–2.456	RK	B	3.74	6.36±0.11	–0.06±0.01	6.30±0.11
323.855	1.031	–2.104	WA	C	5.14	6.34±0.13	–0.06±0.02	6.28±0.13
324.144	1.199	–1.803	WA	B	6.67	6.36±0.14	–0.07±0.04	6.29±0.15
324.281	1.022	–2.540	RK	C	3.79	6.45±0.11	–0.06±0.01	6.39±0.11
324.915	1.059	–2.482	RK	C	5.08	6.59±0.13	–0.06±0.02	6.53±0.13
325.259	1.297	–1.807	WA	C	5.55	6.36±0.12	–0.05±0.02	6.32±0.13
325.549	1.300	–1.829	WA	A	5.34	6.35±0.10	–0.03±0.02	6.32±0.11
326.106	1.788	–1.427	RK	C	2.23	5.96±0.14	0.00±0.00	5.96±0.14
326.311	1.146	–2.387	RK	C	3.85	6.43±0.11	–0.05±0.01	6.38±0.11
326.665	1.191	–2.296	RK	C	3.45	6.35±0.11	–0.04±0.00	6.30±0.11
326.904	1.566	–1.846	RK	C	1.95	6.03±0.14	–0.02±0.00	6.00±0.14
327.073	1.195	–2.346	RK	B	2.74	6.26±0.15	–0.05±0.00	6.21±0.15
327.420	1.331	–1.810	RK	C	4.70	6.24±0.11	–0.03±0.01	6.21±0.11
329.126	1.488	–2.479	RK	C	1.31	6.36±0.15	–0.04±0.00	6.32±0.15
329.168	1.612	–1.490	RK	C	3.37	6.04±0.11	–0.01±0.00	6.03±0.11

Note: 'source' column indicates the reference of log *gf* value:
WA – Aoki (2015), RK – Castelli & Kurucz (2004),
GI – Israelian et al. (1998), GP – García Pérez et al. (2006)